European Master of Science
in Nuclear Fusion and Engineering Physics

Antenna Optimization for Plasma Positioning Reflectometry in Blanket-Equipped Tokamaks

Master Thesis
presented by

Johannes Lips

Thesis Promoter
Prof. Stéphane Heuraux
Université de Lorraine

Thesis Supervisor
Carsten Lechte
Burkhard Plaum
Universität Stuttgart

July 8th, 2020

Antenna Optimization for Plasma Positioning Reflectometry in Blanket-Equipped Tokamaks

Master Thesis
presented by

Johannes Lips

Thesis Promoter
Prof. Stéphane Heuraux
Université de Lorraine

Thesis Supervisor
Carsten Lechte
Burkhard Plaum
Universität Stuttgart

Erasmus Mundus Program on Nuclear Fusion Science and Engineering Physics

July 8th, 2020

Abstract

A future nuclear fusion power plant, which would produce clean and safe electricity, will require real-time control of the fusion plasma position. Plasma positioning reflectometry, a radar technique in which microwaves are reflected on the plasma, from which the distance between the radar antenna and the plasma can be derived, is a strong candidate to provide feedback on the plasma position for this control system. However, measurement perturbations caused by the interplay between the turbulent plasma and the metallic blankets surrounding the plasma make it difficult to use classical methods to reconstruct the plasma position. Also for new approaches which use neural networks or databases of full-wave simulations for the reconstruction, the problem is expected to be complex.

One possible solution lies in optimizing the antennas used in the reflectometer system. By modifying the antenna shape, antennas which behave similarly independent of the probing frequency can be designed, opening the way for reconstruction methods which can yield accurate results fast enough for plasma position control in blanket-equipped tokamaks.

In this work, a first attempt to design such a frequency-independent antenna is made. To assess the performance of different antennas, a two dimensional ray tracing code (R2P2), which simulates plasma positioning reflectometry in ITER-like conditions, is built. The results give insights in antenna behaviour and lead to several design criteria for the antenna.

Based on these results, a frequency-independent cylindrical horn antenna is optimized, taking into account the ITER-imposed spatial constraints.

A prototype of the optimized antenna is tested against a reference antenna. The optimized antenna shows clear advantages in the resulting radiation diagrams. The measurements also show that misalignment of the antennas and their surroundings can lead to large asymmetry in the radiation diagrams.

When mounted between ITER-like blankets, the optimization effects disappear. Also when reducing the length of the blanket structures, the influence of the blankets on the radiation diagram remains. This suggests that a second optimization is required, in which the antenna is optimized directly in its surroundings.

Simulations of the optimized antenna with small amounts of higher-order modes at the antenna input show that these modes can lead to offsets in the direction of the main lobe of the antenna. The suggested second optimization should therefore also consider the waveguide modes at the antenna input.

Keywords: Plasma positioning reflectometry, plasma diagnostics, horn antennas, optimization, ray tracing, simulation methods and programs, ITER, fusion

Nuclear fusion, the energy of the sun. Ever since we humans have understood the physics behind nuclear fusion, some of us have been dreaming of using the same processes to produce clean, safe and renewable energy on earth. A dream with a lot of challenges, a lot of uncertainties, a lot of research still to be done. It is a long trip to the sun, but we will get there, lifted by our dreams and standing on the shoulders of giants.

Contents

Chapter 1

Introduction

1.1 The Physics of Fusion

Nuclear fusion is a physical reaction, of which the name describes the process very well: multiple atomic nuclei are fused, driven by the nuclear force. This process is accompanied by a release in energy. The dominant fusion reaction in the sun is the following:

$$\mathrm{p} + \mathrm{p} \rightarrow \mathrm{D} + e^{+} + \nu + 0.42\,\mathrm{MeV} \tag{1.1}$$

In this reaction two protons p, fuse into deuterium D (a hydrogen isotope containing 1 proton and 1 neutron), a positron e^{+}, and a neutrino ν. During the process 0.42 MeV energy is released. This reaction has a very low cross-section ($\approx 10 \cdot 10^{-50}\,\mathrm{m}^2$ [1]), meaning it is not likely to happen, and making it not the most interesting reaction to try to achieve on earth. Instead, deuterium-tritium (DT) fusion is the reaction aimed for:

$$\mathrm{D} + \mathrm{T} \rightarrow {}^{4}\mathrm{He}\ (3.5\,\mathrm{MeV}) + \mathrm{n}\ (14.1\,\mathrm{MeV}) \tag{1.2}$$

Deuterium and tritium (a hydrogen isotope containing 1 proton and 2 neutrons) are fused, forming a helium atom (containing 3.5 MeV or about one fifth of the reaction energy) and a fast neutron (containing the remaining four fifth of the energy release). This reaction has a higher cross-section ($\approx 10 \cdot 10^{-30}\,\mathrm{m}^2$ [2]) under conditions which can be achieved on earth. In a fusion power plant, this fusion reaction will be followed by a second reaction with lithium:

$$\mathrm{n} + {}^{6}\mathrm{Li} \rightarrow {}^{4}\mathrm{He} + \mathrm{T} + 4.78\,\mathrm{MeV} \tag{1.3a}$$

$$\mathrm{n} + {}^{7}\mathrm{Li} \rightarrow {}^{4}\mathrm{He} + \mathrm{T} + \mathrm{n} - 2.47\,\mathrm{MeV} \tag{1.3b}$$

A neutron n, produced by the fusion reaction in Equation 1.2, reacts with lithium to form tritium which can fuel another fusion reaction[1]. Depending on the

[1] However, some neutrons from the fusion reaction (1.2) will be lost and will not react with Li. To make sure enough T-production occurs, other n-producing reactions will occur as well, so that there are more neutrons available to react with Li and produce T. This also means that a fusion reactor generates radioactivity, albeit with a very short lifetime compared to the radioactive waste of a fission reactor.

lithium isotope with which the neutron reacts, either additional energy is released or energy from the fast neutron is used. Reactors in which these lithium-reactions occur are called breeder reactors, as the tritium-fuel for the fusion reactions is bred in the reactor vessel itself. The produced tritium is collected and stored, so that it can be added to the plasma in a controlled way. These two reactions form the core of a fusion reactor and are illustrated in Figure 1.1. Not only is it very convenient to produce tritium, it is also necessary; tritium is rare and the total available amount of tritium on earth is in the same order of magnitude as that which a fusion power plant would use in a single year [3]. Deuterium is not produced in the reactor, but is available and can be added to the process from a storage facility nearby the reactor.

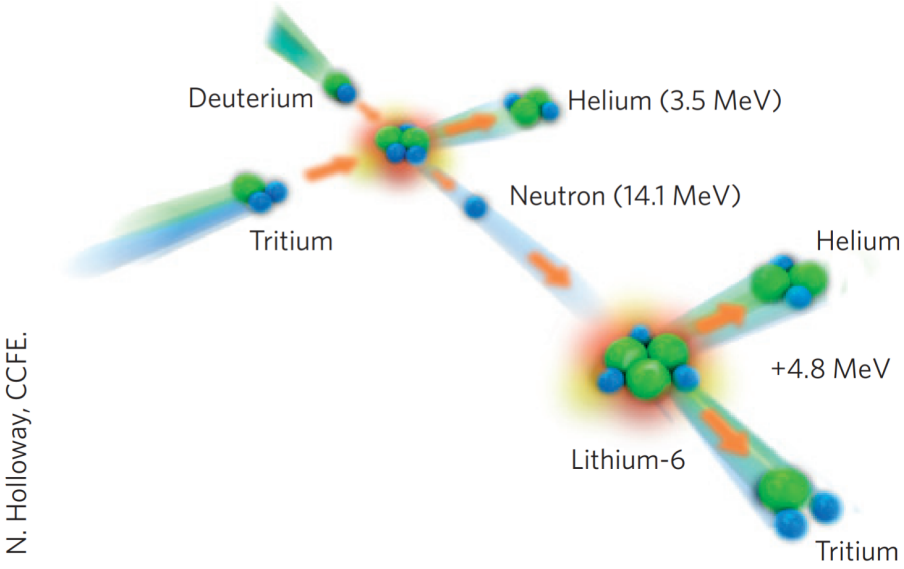

Figure 1.1: Reactions occurring in a breeder fusion reactor: deuterium and tritium fuse to produce a neutron, which then reacts with lithium (here depicted ^{6}Li) to form tritium, effectively breeding the T-fuel. Both reactions produce helium ions as a byproduct. [4]

1.2 Conditions for Fusion

A first condition for fusion to occur is that free atomic nuclei, positive *ions*, must exist to be able to react. This means that the deuterium and tritium atoms must first undergo ionization reactions, splitting them into ions and free electrons. Ionization reactions can be thought of as a phase transition. Just like vaporization is the transition between a liquid and a gas, ionization is the transition between gas and plasma[2]. The DT-fuel mixture needs to be in this plasma state, i.e. there need to be a sufficient amount of ionized particles. Just like any other phase

[2]Unlike other phase transitions however, ionization does not occur on a single line in a p-T diagram but instead occurs depending on various other properties of the system. Approaching ionization as a phase transition is correct, but it must be kept in mind that it does not act as a 'normal' phase transition all the way.

transition which gets a system to a higher energetic state, ionization requires activation energy, so the system needs to consist of high-energetic particles in order for the plasma state to be achieved. As the plasma contains free negative electrons and positive ions, it has electromagnetic properties: it can conduct electricity, reflect or screen electric fields or be contained by magnetic fields.

Exactly electromagnetism is responsible for a second, more strict condition to obtain fusion. In the plasma state, two *positive* ions need to fuse together. However, positive charges repel each other. It is necessary for the particles to overcome this repelling electromagnetic force (the Coulomb barrier), if they are to be fused. To do this, they need even more energy than the plasma state requires. Both from engineering as from reaction-probabilistic point of view a particle energy of about 10 to 20 keV, corresponding to a temperature of 115 to 230 million Kelvin would be good for DT-fusion on earth [5, Chapter 10].

An extra condition is of course that produced plasma should be confined. It costs a lot of energy to produce the plasma, so losing it (and having to spend more energy to create more plasma) would make a future fusion reactor very inefficient. Additionally, due to the high energy of the plasma particles, it would destroy almost any material it comes in contact with. This condition might sound trivial, but instabilities that follow from the complicated interplay of forces which lies at the basis of plasma physics make containing a plasma a difficult task.

Creating these conditions is one of the main challenges in fusion research today. It is not reaching the conditions per se which is difficult, but reaching and maintaining these conditions in an energy-efficient way. After all, a fusion power plant is supposed to be a power plant, with as only goal electricity production. The difficulty in the research is not to make fusion possible, it is to make fusion with a net energy output possible. This can be reformulated in terms of the 'Q-factor':

$$Q = \frac{P_{\text{fusion}}}{P_{\text{aux}}} \geq 1 \tag{1.4}$$

in which P_{fusion} is the power produced by the fusion reaction and P_{aux} is the auxiliary power necessary to create the conditions for fusion to occur. It is reaching $Q \geq 1$ which is the main goal of the fusion community today.

1.3 Fusion Reactors

There are multiple possibilities for creating the conditions for fusion, one of them occurs in the sun.The large gravitational field provides both a high pressure and temperature such that the plasma state is maintained and the plasma remains confined.

Several other possibilities are being investigated for fusion as an energy source on earth. Magnetic confinement of the tokamak and stellerator type, together with inertial confinement fusion are the main areas of investigation. The tokamak (a Russian acronym standing for toroidal chamber with magnetic coils) is at this moment the closest to achieving self-sustained fusion. The other technologies will not be discussed in this work. ITER (Figure 1.2), the biggest tokamak in the world, currently under construction in Cadarache, France, will be the first fusion

experiment that aims to reach $Q \geq 1$ and will go up to $Q = 10$. Up to now, most fusion experiments have had a different goal, namely to examine the conditions under which fusion can happen without actually trying to achieve fusion, mainly by investigating plasma physics to determine relevant scenarios for ITER to work in safe conditions.

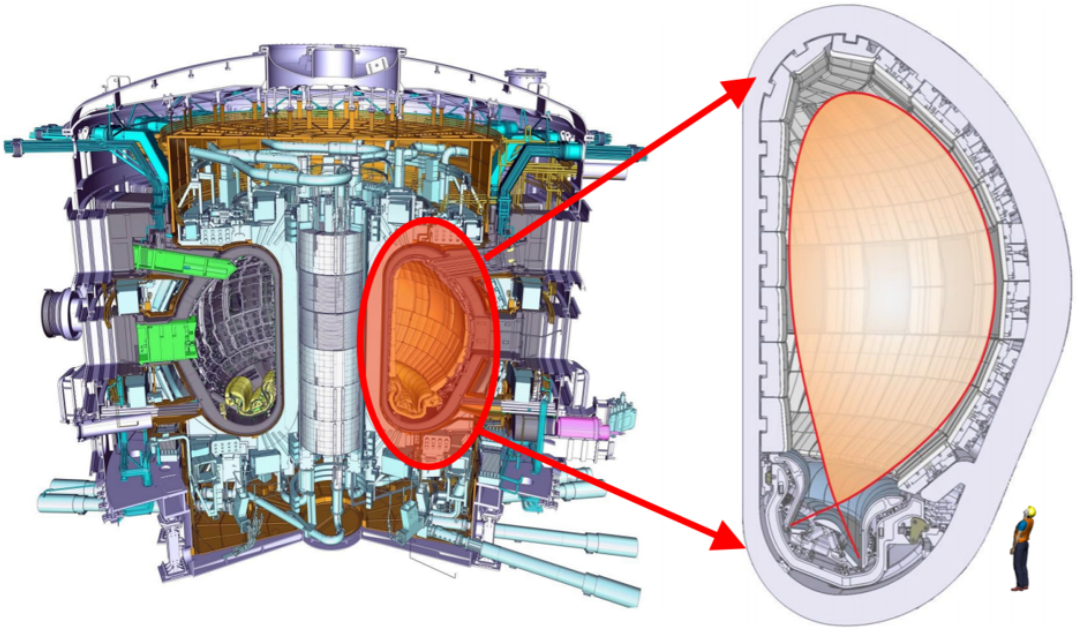

Figure 1.2: Overview of the ITER reactor, (left) full toroidal vessel and auxiliary systems, (right) the plasma vessel with a person for comparison, the plasma is coloured transparent orange [6].

In a tokamak, the plasma (marked orange on the Figure 1.2) flows around in a toroidal (donut-shaped) vessel without touching its walls. A complicated magnetic field in and around the vessel is responsible for its confinement. On Figure 1.3, two poloidal cross-sections of the ITER tokamak are shown. Figure 1.3a shows different parts of the magnetic confinement system. These are the central solenoid (red), which induces a current in the plasma; toroidal fieldcoils (green) and poloidal fieldcoils (blue). The resulting magnetic fieldlines go almost toroidally (so in the plane of the figure). In fact these fieldlines are helical and have an offset of a couple of degrees from a full toroidal path. All of the coils of ITER will be superconducting, limiting the power consumption. The resulting magnetic field allows for a good plasma confinement and positioning. The condition of containing the plasma is thus satisfied.

To produce the plasma, multiple schemes for heating the DT mixture to high enough energies are available. A couple of possibilities use electromagnetic radiation to heat the plasma (somewhat similar to a microwave oven), specifically by enlarging one component of the kinetic energy of one of the particle species in the plasma. Another scheme uses neutral beam injection (NBI), in which highly energetic hydrogen atoms are shot at the plasma and give their energy to raise the total plasma energy. Part of the energy released with the fusion reactions can also serve to maintain the plasma state; the helium ion (a so-called α-particle)

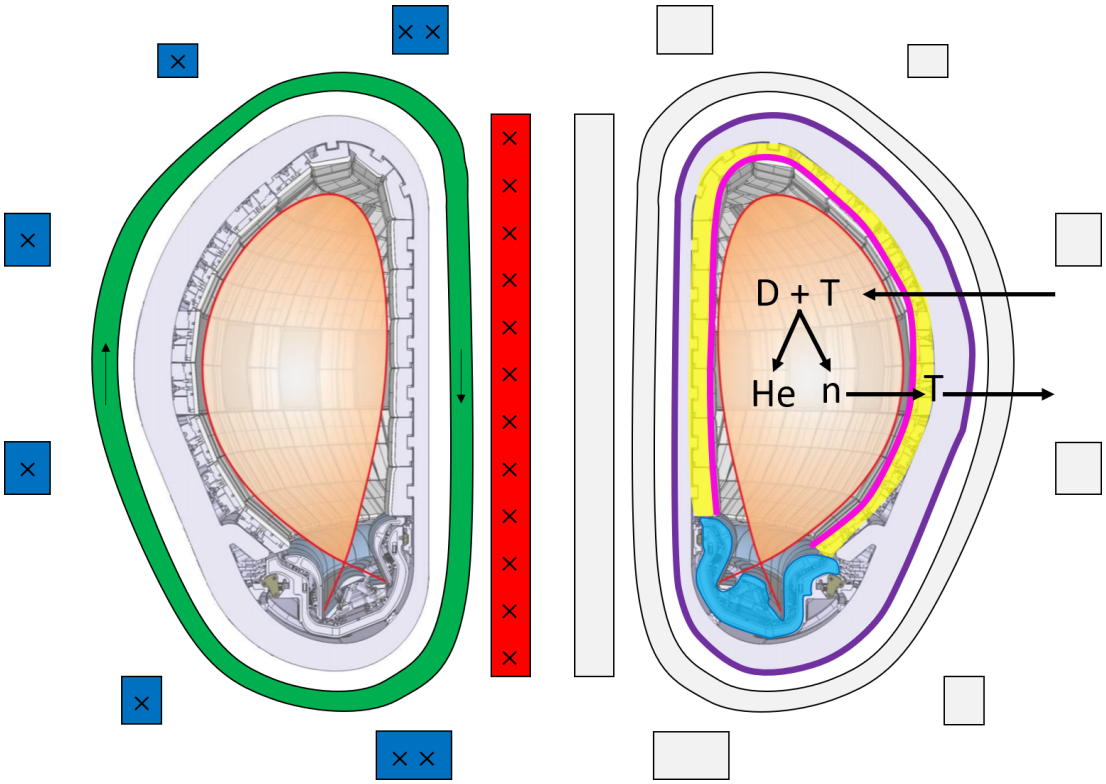

(a) Magnetic confinement components with arrows indicating direction of currents: central solenoid (red), toroidal fieldcoils (green), poloidal fieldcoils (blue).

(b) Vacuum vessel components: first wall (fuchsia), breeder blanket (yellow), divertor (light blue), vacuum vessel (purple), also showing ITER main reactions.

Figure 1.3: Poloidal cross-sections of ITER tokamak.

produced in Equation 1.2, is positively charged and therefore confined by the magnetic field which keeps the plasma together. This means that its energy (3.5 MeV or about one fifth of the fusion energy) stays inside the plasma and heats the plasma. A combination of these heating methods will be used in ITER to obtain and maintain the conditions in which fusion can occur.

Only charged particles are confined in the tokamak, so the neutron from Equation 1.2 is not contained and escapes the toroidal chamber where it impacts on the walls of the vessel, called the breeder blankets. In a fusion reactor, this is the place where the tritium-producing reactions between neutrons and lithium (Equation 1.3) happen. The main reaction-cycle is illustrated on Figure 1.3b, on which the breeder blankets are marked in yellow. The breeder blankets are actively cooled: the huge energy carried by the neutrons and the additional energy releases from the lithium reactions heat the material, heat which is then transferred to a coolant. It is the heat contained in the coolant which could be used to drive a classical turbine to produce electricity. In ITER however, the conversion to electricity will not be done. The goal of ITER is to reach $Q \geq 1$, but it still is an experimental reactor and will not be connected to the power grid. Another big project, named DEMO, will be build later and will be the first tokamak to provide electricity to the grid.

On Figure 1.3b some other important components of ITER are marked. The first wall (fuchsia on the figure) consists of tungsten alloys. These are necessary to withstand high heat loads coming from radiation and impacting plasma particles which managed to escape the magnetic confinement. In light blue, the divertor is marked. Its function is to remove helium from the plasma. Although this by-product of the reactions (Equations 1.2 and 1.3) is useful to heat the plasma, it is an impurity which reduces the efficiency of the fusion processes and would accumulate over time if not removed. The divertor collects the helium and other impurities and gets them out of the main plasma. Finally the vacuum vessel (purple) is marked, which keeps the plasma at the correct pressure.

1.4 Plasma Positioning Control

The plasma in ITER will reach core temperatures of 150 million °C. Inside the tokamak, the magnetic confinement system is responsible for keeping the plasma in a position where it does not touch and destroy the walls. This crucial task also carries other benefits; a good plasma position is necessary for efficient fusion processes with minimal losses. To keep the plasma position correct, constant monitoring is necessary. A fusion plasma is highly turbulent, similar to turbulent gases and liquids, but fundamentally different since also electromagnetic forces play a role. Where the steady-state magnetic field generated by the magnetic confinement components is responsible for controlling the drift-motions which the ions and electrons undergo as a consequence of plasma physics, a continuous fine-tuning of the poloidal fieldcoil currents (blue on Figure 1.3a) is responsible for compensating changes in the plasma position induced by turbulence, heating, fueling, and other non steady-state changes in the plasma [7, Section 1.7].

The block diagram of the plasma positioning control scheme is presented in Figure 1.4. When wanting to keep the plasma position at a certain reference $\vec{r}_{\text{ref}}$, the real-time position $\vec{r}_{\text{real}}$ is compared with the reference. The difference between these $\Delta\vec{r}$ is fed to a controller which sends steering signals to the power supply of the poloidal fieldcoils. The power supply changes the amount of power sent to the coils, changing the current in the coils, which results in a change in the magnetic field in the tokamak. The plasma reacts on the change in the magnetic field by changing its position towards the reference. At the same time, perturbations δ caused by e.g. turbulence change the plasma position, such that the real position is again different from the reference. A plasma positioning diagnostic measures plasma properties from which a plasma position can be reconstructed, this real-time position is then send back to the start of the loop. The faster this loop can work, the better the resulting plasma position. Every block of the loop introduces time delays, and it is important to minimize these delays where possible.

The focus of this thesis is the design of a plasma positioning diagnostic which allows for a fast and correct plasma position reconstruction in power plant-like tokamaks with long pulse operation. In current-day, small tokamaks which are operated only in short pulses and without DT-fusion, the diagnostics used are magnetic pickup coils. These are small coils placed around a poloidal cross-section

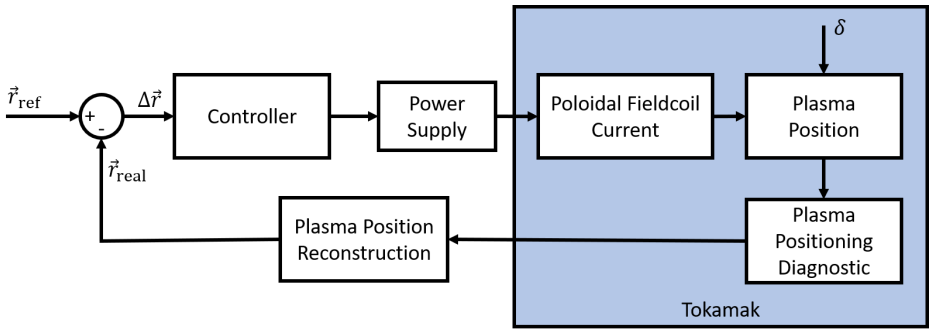

Figure 1.4: Block diagram of plasma position controller with feedback.

in which currents are induced as a consequence of the plasma current. The amount of induced current varies with the distance of the edge to the plasma, so that by integrating the measured currents the distance between the plasma and the wall is obtained. With enough coils, it is possible to get a good reconstruction of the plasma position. [7, 8]. This magnetic diagnostic has some major shortcomings when it comes to big fusion reactors which will probably operate in very long pulses (in the order of 20000 seconds [3]) and will have high neutron radiation on the walls. The radiation will induce changes in conductivity and emf's in the pick-up coils, continuously changing their behaviour and making a correct interpretation of the measurements difficult [9]. Additionally, the integrators which process the measured signals to the distance between plasma and wall are known to be inaccurate when operated for longer time (the so-called drifting integrator effect), and although advancements are made in the integrator designs, recent integrators can function well only in the order of 1000s [10] which is still far from 20000s. In ITER, the plasma positioning feedback must be accurate up to 1 cm [11]. With the current state of the magnetic diagnostics, this is not possible for long, nuclear discharges.

A different diagnostic which can be used is a plasma positioning reflectometer (PPR). A PPR uses radar-detection techniques. Electromagnetic radiation is emitted by an antenna and reflects on an object. It returns to a receiving antenna and the time between emitting and receiving the signal can be calculated, from which the distance to the object can be derived. Unlike traditional radar, where the object on which the radiation is reflected is metallic, for plasma reflectometry the plasma itself reflects the radiation. Different emitted frequencies will reflect on different density layers of the plasma, so that a frequency sweep will result in sufficient knowledge to make a density mapping and determine the plasma position [12].

PPR has been successfully integrated as part of the control circuit from Figure 1.4 in the tokamak ASDEX-Upgrade in Germany [13, 14] and does not suffer from the same problems as the magnetic pickup coils. However, its design poses new challenges in terms of plasma position reconstruction in blanket-equipped tokamaks. The blankets (which are not present in ASDEX-Upgrade) have a major influence on the received signals in PPR and make plasma position reconstruction within the ITER 1 cm tolerance level difficult [11, 15].

A possible solution for this problem is to use new methods using neural net-

works [16] or databases of full-wave simulations [17]. But also for these methods, plasma position reconstruction in blanket-equipped tokamaks remains a challenging task and it is feared that real-time feedback is not possible given the complexity of the problem [18]. One of the problems is that the radiation diagrams of the currently suggested antennas are frequency dependent [19], so that the spatial correlation of turbulent regions is convoluted with changes in radiation diagram as a frequency sweep is made by the PPR. A complex deconvolution of these effects is necessary to interpret the received signals.

In this work, a first attempt is made to design broadband PPR antennas with frequency-independent radiation patterns in order to lower the amplitude variations when the frequency changes, with the broader goal of enabling fast and accurate plasma position reconstruction in blanket-equipped tokamaks.

1.5 Thesis Outline

The work is organized as follows: in Chapter 2, the theoretical background of a plasma positioning reflectometer is explained in detail. In Chapter 3, the two dimensional ray tracing code 'R2P2', which was built to evaluate the performance of different antennas, is introduced. In Chapter 4, the results of simulations done with R2P2 are analysed and discussed. In Chapter 5 a design for a performant, frequency-independent antenna is made using PROFUSION [20, 21]. In Chapter 6 a prototype of the antenna is tested and compared with a reference antenna. A final chapter contains conclusions and suggestions for further research.

Chapter 2

Plasma Positioning Reflectometer Basics

2.1 Plasma Physics

Plasma has some properties which are similar to gaseous substances and at the same time complex electromagnetic behaviour. In section 1.2, several properties of a plasma were already mentioned briefly, now those which are most relevant for a plasma position reflectometer (PPR) will be discussed in more detail.

2.1.1 Density and Magnetic Field Profiles

The plasma in a tokamak is confined by a magnetic (B-) field. Symmetry in the toroidal direction is assumed, meaning that the plasma looks the same in each poloidal cross-section. A typical spatial evolution of the B-field strength and electron density of the plasma in a poloidal cross-section are given in Figure 2.1. The variable R is the radial position from the center of the tokamak, R_0 is the location where the plasma density is maximum and where the barycenter of the plasma is located, called the plasma major radius. An alternative axis x is defined, starting from the center of the plasma R_0. With the assumption of toroidal symmetry, the coordinate

$$\vec{r} = x \cdot \vec{e_x} + z \cdot \vec{e_z}$$

$$r = |\vec{r}| = \sqrt{x^2 + z^2}$$

gives a complete description of the location in the plasma (in which $\vec{e_i}$ is a unity vector along axis i). The plasma minor radius a is defined as the distance between plasma center and the point where the plasma density $n(\vec{r} = a) = 0\,\mathrm{m}^{-3}$. The ITER-like values given in Table 2.1 will be used in this work and the R2P2-code.

The magnetic field $\vec{B}$ in a tokamak points approximately in the toroidal direction (the y-direction of Figure 2.1). Because it has an offset of a couple of degrees from this axis, the resulting fieldlines are not circular but helical, which is necessary to have a stable plasma. In first order, $B_{\mathrm{tor}} \gg B_{\mathrm{pol}}$, the field strength can be approximated by:

$$B(R) = B_0 \cdot \frac{R_0}{R} \tag{2.1}$$

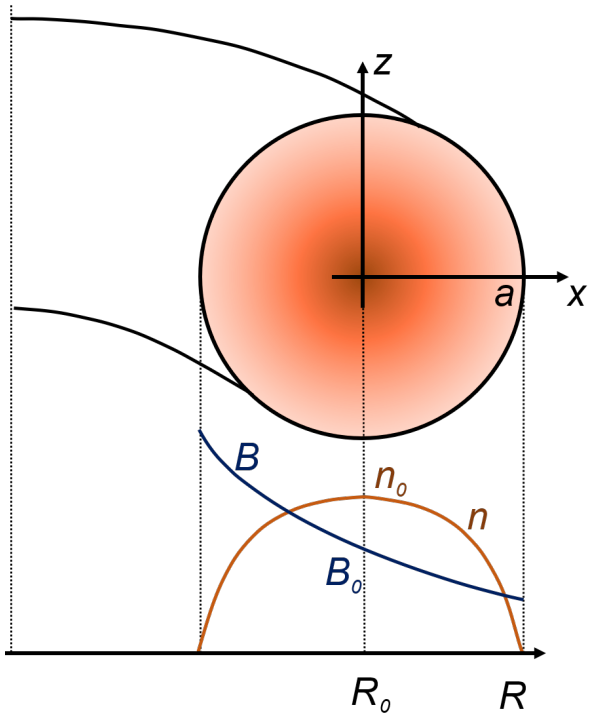

Figure 2.1: Typical density $n(R)$ and magnetic field $B(R)$ profile in poloidal cross-section of a tokamak with major radius R_0 and minor radius a [5]. Values for R_0, a, n_0 and B_0 are found in Table 2.1.

The side $x > 0$ is called the low-field side (LFS), the side $x < 0$ is named high-field side (HFS), also named the good-curvature region (opposed to the LFS, which is the bad-curvature region). The names bad- and good-curvature region refer to an instability, the interchange instability, which occurs when the pressure gradient and magnetic field gradient are pointing in the same direction. On Figure 2.1 it can be seen that this unfavorable behaviour occurs in a tokamak on the outer side (LFS, bad-curvature) and stabilizing behaviour exists for the HFS. The helical magnetic fieldlines, along which the plasma particles move, cause the particles to spend some time in the bad-curvature region and some time in the good-curvature region, so that instabilities will grow for some time and later be damped again. It is because of this and many other instabilities that the exact shape of the magnetic fieldlines plays such a crucial role in a tokamak.

Table 2.1: ITER-like values for the main tokamak parameters which are used throughout this work (depicted at Fig. 2.1).

R_0	6.2 m
a	2 m
n_0	$10^{20}\,\mathrm{m}^{-3}$
B_0	5.3 T

The main electron density profile $n_e = n$ is often approximated by a quadratic equation in r with maximum $n(r = 0) = n_0$ and $n(r = a) = 0$:

$$n(r) = n_0 - n_0 \frac{r^2}{a^2} \tag{2.2a}$$

$$n(x, z) = n_0 - n_0 \frac{x^2 + z^2}{a^2} \tag{2.2b}$$

Shapes other than this are also possible; often, in the so-called high confinement mode (H-mode), a fusion plasma will have a steep slope in the edge region of the plasma and a relatively flat central part, the quadratic profile is however a very realistic, yet simple main density profile and will be used in this work. In a real scenario, additional turbulence δn (which can be asymmetric in all coordinates) exists and plays an important role in the behaviour of the plasma and its interactions with e.g. heating sources.

Turbulent transport can be connected with a number of instabilities which can be grouped in MHD (magneto-hydrodynamical) turbulence on the one hand, which are instabilities with a quasi-constant structure in the direction of the magnetic fieldlines; and driftwave turbulence on the other hand, which has dynamic behaviour along the fieldlines. MHD turbulence typically shows small interchange instabilities in the bad-curvature region [5, Chapter 15]. The turbulence model which is used in this work will be discussed in detail in Section 3.4.1.

2.1.2 Debye Shielding and Plasma Frequency

A free charge q_0 brings with it an electrostatic Coulomb-potential of the form

$$\phi(r) = \frac{q_0}{4\pi\epsilon_0} \frac{1}{r} \tag{2.3}$$

with r the distance from the charge. This potential is linked with the electrical field of the charge, making it possible to detect the charge and interact with it. In a plasma there are both positive and negative charges present in more or less equal numbers. On a small spatial scale, these charges attract each other. Because the mobility of the electrons is large compared with that of the positive charges, a positive test charge will be surrounded by negative electrons which 'screen' the positive charge. Assuming an isotropic plasma, spherical symmetry can be applied. Because of the screening, the test charge potential changes to the Debye-Hückel potential:

$$\phi(r) = \frac{q_0}{4\pi\epsilon_0} \frac{1}{r} \cdot e^{-\sqrt{2}r/\lambda_D} \tag{2.4}$$

The potential now has a strong exponential decrease instead of the previous $1/r$ behaviour, meaning it will be not possible to detect the charge as soon as the observer is further away than roughly the Debye-length λ_D (typically $7 \cdot 10^{-5}\,\mathrm{m}$ for fusion plasmas [5, p. 9]). A result of this shielding is quasi-neutrality: because negative and positive charges will shield each other, inside the plasma the electron

density n_e equals the ion density n_i multiplied with the effective charge number Z_i of the ions:

$$n_e \approx Z_i n_i \tag{2.5}$$

This explanation is true for a stationary charge. A next question can be how fast the test charge can move/oscillate while still being effectively shielded by the plasma. This oscillation frequency is called the plasma frequency f_p (with angular frequency $\omega_p = 2\pi f_p$). Electrons are the lightest particles in the plasma and as a result of their low inertia they can react the fastest to changes such as the moving electric field of an oscillating charge. It is only when the electrons can no longer follow the movements of a test charge that their shielding is not effective anymore. This happens when the electron plasma frequency is reached, which for a plasma with density n is given by:

$$\omega_{pe} = \sqrt{\frac{e^2 n}{\epsilon_0 m_e}} \tag{2.6}$$

When a test charge oscillates faster than ω_{pe} it will no longer be shielded and then it can be observed from outside the plasma. Or more generally: the plasma does not have a screening effect on electric fields which oscillate faster than ω_{pe}. This also means that waves with frequency $f > f_p$ can pass through the plasma, while waves with a frequency $f < f_p$ will be shielded, in other words reflected, by it.

2.1.3 Dispersion Relations

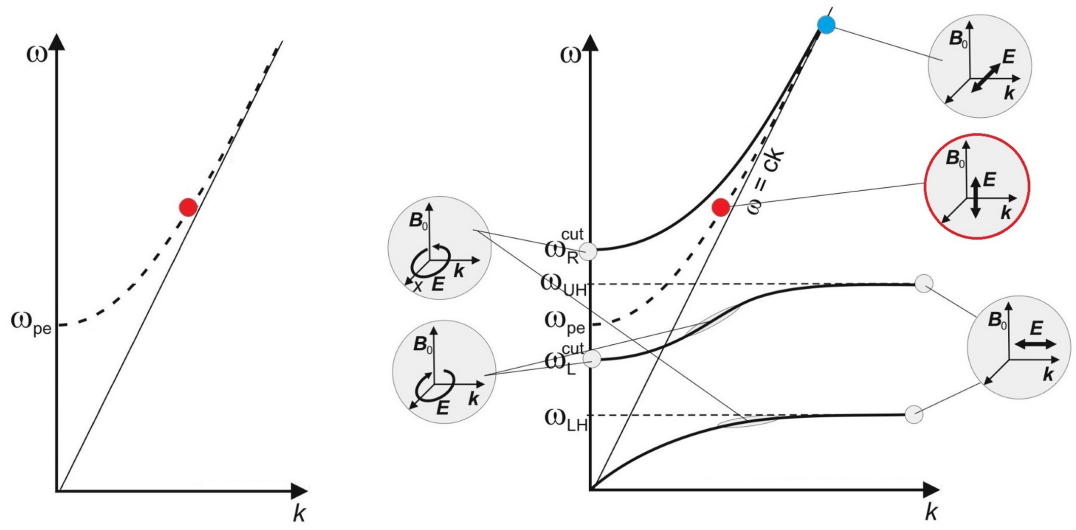

(a) cold, unmagnetized plasma

(b) cold, magnetized plasma for $\vec{k} \perp \vec{B}$

Figure 2.2: Dispersion relationships in plasma. A straight line $\omega = ck$ (vacuum propagation) is drawn for comparison, the dashed line with the red dot is the O-mode, in the grey circles the polarization corresponding to different dispersion relations is given [5] (courtesy of U. Stroth).

The way electromagnetic waves behave and interact with the plasma depends on a lot of aspects: hot plasmas behave different from cold ones, collisional different from non-collisional, unmagnetized different from magnetized and for the latter the wave even behaves different depending on its propagation direction relative to the background magnetic field. A wave is normally defined by its frequency f or its wavelength λ, here this will be expanded with a dispersion relation. Note that the frequency f, the angular frequency ω and associated period T are always linked one on one and therefore interchangeable, and the same is true for the wavelength λ and wave number k:

$$\omega = 2\pi f = \frac{2\pi}{T} \tag{2.7a}$$

$$k = \frac{2\pi}{\lambda} \tag{2.7b}$$

These properties can be linked with each other through the dispersion relationship:

$$\omega = \omega(k) \tag{2.8}$$

and through the phase and group velocities v_{phase} and v_{group}:

$$v_{\text{phase}} = \frac{\omega(k)}{k} \tag{2.9a}$$

$$v_{\text{group}} = \frac{\partial\omega(k)}{\partial k} \tag{2.9b}$$

Another important quantity is the refractive index N:

$$N = \frac{c}{v_{\text{phase}}} = \frac{kc}{\omega} \tag{2.10}$$

which is 1 in vacuum.

Depending on the function describing the dependency of the wavelength on the frequency (Eq. 2.8), the behaviour of the waves changes. In Figure 2.2 the dispersion relations for a cold unmagnetized (a) and magnetized (b) plasma with $\vec{k} \perp \vec{B}$ are presented. It can be seen that there are a lot of different possibilities for waves to exist in a magnetized plasma, each of them with a different $\omega(k)$. Only waves which have the correct combination of ω, k and polarization so that they lie on one of the lines in the figure can exist in the plasma.

The dotted line with red accent is present in both figures and is called the ordinary mode (O-mode) as opposed to the other curves displayed which are named X-modes or extraordinary modes. Along the magnetic fieldlines, particles in a plasma behave the same as if there was no magnetic field, thus, when a wave is linearly polarized is in this direction, the behaviour of the magnetized plasma is no different than in a non-magnetized plasma. This is the reason that the dotted line is identical for both unmagnetized and magnetized plasma and it explains its 'ordinarity'. The O-mode has the following dispersion relation and refractive index:

$$\omega^2 = k^2c^2 + \omega_{pe}^2 \tag{2.11}$$

$$N^2 = 1 - \frac{\omega_{pe}^2}{\omega^2} \tag{2.12}$$

Given O-mode polarized radiation with frequency ω, the refractive index $N^2 = 0$ when $\omega_{pe}(n_c) = \omega$. The density n_c for which this happens (Eq. 2.6) is called the cut-off density for ω. From Equation 2.12, it can be seen that for any density higher than the cut-off density, the refraction index becomes imaginary, and the wave can no longer propagate. The approach can also be reversed: given a fixed plasma density n_c, O-mode polarized radiation can only propagate through it if $\omega > \omega_{pe}(n_c)$. In Figure 2.2 (where the dispersion relation is drawn for a fixed ω_{pe}) this can be seen: for $\omega > \omega_{pe}$ the O-mode dispersion relationship exists so waves can propagate, for $\omega < \omega_{pe}$ this is not the case and waves are reflected instead. This agrees with what was seen in Section 2.1.2.

2.2 Microwave Components and Technology

2.2.1 Maxwell Equations

As PPR is based on on the propagation of electromagnetic radiation, it is convenient to use electric and magnetic fields instead of current and potential to describe electromagnetic behaviour. Therefore, Maxwell's equations are used to model the different components of the PPR. With $\vec{E}$ the electric field, $\vec{B}$ the magnetic field, $\vec{D}$ the displacement field, $\vec{H}$ the magnetizing field and the source terms $\vec{j}$ the electric current density, and ρ the electric charge density, the Maxwell equations become:

$$\vec{\nabla} \times \vec{E} = -\frac{\partial \vec{B}}{\partial t} \tag{2.13a}$$

$$\vec{\nabla} \times \vec{H} = \frac{\partial \vec{D}}{\partial t} + \vec{j} \tag{2.13b}$$

$$\vec{\nabla} \cdot \vec{D} = \rho \tag{2.13c}$$

$$\vec{\nabla} \cdot \vec{B} = 0 \tag{2.13d}$$

Depending on the boundary values set by the problem, different solutions, so-called eigenmodes, for the Maxwell equations are found.

An important solution of the Maxwell equations is the plane wave. It takes the following form for a wave with frequency ω and wavenumber k propagating through vacuum in the z-direction with electric field component E_x and magnetic field component H_y orthogonal on each other:

$$E_x = E \cdot e^{j(\omega \cdot t - k \cdot z)} \tag{2.14}$$

$$H_y = \frac{E_x}{Z_0} \tag{2.15}$$

with wave impedance $Z_0 = \sqrt{\frac{\mu_0}{\epsilon_0}}$

To characterize the power density of the wave, the Pointing vector $\vec{S}$ is introduced. The vector points in the direction of the power propagation and its amplitude equals the power:

$$\vec{S} = \mathrm{Re}(\vec{E} \times \vec{H}^*) \tag{2.16}$$

$$S = |\vec{S}| = \frac{|\vec{E}|^2}{Z_0} \tag{2.17}$$

2.2.2 Plasma Positioning Reflector Circuit

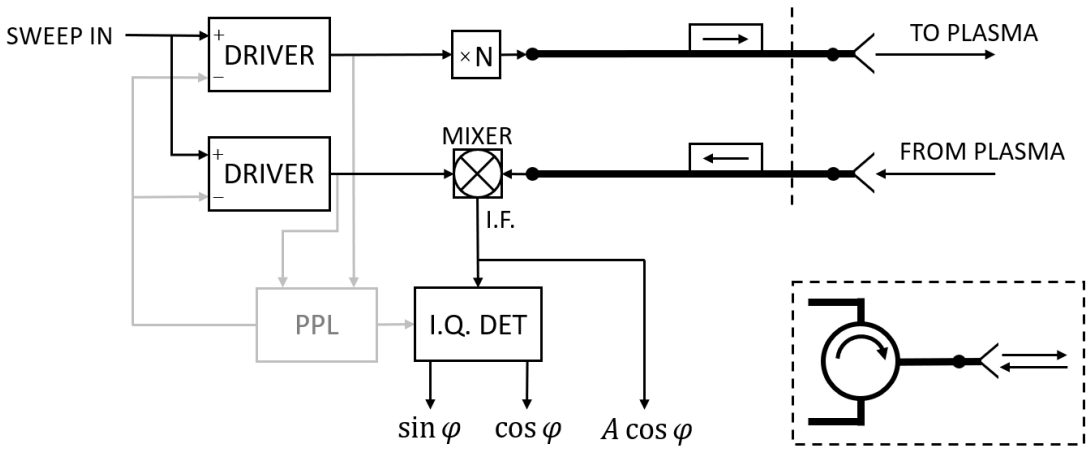

Figure 2.3: Schematic of a plasma reflectometer with heterodyne detection. By replacing the part right of the dotted line by the circuit in the dotted box, the bi-static setup becomes mono-static.

In Figure 2.3, a schematic representation of a plasma reflectometer with heterodyne detection [12] is given. By replacing the right part of the circuit by the circuit in the dotted box, the bi-static setup (meaning it uses separate antennas for emitter and receiver) becomes mono-static. The input given to the system is a required frequency sweep that is to be performed. In case of the PPR system for ITER, this would be a sweep from 15 GHz to 75 GHz. For the system that is considered in this thesis the range is limited to 30 GHz to 60 GHz. As will be explained in Section 2.3, this swept input will result in reflections on the density cut-off layers corresponding with the plasma frequencies of the input range. This system is called a Frequency-Modulated Continuous Wave (FM-CW) radar. The components that are used in this system and Figure 2.3 are [13]:

1. **DRIVER**: Wave generators that produce a stable frequency f' so that the probing frequency f is a multiple of f': $f' = f/N$

2. **PPL**: A Phase-Locked Loop provides feedback to the drivers so that the drivers always have the same phase.

3. **Frequency multiplier**: Multiplies the driver frequency to the probing frequency $f = f' \times N$.

4. **Coax-waveguide adapter**: Transition between coax-line and waveguide transmission line.

5. **Waveguide** (thick line): Low-loss transmission line for the high-frequency signal. Detailed description in Section 2.2.2.1.

6. **Taper**: Transition between two waveguide sections. Detailed description in Section 2.2.2.2.

7. **Isolator** (box with arrow): Waveguide component which allows power to flow through in a single direction only. Power flowing in the opposite direction is dissipated.

8. **Circulator** (circle with arrow): In the mono-static circuit, a circulator is used to separate the transmission and receiver circuits. Circulators are waveguide components with three ports (a), (b), (c). Power coming from port (a) will be leaving through port (b), power coming from port (b) leaves through port (c) and power coming from port (c) leaves through port (a).

9. **Antenna**: Transition between transmission line and free-space radiation. Detailed description in Section 2.2.2.3.

10. **MIXER**: Shifts the returning frequency to a lower intermediate frequency (I.F.) by mixing it with the second driver signal.

11. **I.Q. DET**: In-phase/Quadrature detection in which the phase-locked loop signal is used as reference with which the I.F. signal is compared. From this the real (in-phase) and imaginary (quadrature) part of the returning signal can be found. Without I.Q. detection, only the real part of the signal would be known with no means to obtain phase and amplitude separately.

2.2.2.1 Waveguides

To make a correct interpretation of any measurement, it is necessary to have a sufficiently high signal-to-noise ratio. Therefore, noise levels and signal losses need to be kept as low as possible. Because the distance between the tokamak, where the antennas are located, and the place where the signals are generated and processed will be around 100 m in ITER, low loss transmission lines are required for the PPR. Waveguides, having lower losses than coax-cables, can be used for this. Unlike coax-cables, waveguides have no dielectric component, this is another advantage since dielectrics are less resistant to the tokamak environment than metals.

Waveguides are hollow, metallic transmission lines that come in various shapes. Common are rectangular and cylindrical waveguides, either with smooth or corrugated walls [22]. Each of these imposes different boundary conditions to Maxwell's equations, resulting in different eigenmodes which can propagate in the waveguide. It depends on the dimensions of the waveguide, whether or not a certain

Table 2.2: Cut-off frequencies in a smooth-wall cylindrical waveguide with $D = 8\,\text{mm}$. Two modes can propagate for the whole bandwidth of 30 to 60 GHz, four more modes can propagate for the part of the bandwidth with $f > f_c$.

mode	TE_{11}	TM_{01}	TE_{21}	TE_{01}	TM_{11}	TE_{31}	TM_{21}	TE_{41}
f_c (GHz)	21.96	28.69	36.43	45.71	45.71	50.11	61.26	63.43

frequency is able to travel through it. The dimensions set a lower frequency limit for each eigenmode. The eigenmode which has the lowest frequency limit is called the fundamental mode. This means that a waveguide is only usable for frequencies $f > f_c$ with f_c the cut-off frequency of the fundamental mode.

In waveguides with smooth walls, the modes which can propagate are the TE and TM modes, standing for transversal electrical respectively transversal magnetic fields (with respect to the propagation direction). This opposed to the TEM modes, which have transversal electrical and magnetic fields, like the plane wave which was introduced before, and which propagate in free space. In corrugated waveguides the eigenmodes are hybrid modes HE which are superpositions of TE and TM modes. Modes are characterized by two indices. A TE_{mn} in a rectangular waveguide with cross-section in the (x,y)-plane is a mode with a transversal electric field with m extrema in the electric field in the x-direction and n extrema in the y-direction. The interpretations in cylindrical waveguides is analogous but now in the (r,ϕ)-plane, with indices standing for the number of radial and angular maxima instead.

TE_{mn}- and TM_{mn}- eigenmodes in a smooth-walled cylindrical waveguide with radius a have the following cut-off frequency:

$$f_c^{\text{TM}} = \frac{c j_{mn}}{2\pi a} \tag{2.18a}$$

$$f_c^{\text{TE}} = \frac{c j'_{mn}}{2\pi a} \tag{2.18b}$$

With j_{mn} the n^{th} zero of the m^{th} Bessel-function and j'_{mn} the n^{th} zero of the first derivative of the m^{th} Bessel-function. The cylindrical waveguide with diameter $D = 8\,\text{mm}$ that will be used in Chapter 5 and Chapter 6 can be used as an example. This waveguide is used in frequency range 30 to 60 GHz. The cut-off frequencies for the modes with the lowest f_c are given in Table 2.2. It is seen that for this type of waveguide TE_{11} is the fundamental mode and that apart from this mode also TM_{01} can propagate for this bandwidth. The modes TE_{21}, TE_{01}, TM_{11} and TE_{31} can propagate for part of the bandwidth.

A smooth-walled rectangular waveguide with dimensions a, b ($a > b$) has fundamental mode TE_{10}. The cut-off frequency of this mode is:

$$f_c = \frac{c}{2a} \tag{2.19}$$

2.2.2.2 Tapers

In Table 2.2 it is seen that multiple modes can propagate in the waveguide used for PPR, especially for the high end of the bandwidth. When a perfect

TE_{11} mode is launched in a perfect version of this waveguide, only this mode will propagate, however, when the waveguide is fed from a coax-cable or from a previous waveguide with a different shape the transition to the used waveguide can introduce higher-order modes that have $f_c < f$. Another unwanted effect are power reflections at the transition. To reduce both power reflections and higher-order modes, tapered waveguide sections can be used when a transition between waveguides is made. The tapered section changes the dimension of the waveguide gradually, which can be thought of as providing a smoother transition of the boundary conditions of the Maxwell equations, lowering the high-order mode fractions and power reflections.

2.2.2.3 Antennas

Antennas provide a transition from electromagnetic fields propagating through a transmission line to free space (emitter) and vice versa (receiver). The antennas used in this work are horn antennas, an example is depicted in Figure 2.4a. Horn antennas use a waveguide as incoming transmission line and typically have a diverging horn, although more exotic shapes are possible as well. It is also possible to use an open-ended waveguide (without diverging section) as antenna. Just like tapers, antennas aim to make a good transition between two sets of boundary conditions of the Maxwell equations so that a high mode purity of the wanted TEM-mode is obtained.

It will be seen in Chapter 4 that the width of the radiated beam is crucial for the performance of a PPR antenna: a too narrow beam has the risk of not being reflected towards the receiver, a too wide beam has the risk of not reflecting powerful enough signals to the receiver. Whatever the plasma conditions, the signals received by the receiver antenna should be higher than a noise threshold to enable an accurate position reconstruction. Several horn antennas are to be tested to assess their performance. For this, analytical descriptions of the electric fields of these antennas are necessary. TEM modes, also called Gaussian modes, are the non-planar free-space propagating solutions of the Maxwell equations and analytical formulas of their radiated fields exist, so that antennas launching these modes can be easily modelled and their performance tested.

Gaussian Beams

The electric field of a fundamental Gaussian beam with wavelength λ takes the following form for a wave propagating in the z-direction in cylindrical coordinates [23]:

$$E(r,z) = \left(\frac{2}{\pi w^2}\right)^{0.5} \exp\left[\frac{-r^2}{w^2} - jkz - \frac{j\pi r^2}{\lambda R} + j\phi_0\right] \tag{2.20}$$

with w the beam radius, R the radius of curvature and ϕ_0 the Gaussian beam phase shift at the given (r,z) coordinates, which are defined by the following formulas and graphically defined and illustrated together with the Gaussian beam propagation in Figure 2.4b.

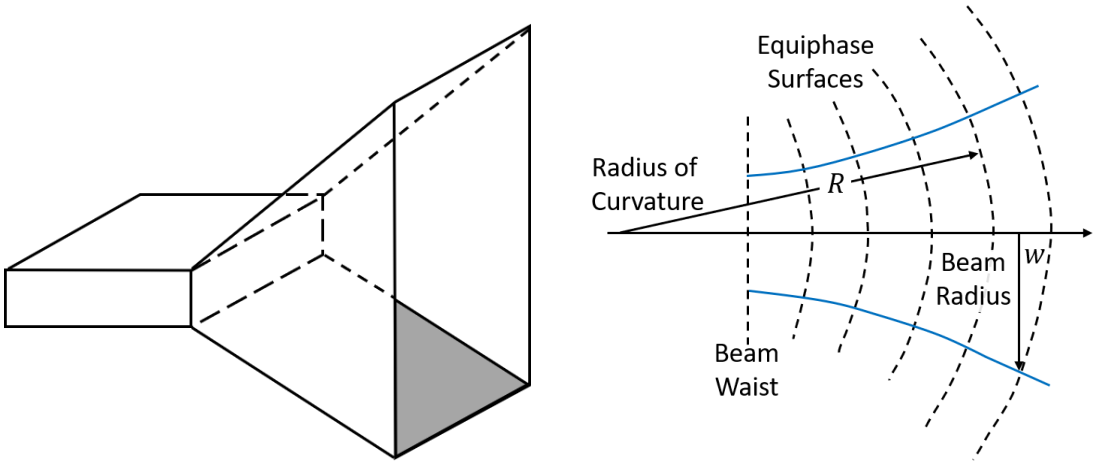

(a) (b)

Figure 2.4: (a) typical horn antenna fed by a rectangular waveguide, (b) propagation of fundamental Gaussian beam, illustrating the definitions of radius of curvature R, beam radius w and equiphase surfaces, also known as phase fronts [23].

$$R = z + \frac{1}{z}\left(\frac{\pi w_0^2}{\lambda}\right)^2 \tag{2.21a}$$

$$w = w_0\left[1 + \left(\frac{\lambda z}{\pi w_0^2}\right)^2\right]^{0.5} \tag{2.21b}$$

$$\tan\phi_0 = \frac{\lambda z}{\pi w_0^2} \tag{2.21c}$$

with w_0 the beam waist, which is the beam radius at the position where the beam is the most narrow. Using these formulas it suffices to know the location and size of the beam waist w_0 and the frequency f of the beam (corresponding to λ) to fully characterize the electrical field.

From Equation 2.20 it is clear that the beam radius w is the value of the radius at which the field falls to $1/e$ relative to its on-axis value. This makes it a good measure for the divergence of the beam as can be seen in Figure 2.4b. Another useful quantity that can be defined is the confocal distance z_c:

$$z_c = \frac{\pi w_0^2}{\lambda} \tag{2.22}$$

The confocal distance can for example be used to rewrite Equations 2.21.

Also higher-order Gaussian modes, called Gauss-Laguerre modes in cylindrical coordinates, exist. The electric field of the cylindrical symmetric modes TEM_{p0} can be described using the ordinary Laguerre polynomials L_p [23]:

$$E_{p0}(r,z) = \left(\frac{2}{\pi w^2}\right)^{0.5} L_p\left(\frac{2r^2}{w^2}\right)\exp\left[\frac{-r^2}{w^2} - jkz - \frac{j\pi r^2}{\lambda R} + j(2p+1)\phi_0\right] \tag{2.23}$$

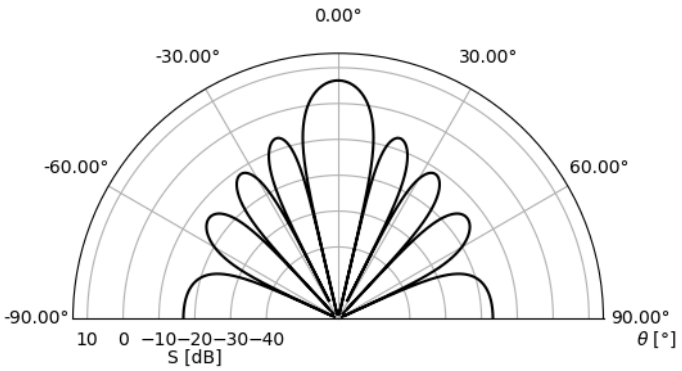

Figure 2.5: H-plane radiation pattern of horn with rectangular aperture. Apart from the central main lobe, several sidelobes are present.

Antenna Characteristics

Several antenna characteristics will be of importance in this work [24]:

1. **Reciprocity**: Passive, linear antennas, such as those used in a PPR circuit, have the same characteristics when they are used as emitter and as receiver.

2. **Radiation diagram**: Also called radiation pattern or antenna diagram, the radiation diagram is a 3D plot on which the radiated power density S is given as function of the radiation direction. Normally 2D section cuts are drawn in different directions and for different polarizations. Because of symmetry, a few of these 2D diagrams often suffice to characterize the antenna. Figure 2.5 gives an example of a 2D radiation diagram for a horn with rectangular aperture.

3. **Main and side lobes**: On Figure 2.5, multiple lobes in which the power is radiated are visible: centrally a large main lobe exists, which radiates most of the power in the wanted direction. However, a lot of sidelobes, radiating in different directions, are present. For an emitter, the side lobes cause power losses. For a receiver, it will be impossible to determine whether received power came from the direction of the main lobe or from the side lobe.

4. **Co- & cross-polarization**: An antenna will be made such that the main part (ideally 100 %) of its power is polarized so that it is useful for the application. Any radiation with different polarization will lead to unwanted behaviour of the antenna and power losses. Radiation with the correct polarization is co-polarized, other radiation is cross-polarized.

5. **Directivity & Gain**: Directivity D is a measure of the maximum power density relative to the uniform power density of an isotropic source S_{iso} in dB scale. Gain is defined as the directivity multiplied by the electronic efficiency.

$$D = 10 \log_{10} \frac{\max(S)}{S_{\text{iso}}} \tag{2.24}$$

Decibel scales are common in radio frequency engineering. Conversion between this scale and linear scale happens by:

$$S_{[\mathrm{dB}]} = 10 \log_{10} S_{[\mathrm{linear}]} \tag{2.25}$$

When combined with Equation 2.16, dB-scales can also be used for electric fields directly (then the factor 10 in the above formula needs to be replaced by 20).

Far-Field

In function of the distance from an antenna with characteristic size D (for an aperture antenna D is the largest aperture dimension), three regions can be distinguished. In the reactive near-field region ($r < R_1 = 0.62\sqrt{D^3/\lambda}$), the reactive field dominates. The radiating near-field or Fresnel region ($R_1 < r < R_2$) is the region in which the radiation fields predominate but the angular field distribution (radiation diagram) is dependent on the distance from the antenna. The third region is the far-field region or Fraunhofer region ($r > R_2$), in which the radiation fields are dominant and the angular field distribution is quasi independent of the distance from the antenna.

There are multiple criteria on where the far-field starts [24, 25]:

$$R_2 = 2\frac{D^2}{\lambda} \tag{2.26a}$$

$$R_2 = 5D \tag{2.26b}$$

$$R_2 = 1.6\lambda \tag{2.26c}$$

In general the most strict criterion (largest R_2) can be used as a safe starting point of the Fraunhofer far field.

2.3 Plasma Positioning Reflectometry

2.3.1 O-mode Reflectometry

The considered PPR uses O-mode reflectometry. The radiation sent by the emitter has to be polarized as the O-mode branch displayed on Figure 2.2b (dotted line). Therefore polarization parallel to the magnetic field is needed. The magnetic field in a tokamak is approximately in the toroidal direction (Section 1.3), so the polarization should be in the toroidal direction as well[1]. The plasma positioning antenna can be placed anywhere around a poloidal cross-section to probe the distance from that point to the plasma. To get a full reconstruction of the plasma position, the plasma needs to be probed from all sides, so a full PPR consists of multiple circuits as in Figure 2.3. For ITER the plasma will be probed from four different poloidal locations [26]. Two of these positions, gap 4 and gap 6, contain in-vessel antennas such as those studied in this thesis.

From the plasma density profile (Eq. 2.2) and the O-mode dispersion relation (Eq. 2.11), Figure 2.6 can be constructed. The quadratic plasma density profile is

[1]The actual magnetic fieldlines are helical, not cylindrical and have a small offset opposed to the toroidal direction, this is not taken into account here.

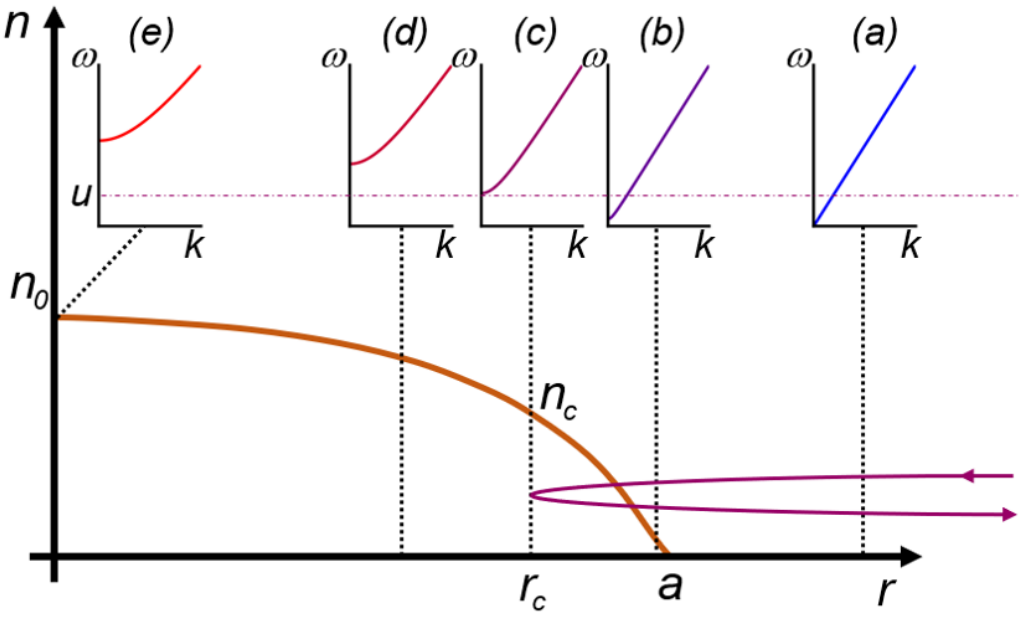

Figure 2.6: Plasma density profile and dispersion relations at different locations. The dotted purple line at frequency $\omega = u$ corresponds with the wave entering the plasma from the right. As long as the O-mode dispersion exists at this frequency ($\omega_{pe}(n(r)) < u$) the wave propagates, as soon as $\omega_{pe}(n(r)) \geq u$ the wave is reflected on the cut-off density layer $n(r_c) = n_c$.

given, together with the O-mode dispersion relation at different radial locations corresponding to different densities. On the figure, dispersion relation (a) at $n(r > a) = 0$ corresponds to vacuum propagation: $\omega = ck$. As soon as $n(r < a) \neq 0$, the intersection of the dispersion relation with the $k = 0$ axis is no longer zero ($\omega(k = 0) = \omega_{pe} = \sqrt{\frac{e^2 n}{\epsilon_0 m_e}} \neq 0$). This value keeps rising through dispersion relations (b), (c), (d) until (e) where maximum density n_0 and correspondingly the maximum ω_{pe} is reached. The asymptotic behaviour of all dispersion relationships for high k is $\omega = kc$, so that very high frequency waves propagate through the plasma as in vacuum. The dotted purple line at frequency $\omega = u$ in the dispersion diagrams corresponds with the drawn wave entering the plasma from the right. In the dispersion diagrams (a) and (b) this wave is situated at the intersections of the dotted line with the O-mode dispersion. In diagram (c) the plasma frequency equals u, meaning that the wave gets reflected at this density and radial position, as is illustrated in Figure 2.6.

In plasma positioning reflectometry, waves at various frequencies u are used, reflecting at different depths of the plasma. For this thesis, the octave 30 GHz to 60 GHz corresponding with cut-off densities between $1.164 \cdot 10^{19}\,\mathrm{m}^{-3}$ and $4.465 \cdot 10^{19}\,\mathrm{m}^{-3}$ will be used, although ITER plans to use a 15 to 75 GHz range [11]. By reducing the bandwidth, the making of a frequency-independent antenna which has good performance in this application, independent of the frequency or amount of turbulence, becomes easier. For a plasma with central density $n_0 = 10^{20}\,\mathrm{m}^{-3}$ and the main density profile described by Equation 2.2, using 30 GHz to 60 GHz means that the plasma between $r = 0.94a$ and $r = 0.74a$ is observed. For

plasma positioning it is sufficient to observe the outer layers of the plasma and make an estimate of the complete position of the plasma based on this. To get an accurate reconstruction it is necessary to observe the plasma beginning from the very side $r = a$. This is not possible with an O-mode reflectometer, as probing a density close to zero would require a frequency close to zero, which is technically impossible. In ASDEX Upgrade, this is done with an additional X-mode reflectometer working in frequency range $33 - 75\,\mathrm{GHz}$, which probes the plasma from $n(a) = 0$ [13].

2.3.2 Plasma Position Reconstruction

To be able to interpret the PPR signals, the time of flight t_{ToF} (the time between sending and receiving a signal of a certain frequency) needs to be extracted from the signals. From the measured phase difference ϕ between the send and the received signal (which is retrieved through I.Q. detection) it is possible to calculate t_{ToF}, if the measurement is done for a swept frequency range so that $\phi(f)$ is known [12]:

$$t_{\mathrm{ToF}} = \frac{1}{2\pi}\frac{\mathrm{d}\phi}{\mathrm{d}f} \tag{2.27}$$

When the plasma moves relative to the vacuum vessel in which the antenna is mounted, this results in a change in distance d between the edge of the plasma and the antenna aperture. This has a change in the ToF as consequence. To determine the distance d at different sides of the plasma corresponds with the most basic definition of locating the plasma in the vacuum vessel. Under the assumptions of a perfect quadratic density profile (Eq. 2.2) and a exactly known value for a and n_0, the measured time of flight t_{ToF} between sending and receiving the PPR signal can be used for obtaining d. The probing frequency f_c is known, and through the definition of plasma frequency (Eq. 2.6), the cut-off density n_c on which the wave reflects is known. With the density profile, also the position of this layer r_c can be calculated. From these quantities it is possible to calculate the total time between a wave with fixed frequency ω entering and the wave leaving the plasma (using Eqs. 2.9b, 2.11). With ω_{pe} a function of r, this becomes:

$$\begin{aligned} v_{group} &= \frac{\partial\omega(k)_{O-mode}}{\partial k} \\ &= c\sqrt{1 - \frac{\omega_{pe}^2}{\omega_c^2}} \\ &= c\sqrt{1 - \frac{n(r)e^2}{\omega_c^2\epsilon_0 m_e}} \end{aligned} \tag{2.28}$$

$$t_{\mathrm{ToF,\ plasma}} = 2\int_{r=a}^{r=r_c} \frac{\mathrm{d}r}{v_{group}(r)} \tag{2.29}$$

The remaining time

$$t_{\mathrm{ToF,\ vacuum}} = t_{\mathrm{ToF}} - t_{\mathrm{ToF,\ plasma}} \tag{2.30}$$

results from the propagation in vacuum between antenna and plasma. Assuming that the distance emitter-plasma and plasma-receiver are the same, d is found:

$$d = \frac{c}{2t_{\text{ToF, vacuum}}} \tag{2.31}$$

This is only correct for a perfect plasma as described by the assumptions. In reality the plasma density is not perfectly known, but has (possibly large) turbulence δn and in addition the plasma shape and central density are possibly not known (such that n_0 and a are not fixed). This means that contrary to the previous assumption, r_c is not known in advance and has to be determined using PPR.

To determine r_c, an Abel inversion is used [12]:

$$r_c(f_c) = \frac{c}{\pi} \int_0^f {}_c t_{\text{ToF}}(f) \frac{\mathrm{d}f}{\sqrt{f_c^2 - f^2}} \tag{2.32}$$

With r_c and the corresponding (known) n_c, a density profile reconstruction can be made. Equations 2.27 and 2.32 show the need for frequency-swept density measurements to start at $f = 0$. It is of course not reasonable to use a continuous range of frequencies, instead measurements are often done at 2000 frequencies in a range (which for the 30 to 60 GHz band would correspond with steps of 15 MHz).

2.3.3 Blanket-Equipped Tokamaks

In a blanket-equipped tokamak, the PPR antennas have to be positioned in the space between two blanket modules which surround the plasma. Two problems have been identified here. The first is that the metallic blankets function as an elongation of the antenna, so that the actual antenna is the combination of antenna and blankets, leading to different characteristics. For some frequencies this effect alone is sufficient to prevent the PPR system from working in the allowed 1 cm error margin [11]. A second, closely related effect comes from the interplay of the blanket structures and the turbulent plasma, resulting in multi-reflections which can deflect the main lobe away from the antenna axis so that the power does not return to the receiver or does return but heavily perturbed [15, 27]. The multi-reflection effects can be seen[2] in Figure 2.7 which shows different scenarios of the plasma edge region probed by PPR waves. In the figure density lines in the plasma are shown (the plasma center has $n(0,0) = 10^{20}\,\mathrm{m}^{-3}$). The probing rays at $f = 30\,\mathrm{GHz}$ are reflected in the same region, but depending on the turbulence, their path changes. As a result, they sometimes return to the receiving antenna without any spurious effects (a), with parasitic reflections (b) or with parasitic reflections causing a path which passes multiple times through the plasma (c). Each parasitic reflection on the metallic walls causes an additional 180° phase shift. Apart from this, each passage through the plasma results in an additional phase shift. These multi-reflections make it impossible to obtain a correct t_{ToF} so that Eq. 2.32 cannot be used to get a plasma density profile.

[2] A definition of the radiation pattern SINC14 used in Figure 2.7 is given in Eq. 3.16, a definition of turbulence levels is given in Section 3.4.1.

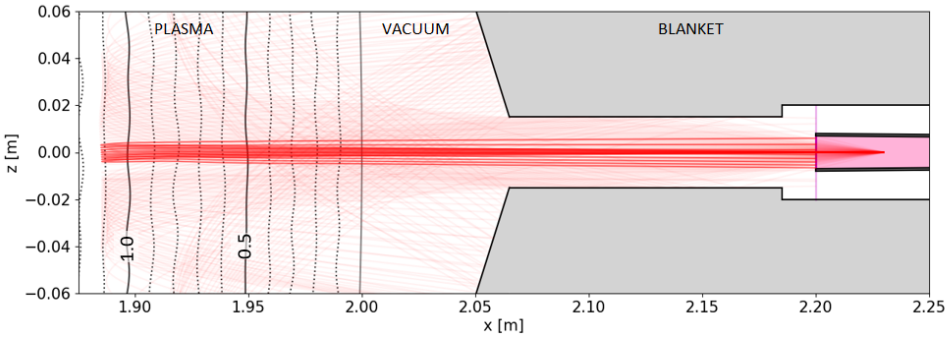

(a) 1 % turbulence: no multi-reflections.

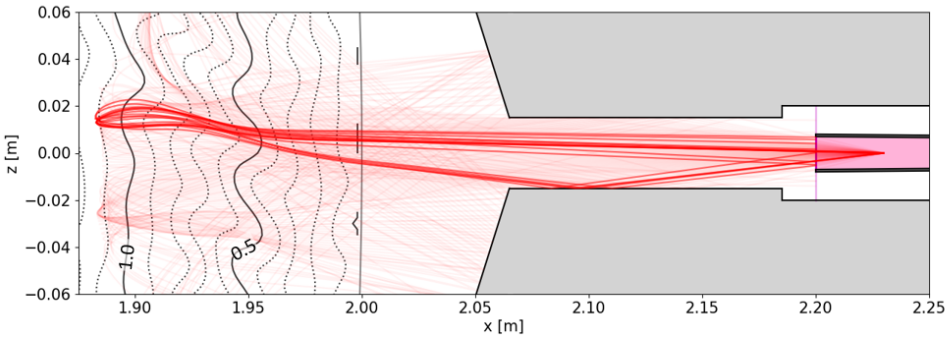

(b) 5 % turbulence: parasitic reflections on lower blanket.

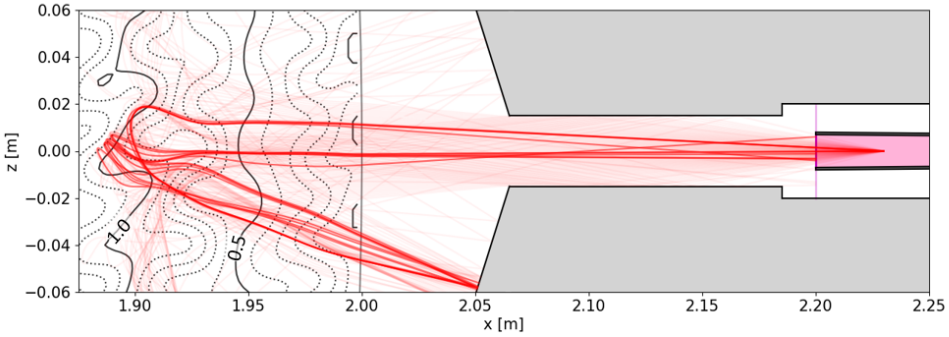

(c) 10 % turbulence: rays passing through the plasma twice before being received.

Figure 2.7: R2P2 (see Chapter 3) simulation results showing multi-reflection effects. A set of rays (red) is launched from the antenna (pink, aperture at $x = 2.20\,\mathrm{m}$), when they return to the receiver rays are bright red. The turbulent plasma (density contours given in $10^{19}\,\mathrm{m}^{-3}$) and reflective blanket modules (grey) create multi-reflection effects. For all simulations the radiation pattern SINC14 at 30 GHz (associated with a cut-off density $n_c = 1.12 \cdot 10^{19}\,\mathrm{m}^{-3}$) is used.

Although the Abel inversion cannot be used, it might be possible to use more modern plasma position reconstruction methods. Already for the PPR system in ASDEX Upgrade (which does not suffer from the described blanket effects, since no blankets are present) the computationally intensive Abel inversion is not done but replaced by a neural network to make real-time feedback possible [16]. For a different application, similar database methods are being investigated [17] to help with difficult plasma reconstructions. In these methods full-wave simulations (field simulations which model the complete plasma and environment) are used

to train a model which can perform the reconstructions. When using such a technique for PPR for ITER, the model should be able to recognize signature signals from certain effects (such as those in Fig. 2.7) and make a reconstruction taking into account how these effects influence the received signals.

Unfortunately, the complexity of the given PPR problem is vast. Turbulence is inherently unpredictable, so for a given type and amount of turbulence there are many different outcomes of the multi-reflections effects. Additionally there exist multiple types of turbulence, causing again many different possible results. Also, the radiation diagram of the ITER PPR antennas changes depending on frequency [19], and for different radiation diagrams, the turbulence can have different effects [28]. This causes a convolution of the spatial correlation of the turbulence with the effects of the changing radiation pattern, complicating the plasma position reconstruction even further. Each of these factors: turbulent randomness, turbulence type, turbulence level, and antenna pattern cause a multiplication in possible tendencies which the model should identify and handle properly. It is feared [18] that the sheer amount of tendencies to identify will be too big, so that real-time feedback for the position control system, even with these modern methods, won't be possible.

There are only few possibilities to solve this problem. The ITER blankets and the first wall encounter very high heat loads and their shape and position needs to be as they are for thermal protection. For future devices, a re-design of the blanket shapes, reducing the multi-reflections might be possible [15, 27]. The other possibility is to try to reduce the computational effort of the reconstruction, so that a neural network/database reconstruction method is possible after all. As most of the complexity of the problem comes from turbulence, the only aspect which can be fully controlled is the antenna diagram. The studies that have been made on antenna optimization for the ITER PPR system always considered the use of pyramidal horn antennas [19, 29], and aimed at optimizing the antenna coupling to maximize the receiver power, but did not attempt any optimization regarding the shape of the radiation pattern.

In the next chapters will be looked at if and how changes to the antennas can be made such that antenna behaviour is less frequency dependent and the performance of the antenna for the PPR application is still good. If it is possible to find such an antenna, the number of tendencies which the future model needs to identify can be lowered drastically, and the models speed and performance can be increased. This work is preliminary to the actual design of such a model, as it is assumed, based on the results of the same approach in different reflectometry fields, that without reducing the complexity of the problem, the neural network or database approach will not be successful.

Chapter 3

R2P2: a Ray Tracing Reflectometry for Plasma Positioning Code

R2P2 stands for **R**ay tracing **R**eflectometry for **P**lasma **P**ositioning. It is a **2** dimensional simulation code, which simulates an antenna (defined by its radiation pattern), turbulent plasma and metallic surroundings such as blankets. The code was developed in this study in order to investigate the multi-reflection effects that occur when a plasma positioning reflectometer (PPR) is used in blanket-equipped tokamaks and to assess the influence of the antenna choice on these effects as well as the overall performance of different antennas for this application. In the previous chapter, Figure 2.7 showed results of three R2P2 simulations. Apart from single simulations, the code can be run multiple times for a given set of parameters, each time with a different turbulence phase matrix, so that an ensemble is obtained from which statistically significant results about the behaviour of the antenna can be derived. In this chapter, the R2P2 description for a single simulation will be developed. The statistical post-processing methods that transfer the simulation results to interpretable data and figures will be discussed in Chapter 4, as the results of the R2P2 simulations done for this research are being presented. The R2P2 code considers only forward scattering, meaning that long spatial variation of the turbulence is assumed compared to the local wavelength. The ray tracing technique will first be introduced. A second section discusses the assumptions and limitations of the code. Consequently the modelling of the different parts of the code will be explained. Finally, pseudocode of the main code is given and some techniques used to minimize computational complexity are listed.

Note: The coordinate system defined in Figure 2.1 is kept. This means that for all R2P2 simulations and images shown, (x, z) defines the poloidal plane which is represented in the plane of the page, and y is in toroidal direction, pointing in the plane of the page. x is the horizontal coordinate and z the vertical coordinate.
Note: For variables f which are ray dependent, the following indices will be used: f_p^i, f_p^l or $f_p^{(i,l)}$ in which p represents the propagation step/state number (starting at $p = 0$ at initialization), i represents the ray number and l stands for the lobe number. The central lobe has $l = 0$, primary sidelobes ± 1, etc.

3.1 Ray Tracing versus Full-Wave

R2P2 is a ray tracing code, which uses rays to represent the electromagnetic radiation, unlike full-wave (FW) codes, which simulate the complete field evolution in space or space and time. Each ray travels a straight path in vacuum until it meets an object with which it interacts, causing the ray to reflect, diffract, ... after which it continues propagating. Phase coherency between neighbouring rays and beam divergence are not taken into account. Ray tracing is a well-developed technique, used in a number of different fields [30] such as CGI for movies or video-gaming, where it is provides realistic real-time imaging for ever-moving characters. Also for mapping radio communication [31] and for plasma reflectometry [32], ray tracing is often used. Ray tracing is the technique par excellence to obtain fast results for a given situation, opposed to FW simulations, which are more time-consuming but give generally more accurate results.

Chaudhury and Chaturvedi compared full-wave and ray-tracing methods [32] and found that for a cold, collisional, unmagnetized plasma, ray tracing gives accurate results if the density gradient length L of the plasma is long compared to the free-space wavelength λ_0 of the rays. A formula for the density gradient length L will be given in Equation 3.9, evaluating the condition shows it is satisfied on the whole frequency range:

$$L \approx 0.01\,\mathrm{m} > \frac{\lambda_0}{2\pi} \approx 0.0016\,\mathrm{m} \text{ for } 30\,\mathrm{GHz} \tag{3.1a}$$

$$L \approx 0.6\,\mathrm{m} \gg \frac{\lambda_0}{2\pi} \approx 0.0008\,\mathrm{m} \text{ for } 60\,\mathrm{GHz} \tag{3.1b}$$

The study also points out that FW codes (however accurate they can describe refraction and absorption effects), are computationally expensive, especially for parametric studies, as will be done with R2P2, and that in this cases ray tracing is the advised method. This justifies the use of ray tracing.

Apart from the computation time, the ray tracing code has the advantage that each received ray has a completely known trajectory. This knowledge can be used to obtain insight in what part of an antenna diagram is responsible for certain effects, as can be seen in Figure 2.7. This type of information is not present in the full-wave output. A disadvantage is that ray tracing codes process only a single frequency at once, whereas FW codes can return resulting fields for multiple frequencies in a single simulation, making it possible for FW codes to use realistic signal processing to extract the plasma position using Eqs. 2.27 and 2.32 (frequencies can be close to each other, resembling a continuous frequency scan). Adding more frequencies to a time-domain FW code does not make the calculation more time-consuming. To obtain a high enough resolution to apply the Abel inversion (Eq. 2.32) to reconstruct the plasma position with a ray tracing code, the total amount of runs would be very high and the total time for this would possibly be bigger than of a single run of a full-wave code. For this reason, O-mode ray tracing codes are not suited for investigating position reconstructions.

The output of the R2P2 code does suffice to get a fast impression of the power that the antenna receives at different times and in combination with the

additional information about the rays trajectories, it is possible to use the code to investigate different antenna diagrams and improve them (whilst making sure that the input fields remain self-consistent regarding electromagnetism) for the application. Of course ray tracing codes which are able to do this might already exist, however these might be not as flexible towards the choice of input antenna diagram and they might not be as fast as a code specifically developed for this application. Also there is no guarantee that the constraints imposed by the surroundings (the presence of metallic objects in the vicinity of the launcher, the possibility to interact with the reflectometer, ...) can be easily satisfied with existing codes. These are sufficient reasons to build R2P2, a new ray tracing code specifically for the application of investigating antenna diagrams for PPR in blanket-equipped tokamaks.

3.2 R2P2 Layout

The content of the R2P2 code is represented in the flowchart in Figure 3.1. First R2P2 reads the settings regarding antenna diagram, used frequency, turbulence model and the geometry of the environment. After this, a turbulence (phase) matrix is generated for the simulation, guaranteeing a unique turbulent plasma for each simulation. R2P2 launches multiple rays for each lobe of the antenna diagram. Each ray undergoes a trajectory defined by the actual ray tracing. This process is given in the flowchart in Figure 3.2. The ray starts with a vacuum propagation in a straight line in its propagation direction. After some distance it will encounter an object, which can be a reflective blanket (causing a specular reflection), the plasma (in which the ray propagates and gets reflected at the cut-off layer), the (receiver) antenna aperture, or the domain edge (which ends the calculation). Depending on the object, a different function in the code handles the effect. The ray tracing in the plasma happens with a numerical solver, but all other effects are described analytically, making the code run faster than when a numerical solver would be used on the whole domain. When all rays have run through this process until the 'finish' block of Figure 3.2, R2P2 checks if there are areas in which more rays need to be launched to make sure that the spatial resolution is high enough to guarantee correct interpretation. The additional rays also run through the Figure 3.2 flowchart. After this, the received rays and the generated turbulence matrix are stored for post-processing.

The code is run 400 times with the same parameters. Since a random turbulence phase matrix is generated for each iteration, the results of the 400 simulations form an ensemble that can be used to draw conclusions on the average behaviour of the antenna for these settings.

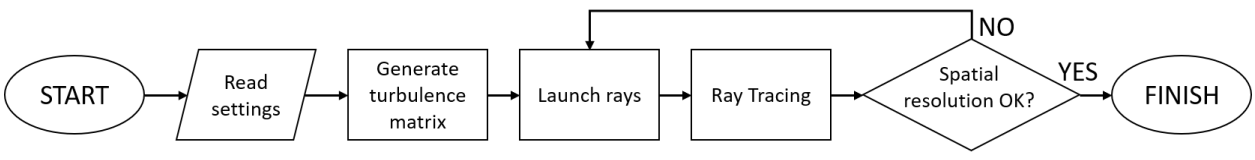

Figure 3.1: Flowchart of the main R2P2 code.

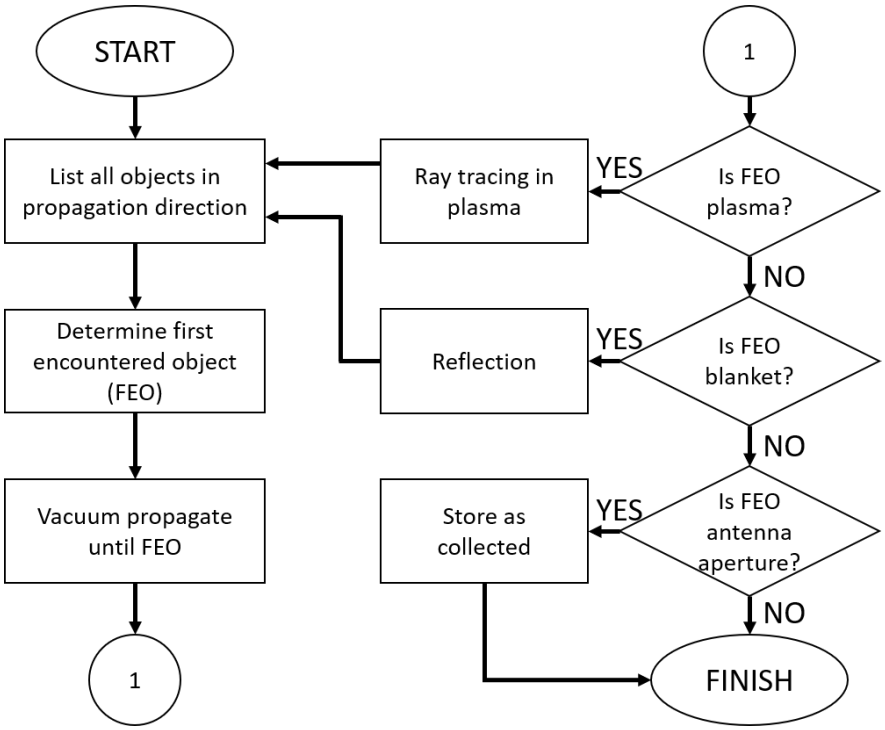

Figure 3.2: Flowchart of the ray tracing for a single ray. If the FEO (= first encountered object) is neither plasma, blanket, nor antenna aperture, the encountered object is the domain edge, causing a direct finish.

3.3 R2P2 Assumptions and Limitations

Apart from the inherent assumptions and limitations of a ray tracing code, which were discussed in Section 3.1, R2P2 has several other assumptions and corresponding limitations.

In R2P2 rays are assumed to be launched in O-mode polarization and it is assumed that the polarization does not change during the ray trajectory. This means that inside the plasma only the O-mode polarization dispersion relation is modelled.

The used ray tracing equations for ray tracing in a plasma [33] are based on a WKB approximation which is only valid when the density gradient length L is large compared with the probing wave wavelength. This condition was already verified in Eq. 3.1. The condition holds an important limitation of the code; when lower frequencies or steeper density profiles are used, the condition should be re-evaluated.

The wave numbers of turbulence density fluctuations in R2P2 are chosen to only include forward scattering of micro-instabilities in the range of $50\,\mathrm{rad/m} \leq k_{\mathrm{fluc}} \leq 2k_A^{30\,\mathrm{GHz}} = 174\,\mathrm{rad/m}$ (Section 3.4.1). This means that neither MHD effects (such as magnetic islands and tearing modes), corresponding with larger structures, nor Bragg backscattering, corresponding with smaller structures, are considered. Forward scattering occurs when broad fluctuations in the plasma cause deformations in the density profile and influence the reflections by the changes introduced in $n(x, z)$. Bragg backscattering occurs when an incoming

wave with $k(x, z)$ and a plasma fluctuation k_{fluc} are resonant such that the Bragg selection rule $k_{\text{fluc}} = 2k(x, z)$ is satisfied. The latter is accepted to be dominant in small and midsize devices with low turbulence levels, but in larger devices such as ITER, in which the turbulence conditions are different and turbulence levels can be high, forward scattering is expected to have major effects on spreading the probing beam [34]. It is this spreading of the beam that gives lead to the multi-reflections that R2P2 wants to study. This makes it a logical choice to implement a forward scattering plasma solver and turbulence model in R2P2. Since forward scattering uses a WKB framework, it is described well by a ray tracing code. It is possible to extend the code to also describe other scales of density fluctuations and the associated phenomena. For the Bragg backscattering this would require an associated Monte Carlo procedure.

It is assumed that the blankets surrounding the antenna act as perfect mirrors and cause specular reflections of the rays. This is only correct up to a certain point, as in reality the blankets act as elongation of the antenna, introducing possibly large changes in the radiation diagram [11].

Furthermore the radiation diagram is taken to be the far-field diagram at the antenna aperture. The reason for this is that the near-field region is located far away from the plasma and can be seen as a passive transition layer, playing no role in the measurements associated with the probing signal. A specific approximation (Section 3.4.2.2) is used to launch the rays using the far-field radiation diagram in a more appropriate way for simulations which are partly in the near-field, as is the case here.

The plasma is considered stationary, which is justified because the timescale of the simulation is a lot smaller than the smallest timescale for changes in the described plasma density fluctuations. In addition to this, the vacuum outside of the plasma is considered perfect.

For the moment, the code works with ITER-like plasma parameters as given in Table 2.1 and with an ITER-like PPR configuration for blanket sizes and antenna position, as given in Figure 3.3. The quantities d (the distance from the aperture to the plasma edge), h (the blanket interspace), and D (the antenna aperture size) can be chosen as parameters in the code. Choosing for ITER, rather than for DEMO parameters, makes sure that there are a lot of other studies available on different aspects of the PPR system. This means that more information is available on the problems encountered and comparison with other results is easier. However, by changing the parameters, R2P2 could easily be used for DEMO PPR simulations.

3.4 R2P2 Description

In this section, the procedures used for the main R2P2 code, corresponding to the flowcharts Fig. 3.1 and Fig. 3.2, are given in detail.

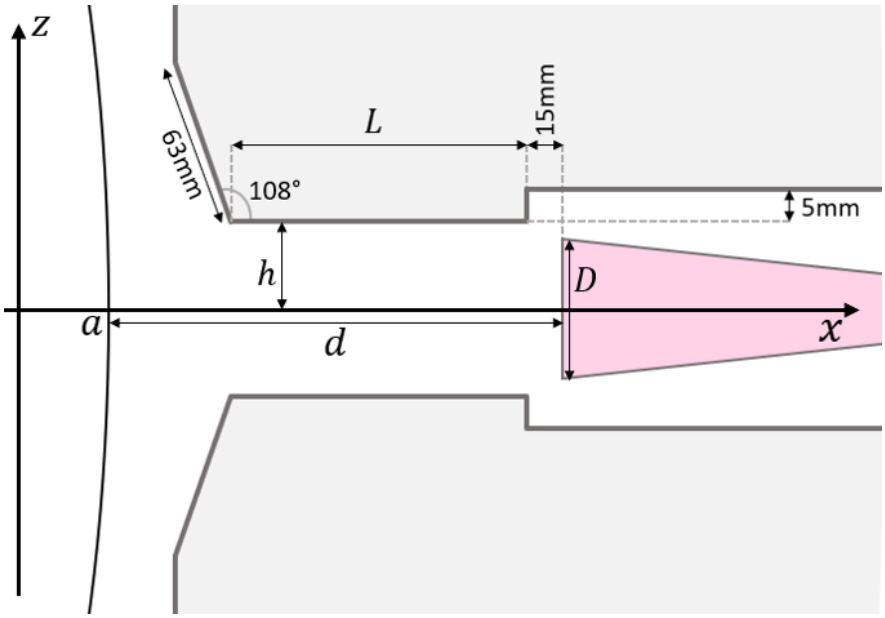

Figure 3.3: The geometry of the R2P2 setup based on the ITER setup studied by P. Valera, J.H. Belo and A. Silva [11, 35], defining the geometrical constants and parameters with D the antenna aperture and d the distance from the plasma edge to the aperture. h, the distance from the x-axis to the blanket, is set to 15 mm while L, the length of the narrow part of the blankets, is 120 mm.

3.4.1 Turbulence Model

An incoming wave with frequency ω and wave number $k(x, z)$ ($k_0 = \omega/c$ in vacuum) is considered, fluctuations in the plasma are assumed sinusoidal with wave number k_{fluc}.

The density fluctuation model δn is assumed homogeneous and is built from a superposition of density fluctuations, each with a certain $\vec{k}_{\text{fluc}} = k_{\tilde{x}}\vec{e}_{\tilde{x}} + k_{\tilde{z}}\vec{e}_{\tilde{z}}$ ($k_{\text{fluc}} = \sqrt{k_{\tilde{x}}^2 + k_{\tilde{z}}^2}$), in which $(\tilde{x}, \tilde{z})$ are coordinates used for a slab model description as depicted in Figure 3.4a, which neglects the (slight) curvature of the plasma. The resulting density perturbation model is given by [36]:

$$\delta n_{\text{turb}}(\tilde{x}, \tilde{z}) = \sum_{i=i_m}^{i_M} \sum_{j=j_m}^{j_M} A(i,j) \cos[k_{\text{fluc},\tilde{x}}(i)\tilde{x} + k_{\text{fluc},\tilde{z}}(j)\tilde{z} + \phi(i,j)] \tag{3.2}$$

$A(i, j)$ is a realistically chosen amplitude spectrum. Indices (i, j) run the summation through all possible wavenumber combinations within a certain range and $\phi(i, j)$ is a random generated phase. It is the choice of $\phi(i, j)$ that is unique for each R2P2 simulation and it is generating this quantity that is meant with choosing a turbulence matrix in the flowchart Fig. 3.1.

Although the slab models representation is very good, with a small change, this model can be transformed into a more realistic polar model (with a at fixed r instead of a at fixed $\tilde{x}$). This is illustrated in Figure 3.4b. The used coordinate

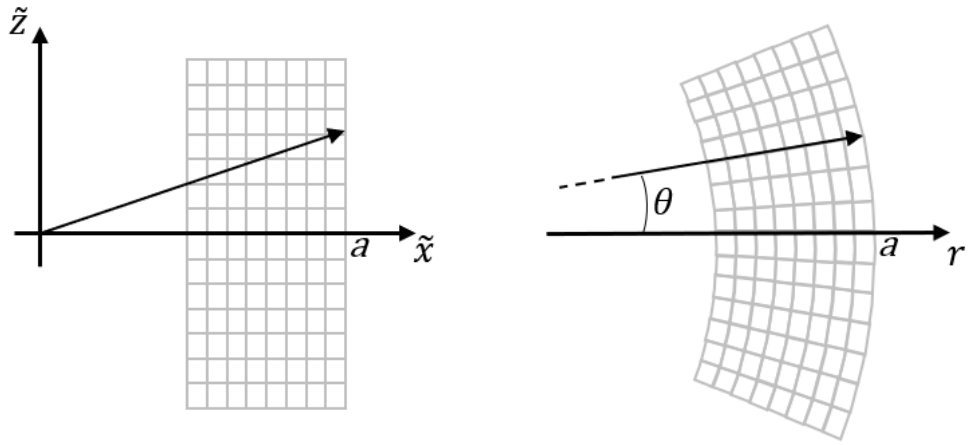

(a) (b)

Figure 3.4: Slab model (a) and polar model (b) for including turbulence in the density profile. The simplified slab model neglects the curvature of the plasma edge, which is taken into account in the polar model.

transformation is:

$$\tilde{x} = r \tag{3.3a}$$

$$\tilde{z} = \theta r \tag{3.3b}$$

The transformation is valid when the spatial dimensions are large compared to the wavelengths associated with the fluctuations in the plasma and $\tilde{z} \ll a$. The resulting model is

$$\delta n_{\text{turb}}(r,\theta) = \sum_{i=i_m}^{i_M} \sum_{j=j_m}^{j_M} A(i,j) \cos[k_{\text{fluc},r}(i) r + k_{\text{fluc},\theta}(j)\theta r + \phi(i,j)] \tag{3.4}$$

To use Equation 3.4, $A(i,j)$ and the range of used wavenumbers still need to be determined. In Section 3.3 it was chosen to only model forward scattering processes (and no Bragg backscattering) in R2P2. The range of fluctuation wavenumbers will be chosen accordingly. An upper limit for the wavenumber range in which forward scattering is dominant is [37]:

$$k_{\text{fluc}} < 2k_A \tag{3.5}$$

with the Airy wavenumber k_A:

$$k_A = 0.63 k_0^{2/3} L^{-1/3} \tag{3.6}$$

The density gradient length L at the cut-off $n_c(r_c)$ is defined as:

$$\frac{n(r)}{n_c} = 1 - \frac{r}{L}\ , \tag{3.7}$$

for a linear density profile [37]. It is possible to make a more general definition of L using the local slope of the density profile at the cut-off layer $n_c(r_c)$:

$$L = -n_c \cdot \left(\frac{\mathrm{d}n}{\mathrm{d}r}\Big|_{r_c} \right)^{-1} \tag{3.8}$$

Applied to the quadratic density profile

$$L = \frac{n_c}{n_0}\frac{a^2}{2r_c} \tag{3.9}$$

is found.

With these definitions the Airy wavenumber in ITER conditions ($a = 2\,\mathrm{m}$, $n_0 = 10^{20}\,\mathrm{m}^{-3}$) is found to be $k_A = 87.01\,\mathrm{rad/m}$ for 30 GHz ($k_0 = 629\,\mathrm{rad/m}$, $r_c = 1.885\,\mathrm{m}$, $n_c = 1.12 \cdot 10^{19}\,\mathrm{m}^{-3}$) and $k_A = 94.15\,\mathrm{rad/m}$ for 60 GHz ($k_0 = 1257\,\mathrm{rad/m}$, $r_c = 1.487\,\mathrm{m}$, $n_c = 4.46 \cdot 10^{19}\,\mathrm{m}^{-3}$). To allow for a fair comparison between different frequencies ω, it is the most interesting to have a fixed range of plasma fluctuations in the model, meaning k_A should be fixed on the complete range. The lowest value for k_A, found when using 30 GHz, was chosen.

A lower limit to the fluctuation wavenumbers was chosen at $k_{\mathrm{start,fluc}} = 50\,\mathrm{rad/m}$, leaving out MHD turbulence such as tearing modes and magnetic islands which have lower fluctuation wavenumbers, so that only microturbulence is studied by R2P2. The resulting turbulence model has wave numbers in the range:

$$50\,\mathrm{rad/m} \leq k_{\mathrm{fluc}} \leq 2k_A^{30\,\mathrm{GHz}} = 174\,\mathrm{rad/m} \tag{3.10}$$

For the amplitude $A(i,j)$ associated with each considered fluctuation (i,j), a cubic decay [5] is used:

$$A(k_{\mathrm{fluc}}) = \frac{B}{(k_{\mathrm{fluc}} - C)^3} \tag{3.11}$$

in which B and C are constants which adjust the shape of the decay and the turbulence level. To limit the calculation time for Equation 3.4, only 22 different values of k_r and k_θ were considered ($i_m, j_m = -11$, $i_M, j_M = 11$, resulting in $22^2 = 484$ different fluctuations taken into account in the model). When more modes (values of k_r and k_θ) were to be considered, an inverse Fourier transform should be used instead of Equation 3.4 to speed up the calculations. With $C = 20$ and B chosen to result in a maximum amplitude $A(k_{\mathrm{start,fluc}}) = 1$, this results in a model which is in close agreement (both in used range for the fluctuations as in amplitude) with the forward scattering model used by F. da Silva [36] for a Doppler reflectometry study, as is seen in Figure 3.5.

Combining the quadratic main density profile n_{main} (Eq. 2.2) with the density fluctuation model (Eq. 3.4 with the range of used k_{fluc} values defined by Eq. 3.10 and the amplitude spectrum by Eq. 3.11) results in:

$$n(r,\theta) = n_{\mathrm{main}}(r) + \delta n(r,\theta) \tag{3.12}$$

For the edge regions, the above formula can result in negative density values (as $\delta n < 0$ is possible), these negative values are set to zero. Different levels of turbulence will be simulated in R2P2. This can be done by scaling δn appropriately. To quantify the amount of turbulence, the percentage of turbulence is defined relative to the cut-off density at 30 GHz:

$$\frac{\delta n^{\mathrm{RMS}}}{n_c^{30\,\mathrm{GHz}}} \tag{3.13}$$

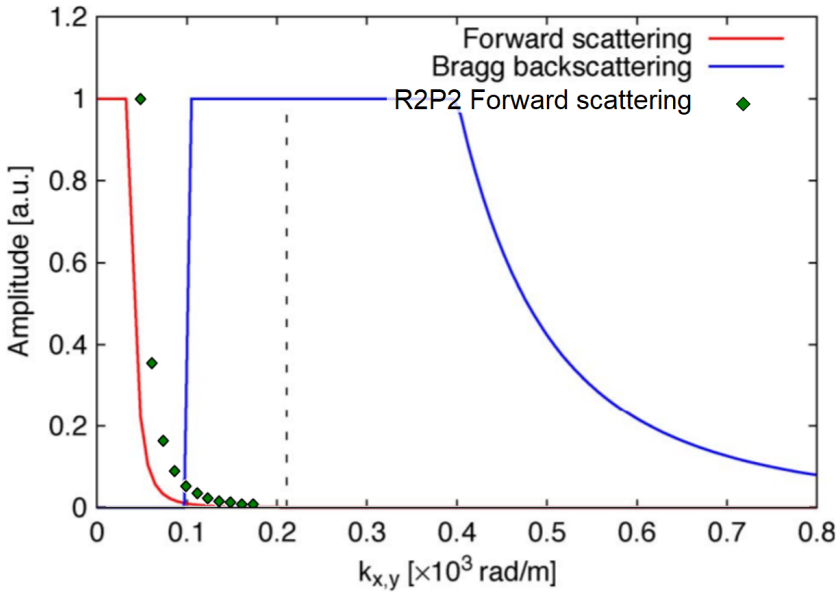

Figure 3.5: Comparison of the fluctuation range and amplitude of the forward scattering model of R2P2 with that used by F. da Silva [36]; except for an offset caused by a different $k_{\text{start,fluc}}$, the models show clear correspondence. Bragg backscattering (blue) is only present in the work of da Silva and not in R2P2.

The RMS-level, with S the area of the plasma, is given by:

$$\delta n^{\text{RMS}} = \frac{1}{S}\int_S \mathrm{d}S\ (\delta n(r,\theta))^2 \tag{3.14}$$

Simulations are done for 0.25 %, 1 %, 3 %, 5 % and 10 % turbulence.

The used homogeneous turbulence model of R2P2 does not represent all types of possible turbulence in a plasma. For example localized turbulence in a certain region or turbulence with an amplitude spectrum different than k^3-decay might occur in tokamaks. These could be added to R2P2 by modifying the model parameters and changing the resulting density function.

3.4.2 Ray Launching

3.4.2.1 Defining Radiation Diagrams

R2P2 assumes that the antenna aperture is located in the (y,z) plane with the center on the x-axis. The simulations are made in a poloidal cross-section (x,z). This means that the only relevant radiation pattern is that in the (x,z) plane with correct (O-mode) polarization, that is with $\vec{e}_E = \vec{e}_B \approx \vec{e}_y$. The radiation diagram is taken from the complete three dimensional diagram, which is often normalized so that the total radiated power in the whole diagram equals 1 W ($P = \int_\Omega S(\Omega)\mathrm{d}\Omega = 1\,\text{W}$ with Ω the solid-angle). For the two dimensional representation in R2P2, in which $S(\Omega)$ becomes $W(\theta)$, it often makes sense to re-normalize this so that the area under the 2D power density curve W is unity:

$$W_{\text{normalized}}(\theta) = \frac{W(\theta)}{\int_{-90^\circ}^{+90^\circ} W(\theta)\mathrm{d}\theta} \tag{3.15}$$

Using the normalized version, named $W(\theta)$ from here on, allows a fair comparison between different antennas. It is also possible to present the quantity in dB-scale using Equation 2.25.

Different radiation diagrams were investigated with the R2P2 code. A pyramidal horn, such as that which was used in the experiments of Valera et al [11] has the following pattern, which will be referred to as 'SINC' followed by the aperture width in mm [38]:

$$W(\theta) = \mathrm{sinc}^2\Big(\frac{D}{\lambda}\pi\sin(\theta)\Big) \tag{3.16}$$

The SINC14 radiation pattern, used in some R2P2 simulations, is given in Figure 3.6 in both carthesian and polar coordinates. Apart from this diagram, R2P2 simulations with antennas launching fundamental Gaussians and superpositions of fundamental Gaussians with higher-order TEM_{p0}-modes will be done (see Chapter 4). For these, Equations (2.16), (2.20) and (2.23) will be used.

3.4.2.2 Ray Initialization

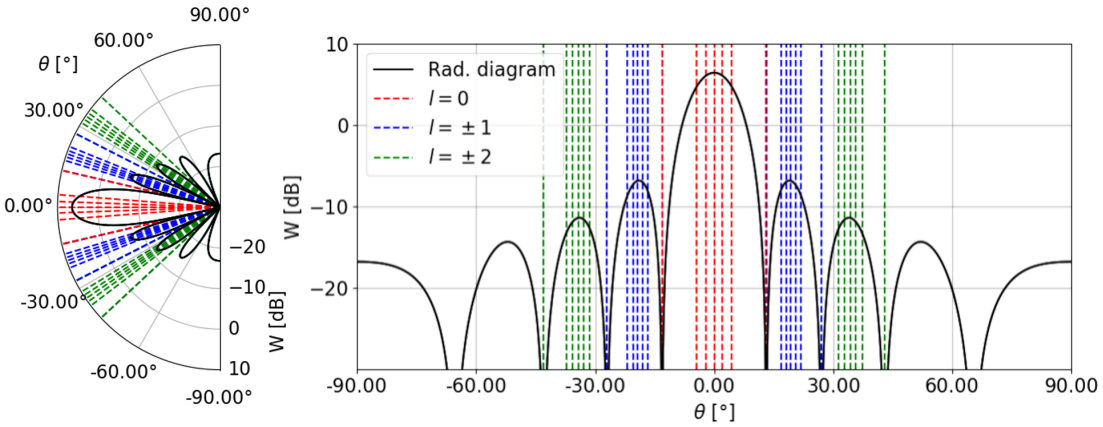

Figure 3.6: Polar and Carthesian representation of the SINC14 radiation diagram showing angular locations of launched rays when representing lobes up to secondary sidelobe by 7 rays. At the edge of the lobes, a ray for both neighbouring lobes is launched, although on the figure only one of them is always visible.

With a normalized radiation diagram in the correct direction and with correct polarization, the rays can be initialized. If a lobe is simulated by for example 7 rays, the rays will be located at angles such that the lobe is divided in 6 parts each containing equal amounts of radiated power. For the SINC14 pattern, Figure 3.6 shows the resulting locations of the rays launched in in the central lobe and the primary and secondary side lobes. The wave vector of the rays (which point in the direction of launching) is defined for each ray $\{i\}$ at θ^i by:

$$\vec{k}_0^i = k_0\big(-\cos(\theta^i)\vec{e}_x + \sin(\theta^i)\vec{e}_z\big) \tag{3.17}$$

For the actual R2P2 simulations, typically 25 rays per lobe were initially launched.

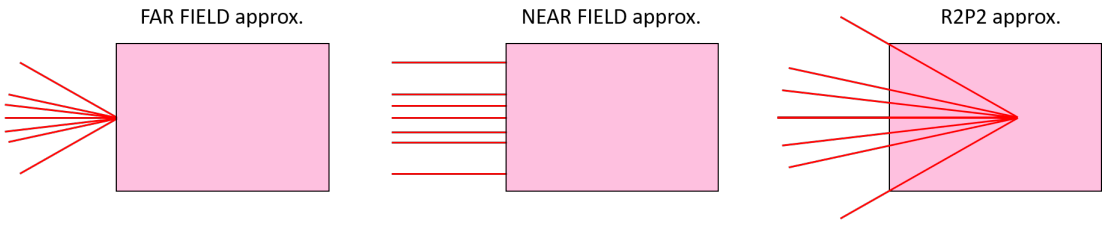

Figure 3.7: Qualitative comparison of far field, near field and R2P2 approximations for launching the rays representing a central lobe from the antenna aperture. Antenna is represented in pink with its aperture on the left side, rays are represented in red.

Ray tracing codes do not model beam divergence[1]. To account for the divergence, an approximation has to be made. If the objects with which the rays interact were located in Fraunhofer far-field, which for the frequency range 30 - 60 GHz and an antenna aperture $D \leq 20\,\text{mm}$ starts around $R_2 = 0.16\,\text{m}$ (Eq. 2.26), the rays should be launched from the aperture center $(x_0^i, z_0^i) = (a + d, 0)$. However, the blankets cause interactions at $r < R_2$. With a near-field approximation, the rays should be launched parallel from the aperture, but also this approximation would not be correct, as the blanket effects would not occur at all and the scale of the setup does require some beam divergence to be modelled. A third approach was chosen, in which the rays are launched from some distance behind the aperture, such that the whole aperture functions as a source (corresponding to the near field approximation), but the beam diverges as it would with the far field approximation. This approximation is fully justified by a comparison with full-wave simulations done in [40]. The three approximations are illustrated in Figure 3.7.

To make this 'R2P2 approximation', a focal point is chosen for each lobe (central lobe, primary sidelobes, secondary sidelobes) such that the ray at the outer edge touches the antenna aperture edge, as is shown in Figure 3.7. When for a lobe l in the radiation diagram the largest angle is θ^l_{max} (for the diagram in Figure 3.6 this is 13.10° for the central lobe, 27.02° for the primary sidelobes and 42.95° for the secondary sidelobes), the focal point for lobe l is:

$$x_0^l = a + d + \frac{D}{2\tan(\theta^l_{\text{max}})} \tag{3.18a}$$

$$z_0^l = 0 \tag{3.18b}$$

Equations 3.17, 3.18a and 3.18b define the launching parameters of a single ray completely. For ray $\{i\}$, the launching state is:

$$\Gamma_0^i = (x_0^i, z_0^i, \vec{k}_0^i, \phi_0^i = 0, t_0^i = 0) \tag{3.19}$$

with ϕ_0 the initial phase of the ray and t_0 the initial time.

[1]Beam tracing on the other hand does take into account beam divergence but needs a numerical solver for vacuum propagation [39]. Not only would this make the ray tracing code more complex, it would also make it slower and would not add that much value to the results, since other assumptions of R2P2 would remain unchanged.

Sometimes it is not correct to take $\theta^l_{\max} = 90°$ for sidelobes going up to 90°. In certain cases these sidelobes reach negligibly low values for $W(\theta)$ for angles which are a lot smaller than 90°. Instead of using $\theta^l_{\max} = 90°$, some symmetry is assumed in the tails of the sidelobe. Assuming that a sidelobe has a known start $\theta_{\text{start}} > 0$ and two known bending points $\theta_{\text{BP1}}, \theta_{\text{BP2}}$ ($\theta_{\text{BP1}} < \theta_{\text{BP2}}$), the end of the sidelobe is defined as follows:

$$\theta^l_{\max} = \theta_{\text{BP2}} + (\theta_{\text{BP1}} - \theta_{\text{start}}) \tag{3.20}$$

This definition sets the end of this type of sidelobes at a more significant location, so that the focal point location is more logically defined.

For fundamental Gaussian beams (pure TEM_{00}) a different approach is necessary to define the initial state of the rays, as the above equations applied to a pattern with only a central lobe would yield the incorrect $\theta^l_{max} = 90°$ (and Equation 3.20 only helps to resolve this issue for sidelobes, not for a central lobe). Luckily, the complete beam propagation of TEM_{00}-modes and their divergence are known (Eqs. 2.20, 2.21). This information can be used to launch the rays correctly. It is possible to launch the rays perpendicular to a far-field equiphase surface, as illustrated[2] in Figure 2.4b. By comparing the TEM_{00} field at different positions, it was found that from $x = 10w_0$ the far field asymptotic behaviour is starting to be observed[3]. It is chosen to define the launching angles of the rays perpendicular to this surface, which corresponds with using

$$x_0 = a + d + (R - 10w_0) \tag{3.21}$$

as focal point with R the radius of curvature at $10w_0$.

Instead of launching the rays from the focal point, it was decided to let them start directly at the part of the equiphase surface which is located between the blanket interspace. (x^i_0, z^i_0) is then on the equiphase surface (a circle with radius R and center in $(a + d + (R - 10w_0), 0)$), $\vec{k}^i_0$ is perpendicular to this surface, $t^i_0 \approx (10w_0)/c$ (since the distance is approximately the same for all launched rays) and $\phi^i_0 = 0$ can be kept, as the surface is equiphase and ϕ is a relative quantity which can be set 0 at any equiphase surface. This method has additional advantages when the rays are received.

3.4.2.3 Additional Ray Launching

In Section 3.2 and the flowchart Figure 3.1 it is mentioned that additional rays are launched in case the spatial (angular) resolution of the simulation is insufficient in a certain region. An additional ray is launched in the middle between two rays:

[2]In this figure, the location where 'Beam Radius' is marked is approximately where the far field starts, this is characterized by the beam radius starting to behave linearly instead of quadratically and the equiphase surfaces to be expanding circles.

[3]With hindsight it would be more logical to use a multiple of the confocal distance (Eq. 2.22) instead of beam waist for this parameter. In future versions of R2P2 this could be modified.

1. When two neighbouring rays are both not received and the power contained between them is bigger than 1 % of the total amount; to make sure that the whole fraction is really not received.
2. When only one of two neighbouring rays is received and the power contained between them is bigger than 0.01 %; to obtain a very high resolution in the region between collected and not collected rays.
3. When two neighbouring rays are both received but their time of flight varies with more than 1 % and/or their phase when returning varies with more than 1 %; to make sure that effects causing significant time or phase delays (such as extra reflections or turbulence effects) are mapped with high resolution.

Additional rays are launched according to the same procedure as for the initially launched rays.

3.4.3 Vacuum Ray Tracing

3.4.3.1 Vacuum Propagation

A ray i at propagation step p is represented by state

$$\Gamma_p^i = (x_p^i, z_p^i, \vec{k}_p^i, \phi_p^i, t_p^i) = (x_p, z_p, \vec{k}_p, \phi_p, t_p)^i \tag{3.22}$$

It propagates in a straight line in the direction of $\vec{k}^i$ until it encounters an object (first encountered object = FEO) on its path. Suppose that the object is located at $(x_{\text{FEO}}, z_{\text{FEO}})$. The travelled distance and time up to the object are:

$$\Delta r = \sqrt{(x_p - x_{\text{FEO}})^2 + (z_p - z_{\text{FEO}})^2} \tag{3.23a}$$

$$\Delta t = \Delta r / c \tag{3.23b}$$

The resulting next state Γ_{p+1}^i is:

$$\Gamma_{p+1}^i = (x_{\text{FEO}}, z_{\text{FEO}}, \vec{k}_p, \phi_p + \omega \cdot \Delta t, t_p + \Delta t)^i \tag{3.24}$$

The observed phase difference corresponds with classical vacuum propagation.

3.4.3.2 Blanket Reflections

Blankets are modelled as perfect mirrors. Therefore a ray encountering a blanket with surface normal $\vec{e}_{\text{FEO}}$ as FEO undergoes a specular reflection. When the last registered state is

$$\Gamma_p^i = (x_{\text{FEO}}, z_{\text{FEO}}, \vec{k}_p, \phi_p, t_p)^i \tag{3.25}$$

the reflection causes a 180° phase shift and changes the direction of the wave vector, such that the state after reflection is:

$$\Gamma_{p+1}^i = (x_{\text{FEO}}, z_{\text{FEO}}, |\vec{k}_p|\big(2(\vec{e}_{\text{FEO}} \cdot \vec{e}_{kp})\vec{e}_{\text{FEO}} - \vec{e}_{kp}\big), \phi_p + \pi, t_p)^i \tag{3.26}$$

3.4.4 Plasma Ray Tracing

3.4.4.1 Ray Tracing Formulas

Because a tokamak plasma has a continuously varying refractive index for O-mode waves, rays travelling through it are bent. The equations describing the behaviour of the rays, based on a WKB approximation [33], are well-known and commonly used in studies of waves in plasmas for fusion research as well as radio communication (where rays going through the ionosphere are studied).

The O-mode dispersion relationship (Eq. 2.11) is rewritten as a homogeneous equation with $\vec{r} = x\vec{e}_x + z\vec{e}_z$ and $\vec{k} = k_x\vec{e}_x + k_z\vec{e}_z$:

$$\mathcal{M}(\omega, \vec{k}, \vec{r}, t) = \omega^2 - |\vec{k}|^2 c^2 - \omega_p(\vec{r}, t)^2 = 0 \tag{3.27}$$

The plasma is stationary, since the time of flight of a ray through the plasma is much smaller than the smallest timescale for plasma density fluctuations. Therefore the time-dependency of $\mathcal{M}$ disappears:

$$\mathcal{M}(\omega, \vec{k}, \vec{r}, t) = \mathcal{M}(\omega, \vec{k}, \vec{r}) \tag{3.28}$$

$$\frac{\partial \mathcal{M}}{\partial t} = 0 \tag{3.29}$$

The ray tracing equations in the plasma are given by[4] [33, Chapter 3]:

$$\frac{\mathrm{d}\vec{r}}{\mathrm{d}t} = -\frac{\partial \mathcal{M}/\partial \vec{k}}{\partial \mathcal{M}/\partial \omega} = \frac{\vec{k}c^2}{\omega} \tag{3.30}$$

$$\frac{\mathrm{d}\vec{k}}{\mathrm{d}t} = \frac{\partial \mathcal{M}/\partial \vec{r}}{\partial \mathcal{M}/\partial \omega} = -\frac{\nabla \omega_p^2}{2\omega} \tag{3.31}$$

$$\frac{\mathrm{d}\omega}{\mathrm{d}t} = -\frac{\partial \mathcal{M}/\partial t}{\partial \mathcal{M}/\partial \omega} = 0 \tag{3.32}$$

A first observation is that when travelling through a stationary plasma the frequency of a wave does not change. The frequency of the probing ray and state Γ_p^i when entering the plasma are known. However, to use the ray tracing equations, also $\omega_{pe}(x, z)$ (Eq. 2.6), as well as its spatial gradients need to be known. These quantities depend on the local plasma density.

3.4.4.2 Analytical Solver

A first possibility in R2P2 it to use the pure quadratic density profile (Eq. 2.2) with an analytical plasma ray tracing solver. Solving Equations 3.30 and 3.31 with this density profile yields the following equations:

$$x_{p+s} = ac/\omega_{p0} \cdot (C_1 e^{\omega_{p0}/\omega \cdot ct_{p+s}/a} - C_2 e^{-\omega_{p0}/\omega \cdot ct_{p+s}/a}) \tag{3.33a}$$

$$z_{p+s} = ac/\omega_{p0} \cdot (C_3 e^{\omega_{p0}/\omega ct_{p+s}/a} - C_4 e^{-\omega_{p0}/\omega \cdot ct_{p+s}/a}) \tag{3.33b}$$

$$k_{x,p+s} = C_1 e^{\omega_{p0}/\omega \cdot ct_{p+s}/a} + C_2 e^{-\omega_{p0}/\omega \cdot ct_{p+s}/a} \tag{3.33c}$$

$$k_{z,p+s} = C_3 e^{\omega_{p0}/\omega \cdot ct_{p+s}/a} + C_4 e^{-\omega_{p0}/\omega \cdot ct_{p+s}/a} \tag{3.33d}$$

[4] $\vec{a} = \partial B/\partial \vec{c}$ corresponds with $\forall i : \vec{a}_i = \partial B/\partial \vec{c}_i$

With these, the ray state Γ^i_{p+s} can be determined, when t_{p+s} is known. Also the time when the ray exits the plasma t_{exit} is analytically known:

$$t_{\text{exit}} = \log\left[\sqrt{2}\Big(\Big((-4C_1^2C_4^2 + 8C_1C_2C_3C_4 - 4C_2^2C_3^2 + 4C_1C_2C_5 + 4C_3C_4C_5 + C_5^2)^{1/2} + 2C_1C_2 + 2C_3C_4 + C_5\Big)\cdot\Big(C_1^2 + C_3^2\Big)\Big)^{1/2}\Big/\Big(2\Big(C_1^2 + C_3^2\Big)\Big)\right]\Big/C_6 \tag{3.34}$$

In principle it suffices to set $t_{p+1} = t_{\text{exit}}$, however this would not bring much knowledge about the behaviour of the ray inside the plasma. A more interesting approach would be to set $t_{p+s} = t_p + s(t_{\text{exit}} - t_p)/s_{\text{exit}}$ in which s_{exit} equals the number of steps the ray takes in the plasma. By defining e.g. $s_{\text{exit}} = 50$, 50 analytical steps are made, so that the trajectory made by the rays inside the plasma is visible, similar to how it is in Figure 2.7. With $s_{\text{exit}} = 1$ the trajectory in the plasma would not be visible.

The constants introduced in Equations 3.33 are:

$$\omega_{p0} = \sqrt{\frac{n_0 e^2}{\epsilon_0 m_e}} \tag{3.35a}$$

$$\alpha = |k_{z,p}|\tan^{-1}\left(\left|\frac{k_{z,p}}{k_{x,p}}\right|\right) \tag{3.35b}$$

$$C_1 = (-a\omega\cos(\alpha) + \sqrt{a^2 - z_p^2}\omega_{p0})/(2ac) \tag{3.35c}$$

$$C_2 = -(a\omega\cos(\alpha) + \sqrt{a^2 - z_p^2}\omega_{p0})/(2ac) \tag{3.35d}$$

$$C_3 = (\omega\sin(\alpha)a + z_p\omega_{p0})/(2ac) \tag{3.35e}$$

$$C_4 = (\omega\sin(\alpha)a - z_p\omega_{p0})/(2ac) \tag{3.35f}$$

$$C_5 = \omega_{p0}^2/c^2 \tag{3.35g}$$

$$C_6 = \omega_{p0}/\omega \cdot c/a \tag{3.35h}$$

(3.35i)

The analytical solver is interesting to get a first, very fast, indication of a new problem setup. This could be to test a new function of the code or to get a first impression of a different antenna diagram. It is also possible to build similar analytical solvers using a different analytical density model and solving the ray tracing equations accordingly. However to model a realistic plasma it is necessary to implement a numerical solver.

3.4.4.3 Numerical Solver

With a known turbulence model (Section 3.4.1) resulting in the plasma density, it is straightforward to make the numerical solver. In R2P2 the differential equations Eqs. 3.30 and 3.31 are solved with the density model given in Eq. 3.4,

using an adaptive step-size[5] Runge-Kutta (RK) method of order 45. To use this method, the total density profile from Equation 3.12 is not calculated at a fixed grid and then interpolated, but the density and the necessary spacial derivatives (calculated as finite differences over 100 μm) are always calculated at the exact location where the ray passes. This gives a more precise result than an interpolation on a fixed grid, but is computationally more intensive. Because of the limited number of rays and fluctuation wavenumbers k_{fluc} used, the calculation still is fast enough and its advantages outweigh the added calculation time.

3.4.5 Ray Termination and Received Power Reconstruction

Except for the plasma and the metallic walls, the rays can encounter two objects: the domain edge and the collection aperture. In case the ray hits the domain edge, the computation terminates. In case the ray hits the collection aperture, the computation ends after the ray gets stored as received. For any pattern apart from the fundamental Gaussian, the collection aperture is the (receiver) antenna aperture, located at $x = a + d$ and $z \in [-D/2, D/2]$. For a fundamental Gaussian the collection aperture is identical to the launching phase front as defined in Section 3.4.2.2. Just like for the launching of the TEM_{00}, an additional phase shift and time interval are added to the collected results to account for the vacuum propagation that would exist in reality when the rays would be collected at the actual aperture. The reason for collecting at the launching aperture is the reciprocity of the antenna: assuming a monostatic system in which the receiving and emitting antenna are identical, their emitting and receiving properties are identical as well, so if rays are launched from this surface, they should be collected there.

After all rays (including those added to increase spatial resolution) are terminated in the main R2P2 program (Fig. 3.1), information is available on whether or not a ray returns to the receiver and if yes, at what time this happens. In Chapter 4, statistical post-processing methods will be described in which the results of the simulations are interpreted as statistical ensemble, however there is also some post-processing which can be done for individual simulations. A reconstruction of the received power $P(t)$ can be made based on the received rays. In a first approximation, the rays can be considered to 'carry' the power. Ray i would then carry power $P^i = \frac{1}{2}P_{\theta_{i-1}\to\theta_i} + \frac{1}{2}P_{\theta_i\to\theta_{i+1}}$ (with $P_{\theta_{i-1}\to\theta_i}$ the power located between θ_{i-1} and θ_i in the radiation diagram[6]). When ray i would be received at time t_q^i, the whole power P^i would arrive at the receiver on that time, or: $P(t) = \sum_i P^i \delta(t_q^i - t)$ (with i only the collected rays and $\delta(t) = 1$ for $t = 0$ and $\delta(t) = 0$ elsewhere).

[5] Adaptive step-size RK45 methods make 2 estimates for each step, one using an RK4, the other using an RK5 method (ideally with a lot of overlapping calculations between the used methods). For step n, time step τ_n is used and the difference of the results of both methods is named ϵ_n. An error tolerance level ϵ_{max} is set. When $\epsilon_n < \epsilon_{max}$, the solution is accepted and a slightly higher $\tau_{n+1} > \tau_n$ is tried for the next step, limiting the number of calculations. If however $\epsilon_n > \epsilon_{max}$, the same step is repeated with a smaller step size ($\epsilon'_n < \epsilon_n$).

[6] Recall that $\forall i : \theta_{i-1} < \theta_i < \theta_{i+1}$.

The assumption that the power is carried on the rays is however wrong. With this approach the wave nature of the radiation is forgotten. The power is not located on the rays but in between them, making it wrong to say that when two neighbouring rays return, it results in two peaks in $P(t)$ at t_q^i and t_q^{i+1} (note that in general $q^i \neq q^{i+1}$). In reality, $P(t) > 0\ \forall t \in [t_q^i,\ t_q^{i+1}]$, as the power between the rays will return during this interval and not only when one of the rays returns. One possibility would be to launch an extremely high number of rays, so that in a limiting case the first approximation becomes correct. This would however increase the calculation time a lot. A second approach uses phase front reconstructions and takes into account rays $i-1$ and $i+1$ for each collected ray i, so that the power can be considered between the rays. By defining multiple phase fronts around the collection times of the rays, a good approximation of $P(t)$ can be made while simulating only few rays. The step-by-step procedure as well as graphical representations of this method can be found in Appendix A. The reconstruction of the phase fronts involves a lot of interpolations, all of these calculations are however very fast, so that there is a considerable speed increase compared to the alternative of launching a lot more rays.

3.5 R2P2 Pseudocode and Performance

The main R2P2 code executes the above described program as given in Algorithm 1, which returns for each ray i its end-state Γ_q^i as well as pass^i, the number of passes through the plasma; refl^i, the number of blanket reflections and col^i, whether or not the ray is collected. This code is run 400 times for the same plasma parameters associated to different turbulence matrices to make statistical interpretation of the results possible. To speed up the process the asynchronous pool function of Pythons *multiprocessing* library is used, this allows the 400 processes to be run optimally in parallel on the available CPU. The results of the 400 runs are stored using the *pickle* library, making them accessible for the phase-front reconstruction program (Appendix A) and further post-processing explained in Chapter 4. To optimize the individual runs, the computationally most intensive parts of R2P2 were tested with the *%timeit* iPython magic command with typical inputs, this command returns the average computation time of a code part which can be used to optimize the used functions and loops. With this, it was seen that it is often preferable to make creative use of available commands from the *numpy* and *scipy* libraries instead of defining own functions, because the standard library commands run very performant code behind the screens. The *jit* library was used to speed up nested loop structures. As a result of these optimizations, R2P2 completes 400 simulations at highest turbulence level in about 70 core hours on an Intel Xeon E5 system. Different datatypes (list, array, dict, tuple) are used for different variables throughout the code, these variables were chosen for their functionality, but possibly changes in the used datatypes could speed up the code even more.

Algorithm 1: R2P2 ray tracing code

input : geometry: a, d, h, D
density: n_0, $k_{fluc}(i,j)$, $A(i,j)$
radiation pattern: ω, $W(\theta)$, number of lobes to trace l_{max}, number of rays per lobe i_{max}
output: For each ray i: end-state Γ_q^i, pass^i, refl^i, col^i.
$\phi(i,j)$ for reproducibility

Define random $\phi(i,j) \in [0,\pi]$;
for *lobe* $l \in [-|l_{max}|, l_{max}]$ **do**
  Set (x_0, z_0) *(Equation 3.18a, 3.18b, 3.21)*;
  For $i_{\max}$ rays determine the ray angle in lobe range $[\theta^l_{start}, \theta^l_{end}]$ such that $\forall i,j < i_{\max} : \int_{\theta_i}^{\theta_{i+1}} W(\theta)\mathrm{d}\theta = \int_{\theta_j}^{\theta_{j+1}} W(\theta)\mathrm{d}\theta$;
  while $i \leq i_{max}$ **do**
    $p = 0$;
    pass = 0; refl = 0; col = 0;
    termination = 0;
    $\Gamma_p = (x_0, z_0, \vec{k}_0^i, \phi_0 = 0, t_0 = 0)$ *(Equation 3.19)*;
    while *termination = 0* **do**
      List all objects on ray propagation path;
      Define first encountered object (=FEO);
      $\Delta t = \sqrt{(x_p - x_{FEO})^2 + (z_p - z_{FEO})^2}/c$;
      $\Gamma_{p+1} = (x_{FEO}, z_{FEO}, \vec{k}_p, \phi_p + \omega \cdot \Delta t, t_p + \Delta t)$ *(Equation 3.24)*;
      $p = p + 1$;
      if *FEO = plasma* **then**
        Solve m next states in plasma: $\Gamma_{p+m} =$ **PlasmaSolver**$(\omega, \Gamma_p, a, n_0, k_{fluc}(i,j), A(i,j), \phi(i,j))$ *(Section 3.4.4)*;
        pass = pass + 1;
      else if *FEO = blanket* **then**
        $\Gamma_{p+1} = (x_p, z_p, |\vec{k}_p|\big(2(\vec{e}_{FEO} \cdot \vec{e}_{kp})\vec{e}_{FEO} - \vec{e}_{kp}\big), \phi_p + \pi, t_p)$ *(Equation 3.26)*;
        refl = refl + 1;
      else if *FEO = aperture* **then**
        col = 1;
        termination = 1;
      else if *FEO = domain edge* **then**
        termination = 1;
    end
    if $i = i_{max}$ **then**
      Check spatial resolution;
      Add rays: define θ_i for new rays and update $i_{\max}$*(Section 3.4.2.3)*;
    end
  end
end

Chapter 4

R2P2 Simulation Results and Analysis

4.1 Simulated Radiation Patterns

Frequency-independent antennas could make the use of plasma reconstruction methods based on simulation databases or neural networks in blanket-equipped tokamaks possible. However, it is not sure that when using such antennas, the performance of the system remains good; it is possible that changing the antennas will result in less power return to the receiver, or that more perturbations caused by the blankets will show in the returning signals. To quantify these effects, eleven radiation patterns with different characteristics were simulated with the R2P2 code. For a single antenna, simulations are made at five equidistant frequencies (30 GHz, 37.5 GHz, 45 GHz, 52.5 GHz, 60 GHz) and for six amounts of turbulence (0 %, 0.25 %, 1 %, 3 %, 5 %, 10 %). For each combination of these parameters, 400 simulations with different turbulence phase matrices are run. The radiation diagrams are normalized using Equation 3.15. The used environment is ITER-like ($a = 2\,\mathrm{m}$, $n_0 = 10^{20}\,\mathrm{m}^{-3}$, $d = 200\,\mathrm{mm}$, $h = 15\,\mathrm{mm}$, see Fig. 3.3).

The first simulated antenna diagram is that of the antenna which ought to be used by ITER: a flared rectangular horn antenna with an aperture size of 14 mm in poloidal and 24 mm in toroidal direction [29]. The associated radiation diagram was introduced as SINC14 in Equation 3.16 and Figure 3.6. For this antenna, simulations were done with two different distances between antenna and plasma edge: not only $d = 200\,\mathrm{mm}$, but also $d = 250\,\mathrm{mm}$ was simulated. Since the results of the simulations at $d = 250\,\mathrm{mm}$ did not provide any additional information, only $d = 200\,\mathrm{mm}$ was simulated for the other antennas.

Apart from this diagram, five fundamental Gaussian diagrams (Section 2.2.2.3) are simulated. Antennas with this type of radiation pattern are often used for generating focused beams. By changing the relation between the beam waist w_0 and the wavelength λ, it is possible to change the shape of the radiation pattern such that it is e.g. independent of the frequency, which forms be a good starting point for the antenna optimization that is to be done. From Equations 2.20 and 2.21 it can be derived that an antenna launching TEM_{00} modes with beam waist

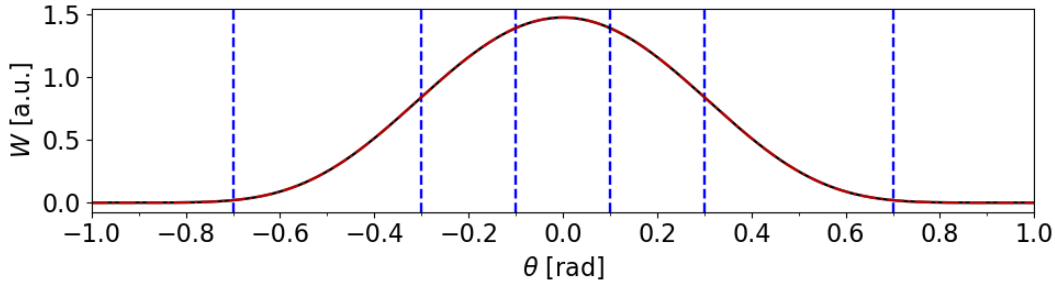

(a) TEM_{00}: $w_0 = 0.588\lambda$, $D = 14\,\text{mm}$

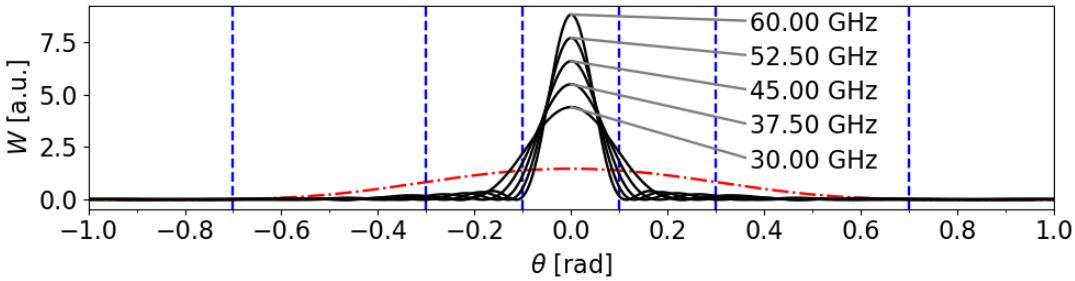

(b) SINC14 (Eq. 3.16)

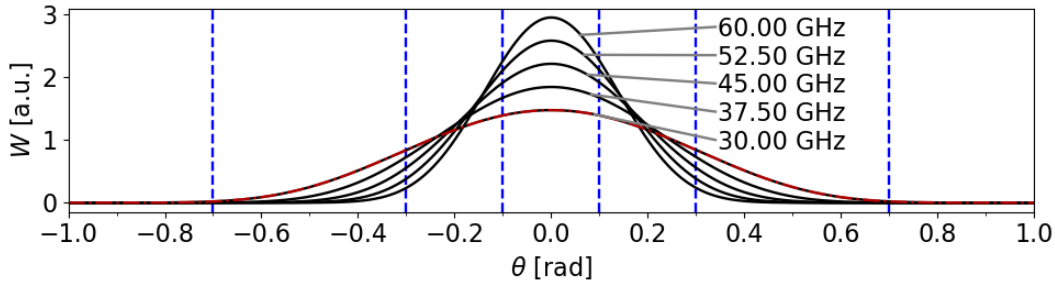

(c) TEM_{00}: $w_0 = 5.88\,\text{mm}$, $D = 14\,\text{mm}$ (fixed beam waist)

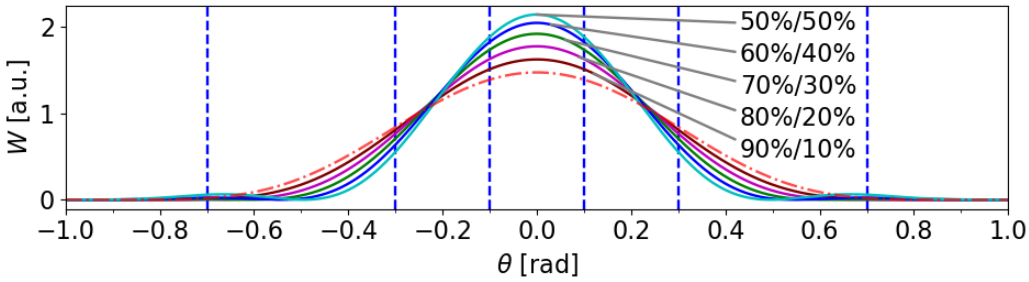

(d) TEM_{00}/TEM_{10} mix with 180° relative phase shift; $w_0 = 0.588\lambda$, $D = 14\,\text{mm}$

Figure 4.1: Radiation diagrams of the simulated antennas. When frequencies are not indicated, the radiation pattern is frequency independent. In all diagrams the fundamental Gaussian pattern with $w_0 = 0.588\lambda$ and $D = 14\,\text{mm}$ (Fig. 4.1a) is drawn as red dotted line for comparison. Vertical lines are drawn at $\pm 0.1\,\text{rad}$, $\pm 0.3\,\text{rad}$ and $\pm 0.7\,\text{rad}$.

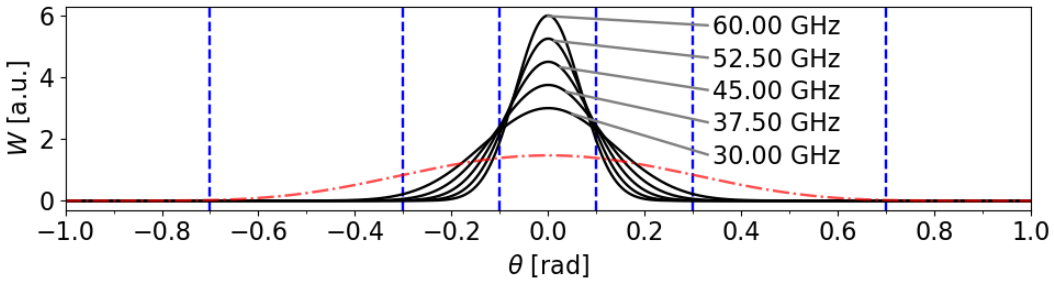

(a) TEM_{00}: $w_0 = 12\,\text{mm}$, $D = 28\,\text{mm}$ (fixed beam waist)

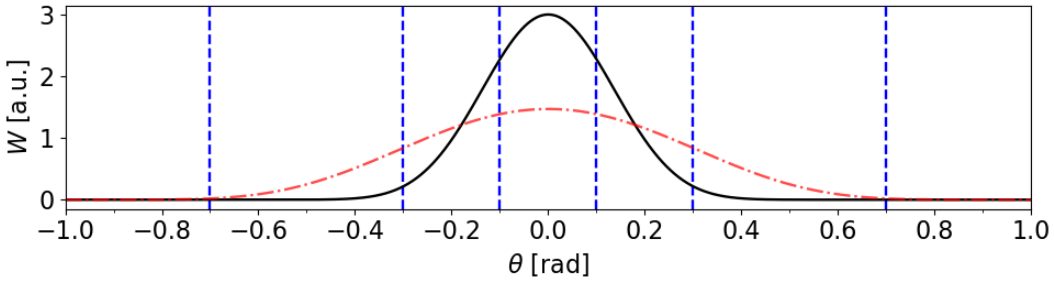

(b) TEM_{00}: $w_0 = 1.2\lambda$, $D = 28\,\text{mm}$

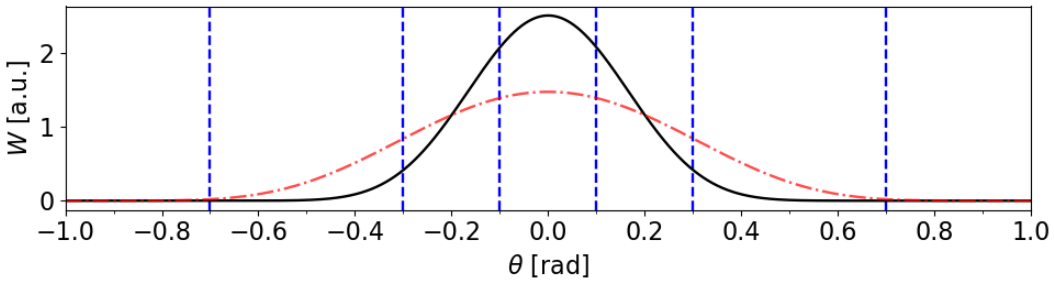

(c) TEM_{00}: $w_0 = \lambda$, $D = 24\,\text{mm}$

Figure 4.2: Radiation diagrams of the simulated antennas. When frequencies are not indicated, the radiation pattern is frequency independent. In all diagrams the fundamental Gaussian pattern with $w_0 = 0.588\lambda$ and $D = 14\,\text{mm}$ (Fig. 4.1a) is drawn as red dotted line for comparison. Vertical lines are drawn at $\pm 0.1\,\text{rad}$, $\pm 0.3\,\text{rad}$ and $\pm 0.7\,\text{rad}$.

$$w_0 \propto \lambda \tag{4.1}$$

results in an antenna with a radiation pattern that is independent of the used frequency. The proportionality factor is limited by the antenna aperture size. For a cylindrical horn antenna with beam waist at the aperture, it is not possible to launch a TEM_{00} with $w_0 > D/2$. With some margin, often $w_0 = D/3$ is used and $w_{0,max} \approx 0.42D$ is said to be an upper boundary [41]. With respect to this maximum beam waist, a frequency-independent diagram can be obtained when using

$$w_0(\lambda) = w_{0,max} \cdot \frac{\lambda}{\lambda_L} \tag{4.2}$$

with $f_L = c/\lambda_L$ the lowest frequency of the range in which the antenna works. A disadvantage of such an antenna is that for all frequencies different from f_L the beam is wider than it would be when the relation used was

$$w_0(\lambda) = w_{0,max} \tag{4.3}$$

To observe the effects of the chosen $w_0(\lambda)$, antennas with different beam waist-wavelength relations (either Eq. 4.2 or Eq. 4.3) will be simulated.

In ITER conditions, the allowed antenna size is limited. The antenna should fit between the blankets, meaning that its maximum size (with $h = 15\,\text{mm}$, Fig. 3.3) is $D = 40\,\text{mm}$, corresponding to $w_{0,max} = 0.42D = 16.8\,\text{mm}$. In this case, the antenna would touch the blankets and the outer 5 mm rim of the antenna would face a reflective component directly in front of it. A better maximum size would be $D = 2h = 30\,\text{mm}$: the antenna does no longer touch the blanket structures and does not have any metallic objects in front of the aperture. This corresponds to $w_{0,max} = 12.6\,\text{mm}$. A third approach could be to start from the same size as the reference antenna with SINC14 pattern used in [11], which has a poloidal size $D = 14\,\text{mm}$, associated with $w_{0,max} = 5.88\,\text{mm}$.

With R2P2, several possibilities were simulated. Two antennas with a $D = 14\,\text{mm}$ aperture were simulated, one with $w_0(\lambda) = w_{0,max} \cdot \lambda/\lambda_L = 0.588\lambda$, another with $w_0(\lambda) = 5.88\,\text{mm}$. Additionally, two larger antennas with $D = 28\,\text{mm}$ were simulated, again one with a frequency-independent radiation pattern ($w_0(\lambda) = 1.2\lambda$) and another with maximum beam waist for all frequencies ($w_0(\lambda) = 12\,\text{mm}$). Finally an antenna with $D = 24\,\text{mm}$ and $w_0(\lambda) = \lambda$ was simulated.

Apart from the fundamental Gaussian patterns, some antennas launching a combination of TEM_{00} and TEM_{10} were investigated. These superpositions have a larger divergence than fundamental Gaussians, but can have narrower central beams close to the antenna when using the same beam waist constraints as for the fundamental Gaussians. Power fractions from 0 % up to 50 % TEM_{10} with 180° initial phase shift relative to TEM_{00} were simulated in steps of 10 %. For these antennas $D = 14\,\text{mm}$ and $w_0(\lambda) = 0.588\lambda$ were used. On Figures 4.1 and 4.2 all simulated patterns are given. The R2P2 simulations results give measurements of PPR performance so that possible changes as a consequence of the large variations in width of the main beam and the differences between frequency-independent and frequency-dependent patterns can be quantified.

4.2 R2P2 Result Analysis

In some parts of the following section, the results of a single antenna at a single frequency will be used to draw conclusions on all antennas at all simulated frequencies. This is only done when the results were clearly similar for all antennas. In parts where there are more relevant differences between the different antennas or frequencies, this is mentioned and analyzed accordingly.

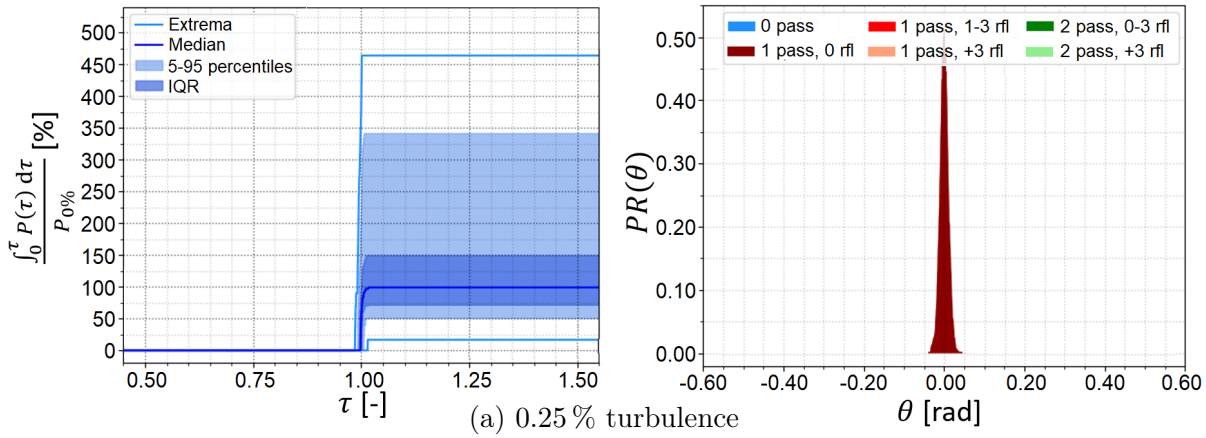

(a) 0.25 % turbulence

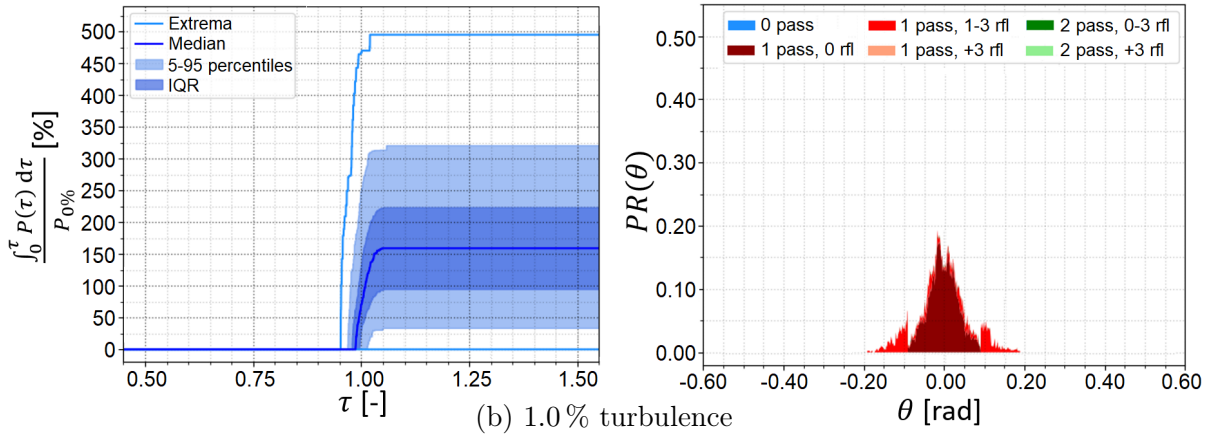

(b) 1.0 % turbulence

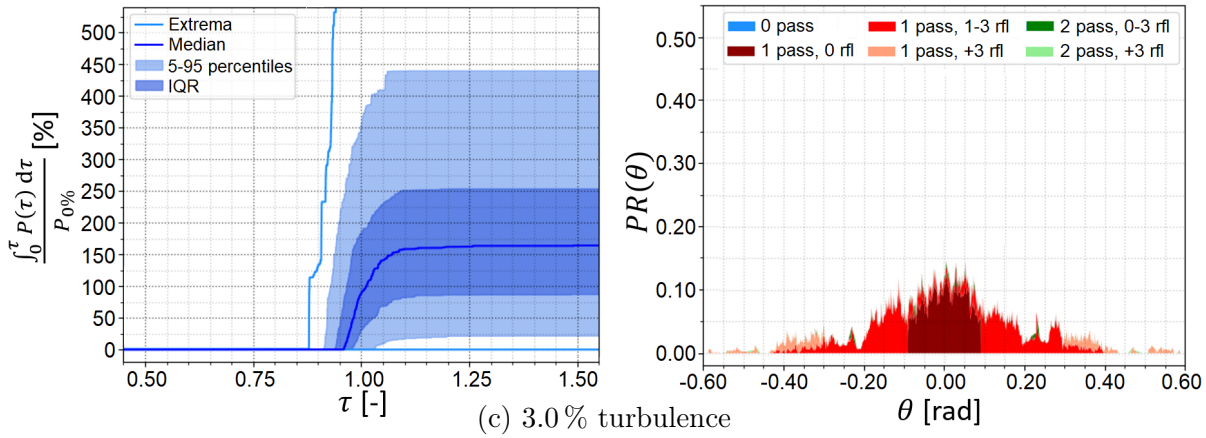

(c) 3.0 % turbulence

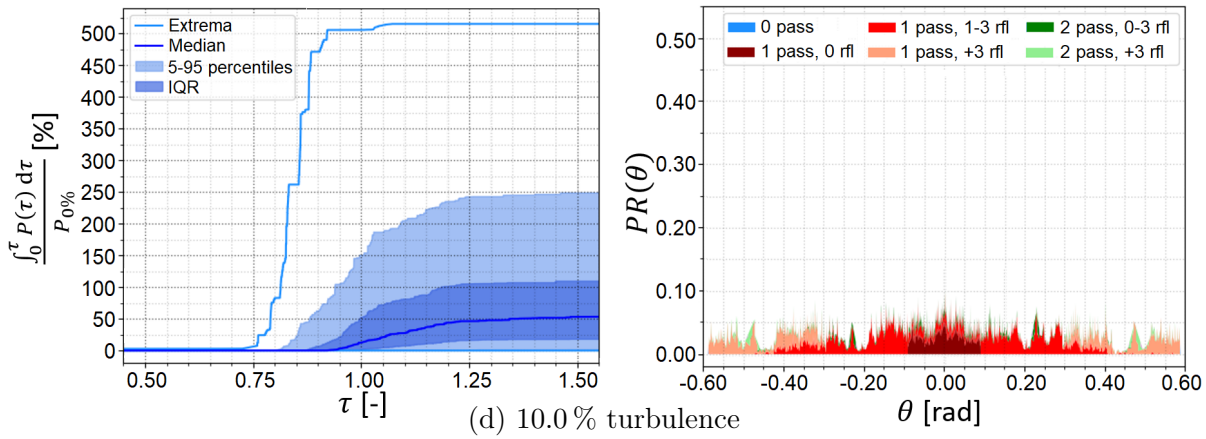

(d) 10.0 % turbulence

Figure 4.3: R2P2 results for SINC14 pattern at 30 GHz and $d = 200$ mm. (left column) normalized received power against time; (right column) Probability for a ray to be received as a function of its launch angle θ.

4.2.1 Power Return

For a set of 400 simulations with different turbulence phase matrices, the power returning to the receiver antenna can be represented in multiple ways: the phase front reconstruction explained in Appendix A results in graphs such as on the left of Figure 4.3, where for the SINC14 antenna at 30 GHz it is shown how much power returns to the receiver as a function of time. The figures depict the returned power (normalized on the 0 % turbulence case, which corresponds to 0.0414 W for SINC14 at 30 GHz) against time (normalized on the non-turbulent time of flight $t_{0\%} = 2.8833\,\text{ns}$). The normalized time is named τ:

$$\tau = \frac{t}{t_{0\%}} \tag{4.4}$$

On the figures, the median of the 400 simulations, the interquartile range (IQR), an expanded version of the IQR going from 5 % to 95 % and the extrema are plotted. No figures are given for the non-turbulent case, as it would only show a step-function at $\tau = 1$ going from 0 % to 100 % on the vertical axis. It is chosen to use median and IQR to interpret the simulation results, because the distribution of the amount of received power is at each time asymmetric. This is clearly visible in the location of the extrema, where independent of τ and the location of the median, the minimum is always close to 0 %, but the maximum reaches very high values. In the lowest turbulence case, the median behaviour of the simulations is almost identical to the non-turbulent behaviour. However, the IQR shows a broad distribution. With higher turbulence, the shape of the median curves is no longer step-, but rather S-shaped. The slope of the S-curve gets flatter as the turbulence becomes higher, and for 10 % turbulence, even at $\tau = 1.55$, the median received power is still slightly increasing.

The median received power at $\tau = 1.55$ increases first as turbulence gets higher (to 0.0684 W for 3 % turbulence, well above 0.0414 W, the amount of received power in the non-turbulent case) and then decreases again for very high turbulence levels. This phenomenon will be discussed in more detail in Section 4.2.2.

4.2.2 Probability on Return

On the right side of Figure 4.3, the probabilities for a ray to return to the receiver $\text{PR}(\theta)$ are given, and the colors represent the trajectory followed by the ray before being received. First the total returned power (accumulation of the different colours) will be discussed, in Section 4.2.3 the meaning of the colours will be clarified and discussed. At 0.25 % turbulence, only rays with $|\theta| < 0.05\,\text{rad}$ have any possibility of being received with the central rays having a probability slightly higher than 50 % to return. As turbulence rises, the chance that a ray undergoes large deflections while travelling through the plasma increases. A first consequence is that the θ-interval with a chance on returning to the antenna broadens, because rays which would not return in a non-turbulent plasma can

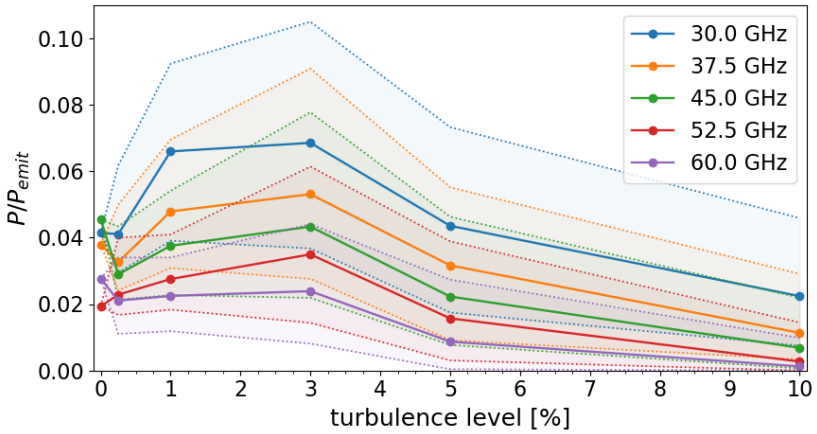

Figure 4.4: Median returned power and IQR at $\tau = 1.55$ for SINC14 radiation pattern for various frequencies and amounts of turbulence. It can be seen that the total received power reaches a maximum at $\approx 3\,\%$ turbulence.

now get deflected towards the antenna. A second consequence is that PR(θ) lowers when θ already had a chance of returning to the antenna, because of an increased chance on deflections away from the antenna. Both effects can be clearly seen in the figures. The expansion of the theta-interval is seen in Fig. 4.3b-c opposed to Fig. 4.3a. The overall lowering of PR(θ) is seen the clearest in Fig. 4.3c-d. These effects have influence on the returning power. Figure 4.4 gives the median returned power at $\tau = 1.55$, an indication of how much power is received in total. For all frequencies, a peak in in returning power fraction is seen at 3 %. This corresponds with the described effects: up to 3 % turbulence the 'broadening' effect dominates, resulting in an increase in the returning power. For turbulence higher than 3 % the 'lowering' effect dominates, so that the received power goes down again. These phenomena are also described by [36, 42]. In [36], a finite-difference time-domain full-wave code found a maximum amplitude of the return signal was also around 3 % turbulence, agreeing with the results that are presented here.

In Figure 4.4, the results of the higher frequencies of the SINC14 pattern are very similar those of the 30 GHz simulations. The main difference is that higher frequencies are reflected deeper in the plasma, so with the used homogeneous turbulence model, the turbulent zone through which the rays travel is larger. This makes the discussed effects associated with turbulence (mainly changing S-shape of returned power and lower return probability levels) stronger when the frequency is higher, so that the median returning power is lower.

4.2.3 Probability on Return for Different Ray Trajectories

In Figure 4.3, the colours in the figures at the right represent the type of trajectory the ray has run through before reaching the receiver. Dark red zones are the probability for a ray to return to the receiver after an unperturbed trajectory with a single passage through the plasma and no reflections on the blanket walls. Bright red zones and pale red zones also have a single passage through the plasma

but with 1 to 3, respectively more than three parasitic reflections on the blankets (Figure 2.7b shows an example of such trajectories). Dark and light green regions represent rays that return after two passages through the plasma (illustrated in Figure 2.7c). These green zones are only visible in small areas of few graphs. Blue zones, representing rays that return without passing through the plasma cannot be seen in these figures, but do exist in some cases outside of the plotted θ-interval and will be discussed further on. In the 0.25 % turbulent case, the only rays with probability on return are those with unperturbed trajectories. Starting from 1 % turbulence also the probabilities of different types of trajectories rises. This goes together with the flattening of the S-shaped curves in the amplitude collection graphs on the left of Figure 4.3. It are however not only the perturbed trajectories that influence the shape of the received power: the time for a ray to travel through a turbulent plasma zone is on average larger than when travelling through non-turbulent plasma, because the turbulence bends the ray in a lot of turns, inhibiting a straight trajectory. It is mainly this effect that causes the changing S-shape of the received power curve.

The unperturbed trajectory probabilities (dark red) in Figure 4.3 are for each amount of turbulence and frequency limited to $|\theta| < 0.1\,\text{rad}$. At 3 % turbulence, a steep decrease in possibility on return is seen around $|\theta| \approx 0.2\,\text{rad}$. In order to see if these effects also occur at different frequencies and for other antennas, the probabilities for a ray to return in different cases of turbulence and at different frequency were averaged out for each antenna separately. With the probability on return named $\text{PR}(\theta)$, the formula used is:

$$\overline{PR}_{\text{antenna}}(\theta) = \frac{1}{25} \sum_{f} \sum_{\text{turb}} \text{PR}(\theta) \tag{4.5}$$

with f representing all simulated frequencies and turb representing all simulated turbulence levels. Some results are presented in Figure 4.5, for the other antennas the resulting figures are found in Figure B1 in Appendix B.

It is seen that the return probabilities of the unperturbed trajectories are zero for $|\theta| > 0.1\,\text{rad}$. This is an obvious consequence of the shape of the blankets. As is seen in Figure 3.3, as soon as a ray is launched from a too steep angle, it hits the blankets on the way to the plasma, making an unperturbed trajectory impossible. For a blanket interspace $2h = 30\,\text{mm}$, this happens at

$$\theta = \tan^{-1}\Big(\frac{15}{135}\Big) = 0.11\,\text{rad} \tag{4.6}$$

when the ray is launched from the aperture. Because the rays are launched from a focal point slightly behind the aperture the limiting value lowers a bit to about 0.1 radians, setting a hard limit for unperturbed trajectories.

The sometimes very high probabilities on return starting around 0.75 rad and extending up to 0.9 rad in Figure 4.5 and B1 are noteworthy. These zones contain rays which are launched in sidelobes and are reflected directly from the blankets back to the receiver antenna. Of course these direct reflections are unwanted effects and in Sections 4.2.5 and 4.2.6 the consequences of these reflections will be discussed. With a small safety margin, it can be said that for the PPR

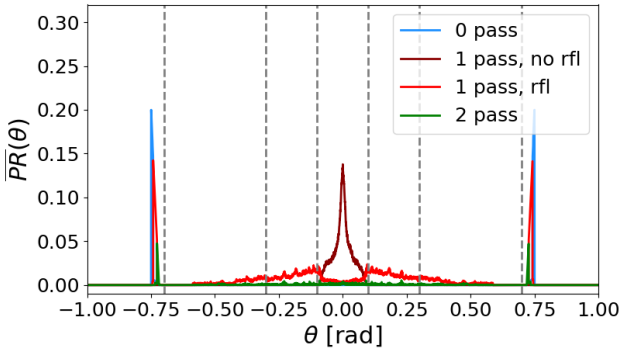

(a) SINC14

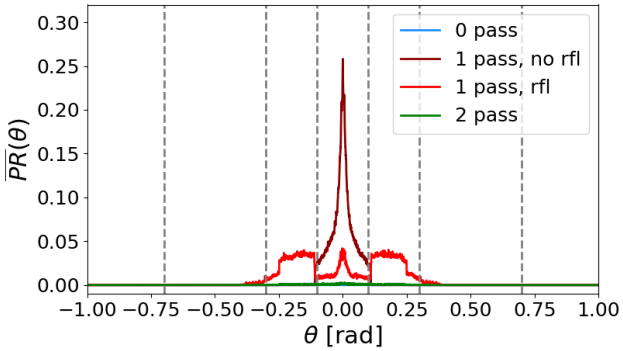

(b) TEM_{00}: $w_0 = 0.588\lambda$, $D = 14\,\mathrm{mm}$

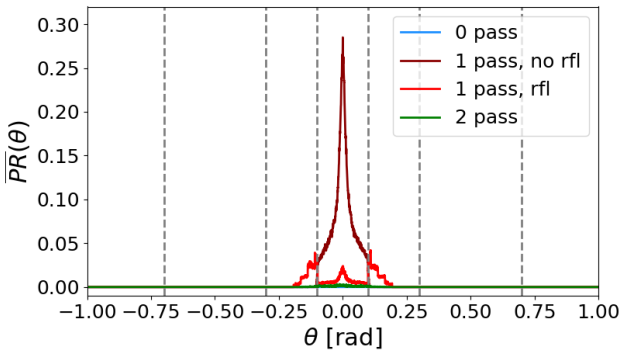

(c) TEM_{00}: $w_0 = 1.2\lambda$, $D = 28\,\mathrm{mm}$

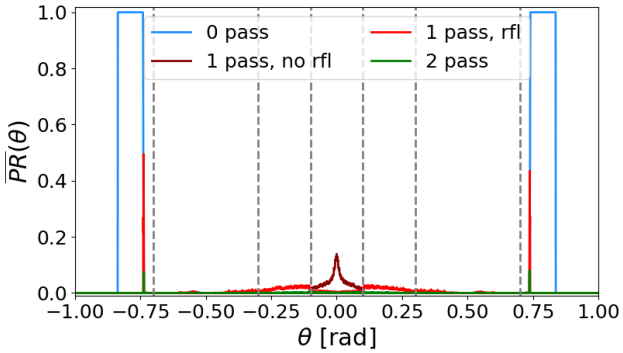

(d) (different y-scaling) $60\,\%TEM_{00}/40\,\%TEM_{10}$: $w_0 = 0.588\lambda$, $D = 14\,\mathrm{mm}$

Figure 4.5: Probability on return for different antennas averaged over different frequencies and turbulence levels. Dotted lines are drawn at $|\theta| = 0.1\,\mathrm{rad}$, $0.3\,\mathrm{rad}$ and $0.7\,\mathrm{rad}$

application in ITER, rays with

$$|\theta| > 0.7\,\mathrm{rad} \tag{4.7}$$

are unwanted.

A third boundary can be identified around

$$|\theta| = 0.3\,\mathrm{rad} \tag{4.8}$$

Although this boundary lies at slightly smaller values for some antennas, $|\theta| = 0.3\,\mathrm{rad}$ can be used as safe upper limit to say that rays have a relatively high chance to return to the receiver when launched at smaller angles and have low chance of contributing to the received signal when launched at larger angles.

In the figures, the green line representing the probabilities for a ray passing through the plasma twice before returning to the receiver is always quite low. Of course this does not mean that it is not possible that these trajectories are very present in a single simulation run, but based on the average behaviour no criteria for this type of trajectories can be found.

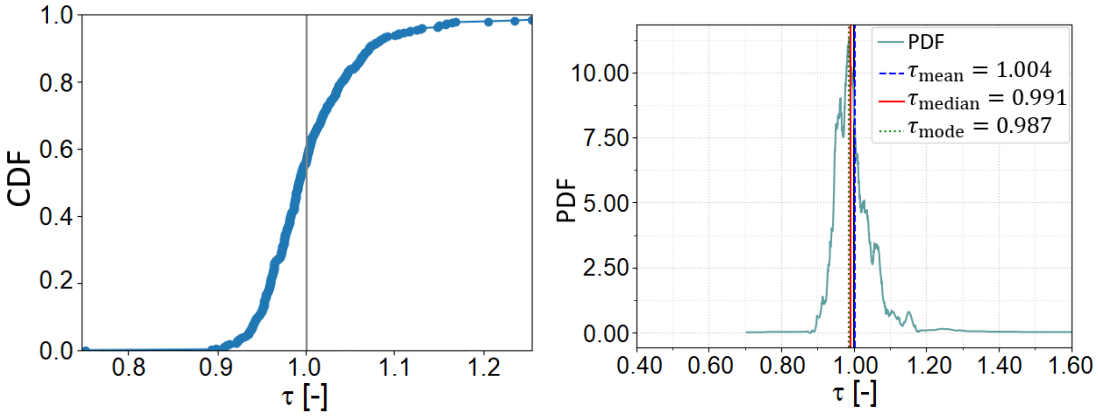

(a) cumulative distribution function (b) probability density function

Figure 4.6: Probability distribution for normalized time of flight for SINC14 at 30 GHz and 3 % turbulence. In (b) the mean, median and mode characterize the average time of flight.

4.2.4 Time of Flight

From the collected power (Section 4.2.1), it is possible to calculate the time of flight (ToF) of a single simulation using the scheme presented in Appendix A. With the time of flights calculated for each simulation, a statistical interpretation can be made and the cumulative distribution function (CDF) using the normalized time variable τ is constructed. Probability density functions (PDF) of the ToF can be calculated for a given frequency and turbulence level. An example is given in Figure 4.6. Because of the limited number of simulations, the CDF is not that smooth, so that when deriving this function to obtain the PDF, it results in erratic distribution functions. It is still possible to draw conclusions from the distributions, but repeating the simulations with e.g. 1000 repetitions instead of 400 could give more accurate results. It was found that when turbulence increases for a fixed frequency the ToF distribution broadens and the distribution becomes asymmetric with a long right tail. This agrees with the expectations that with increasing turbulence the trajectories of the rays in the plasma will differ more from the non-turbulent case (resulting in broadening) and that some turbulence phase matrices result in rays which pass through the plasma quicker than in the non-turbulent case and others (which become more dominant for high amounts of turbulence) result in longer trajectories, hence the long right tail. These tendencies are seen for all simulated antennas.

When looking at the mean of the distributions, it is noticeable that Gaussian patterns with large w_0 and the SINC14 pattern often have a ToF mean closer to $\tau = 1$ than the other tested patterns. When comparing the variances of the distributions, the fundamental Gaussian patterns result on average in less broad distributions than the other antennas. For each PDF the mean and variance of the ToF distribution can be found in Tables B2 and B3 in Appendix B. In Table B3, a color code is used to indicate the asymmetry of the distributions based on the skewness.

Apart from these observations, the question rises if the ToF distributions of

different antennas are significantly different from each other or not. To quantify whether or not the differences are significant, the Kolmogorov-Smirnov test (KS) with a 99 % confidence interval was done. Also the Kullback-Leibler (KL) divergence was calculated between the distributions of different antennas while keeping frequency and turbulence level constant. These tests were done once relative to the SINC14 pattern and once relative to the antenna with 100 % TEM_{00} and $w_0 = 0.588\lambda$. With the KS-test, it is found that in most cases for low turbulence levels (0.25 % and 1 %) at all frequencies the time-of-flight CDF of the SINC14 pattern are not significantly different from any of the tested antennas, which indicates that all antennas function in similar ways at these amounts of turbulence. However, the opposite is true for medium amounts of turbulence (3 % and 5 %), where almost all tested antennas show significantly different PDFs from the SINC14 results. At high levels of turbulence (10 %) the differences are again less often significant but the KL divergence is high for all distributions. This means that the main differences on the time-of-flight distributions in comparison with the reference antenna are present for the medium and high turbulence levels, rather than the low turbulence levels. It is normal that this is the case; when turbulence rises, the chances on turbulent density regions introducing high deflections increase. Any differences present in how much power is radiated in which direction has then also bigger consequences, in other words: variations in radiation diagram will result in more explicit different behaviour as turbulence rises, resulting in more significant differences in the ToF distributions.

When taking the TEM_{00} with $w_0 = 0.588\lambda$ pattern as reference, the results are slightly different. The tested superpositions of TEM_{00} and TEM_{10} have only in very few cases significantly different ToF distributions from the reference according to the KS-test, and these differences can be contributed to the different constraints used in R2P2 for these antennas[1]. For the other tested antennas, the comparison with the TEM_{00}, $w_0 = 0.588\lambda$ reference results in similar conclusions as made before with the SINC14 pattern as reference. These tests indicate that Gaussian superpositions which have the same beam waist-wavelength relation result in similar ToF distributions and PPR behaviour. The results of the KS-test and the KL distances can be found in Tables B4 and B5 in Appendix B.

From the results of the KS-tests and the KL distances between the distributions, as well as the initial observations on mean and variance, it is clear that it is possible to influence the distribution of the time of flight by changing the used antennas and that especially for high frequencies and turbulence levels the differences in distribution are significant. It was also seen that a fundamental Gaussian pattern and superpositions based on the same waist-wavelength relation have more similar behaviour than when the beam waist-wavelength relation is changed. Because the ToF variance of the distributions was lower for fundamental Gaussians and the ToF mean was closer to the non-turbulent value for Gaussians with high w_0 as well as for the SINC14 pattern, it can be concluded

[1]Only at 0.25 % turbulence the KS-test gives significant differences. The distributions at this low turbulence are very narrow and it is seen that there is a slight difference in mean of the distributions, explaining the result of the KS-test. The difference in mean can be explained by the different approaches used for launching and receiving the rays, explained in Section 3.4.2

that fundamental Gaussian patterns are preferable over superpositions that include higher-order Gaussians.

4.2.5 Invalid Runs

In the distribution functions that were discussed in the previous part, some simulation results were not taken into account because the receiver antenna did not receive any useful signal. This can occur when turbulent regions deflect all radiated power away from the receiver or when some power from the main beam does return to the receiver but the power returning to the receiver without the rays going through the plasma (e.g. from sidelobes such as in Figure 4.5a and 4.5d) dominates, so that the reconstructed time of flight is not close to $\tau = 1$ anymore. The chance on either of these scenarios increases with turbulence and frequency, so it is expected that the number of invalid runs will be larger when frequency and/or turbulence level rise. In a real PPR system, these invalid runs correspond to a moment on which the PPR system is not able to give a prediction on the plasma position, making the percentage of invalid runs relevant for the performance of a PPR system. For most antennas, at low levels of turbulence and low frequencies almost all 400 simulations are valid. When the frequency and the turbulence rise, also the amount of invalid runs rises, which agrees with the expectations. When comparing the antennas by their average percentage of invalid runs over all frequencies and all turbulence levels, all fundamental Gaussian patterns have less than 7 % invalid runs, all others have between 7 and 10 % invalid runs. For the high amounts of turbulence this difference is even larger: at 10 % turbulence, fundamental Gaussians have on average 9 to 14 % invalid runs, other antennas have 16 to 19 %. This supports the claim that direct return from sidelobes increases the chance on invalid runs. The tabulated fractions of invalid runs depending on the antenna, frequency and turbulence are given in Table B6 in Appendix B.

4.2.6 Antenna Coupling

Another good way to express the performance of a PPR antenna is is by looking at the average total power return of the antenna in different conditions (frequencies and turbulence levels). To do this, for each antenna the probability on return $\mathrm{PR}(\theta)$ (Fig. 4.3(right)) is weighted with the radiation diagram $W(\theta)$, giving the weighted probability on return WPR:

$$\mathrm{WPR}(\theta) = \mathrm{PR}(\theta) \cdot W(\theta) \tag{4.9}$$

When integrating this quantity, an indication of the average returned power, i.e. of the coupling between the emitter and the receiver antenna, is found:

$$\int \mathrm{d}\theta \ \mathrm{WPR}(\theta) \tag{4.10}$$

This calculation can be made separately for different types of ray trajectories: for rays which have an unperturbed trajectory (passing once through the plasma

and returning to the receiver without any reflections on the blankets), trajectories with blanket reflections, trajectories with multiple passages through the plasma or trajectories which return without a passage through the plasma. The results of these calculations for the simulated patterns are presented in Figures 4.7, 4.8 and 4.9 and in Figures B2, B3 and B4 in Appendix B. The total returned power corresponds to the top level of the bar charts. For SINC14, the values in Figure 4.7a can be compared with Figure 4.4, which depicts the same quantity retrieved through a different statistical method. It is noted that they are not identical: the bar charts always give an overestimate of the median returned power. This does not come as a surprise, since the method using Equation 4.9 does not take into account that two neighbouring rays at slightly different angles, each with a 1 % chance on return, might only return both at the same time in very few cases. Eq. 4.9 will integrate the power density between these rays weighted with the 1 % probability on return, whereas the other method, based on the median of individual simulations, will only take this power density into account if the neighbouring rays have both returned in the same simulation. Although the power is always slightly overestimated, the behaviour that is visible on Figure 4.4 is still seen in $\int$ WPR and this quantity offers new useful insights.

In the charts it can be seen that the power fraction contained in rays returning after a direct wall reflection (blue), as well as rays returning after a double passage (green) through the plasma are on average very low and often not even visible on the figures. The superpositions of TEM_{00} and TEM_{10} (e.g. Fig. 4.7b) form an exception on this and show a constant blue part at the bottom of each bar. This is power coming from sidelobes which are launched towards the metallic walls which are, instead of propagating in the direction of the plasma, reflected directly to the horn. The power fraction rises proportional to the amount of TEM_{10} in the antenna diagram. For a 90/10 TEM_{00}/TEM_{10} mix the power is $6.6\,10^{-5}$ of the emitted power, but in the case of a 60/40 TEM_{00}/TEM_{10} mix, the fraction is 0.08 % of the emitted power and relative to the received power it reaches average values up to 15 % for 60 GHz with 1 % turbulence. The rays undergoing such a trajectory can be a heavy distortion on the received signal, which makes the superpositions of TEM_{00} and TEM_{10} not suited for PPR applications.

It is also noticed that for fundamental Gaussian patterns with the same aperture size but different $w_0(\lambda)$ relations (such as Fig. 4.8a-b or Fig. 4.9a-b) the diagram with the constant maximum waist $w_0 = w_{0,max}$ has larger returning power fractions for the higher frequencies than the pattern which has a beam waist proportional to the wavelength (Eq. 4.2). At lower frequencies these patterns however show very similar behaviour. This is of course a consequence of the shape of the radiation pattern: in Fig. 4.1a,c and Fig. 4.2a,b it is seen that the antennas with $w_0 = w_{0,max}$ have a more focused beam than their $w_0 \propto \lambda$ counterpart, especially for the higher frequencies. This means there is more power present in the central region with a higher chance of returning to the receiver.

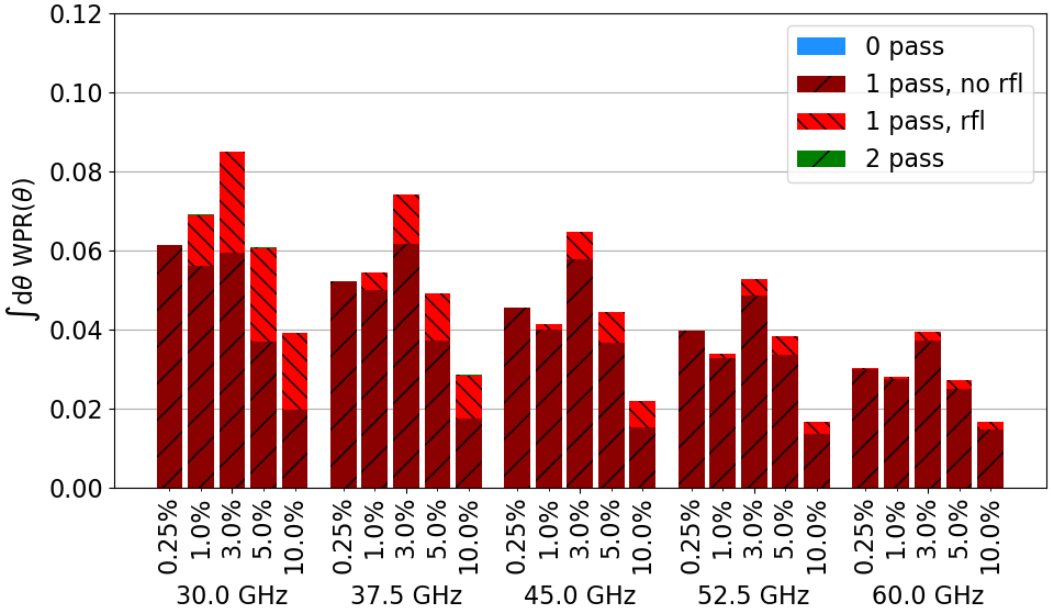

(a) SINC14

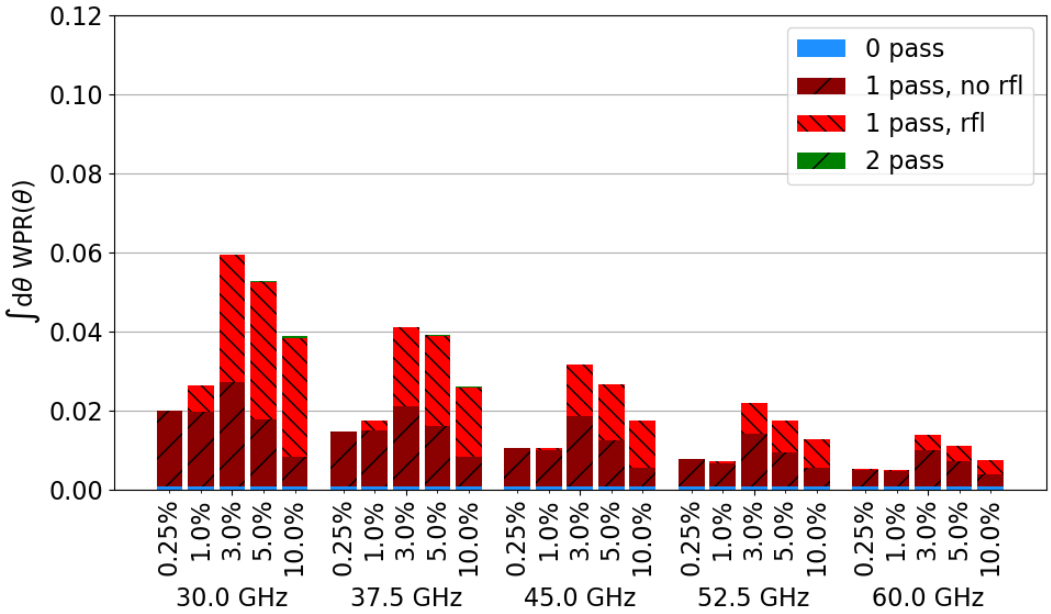

(b) $60\,\%TEM_{00}/40\,\%TEM_{10}$: $w_0 = 0.588\lambda$, $D = 14\,\text{mm}$

Figure 4.7: $\int d\theta$ WPR(θ) for various simulated antennas at different frequencies and turbulence levels. Colors indicate the type of trajectory the returned ray has taken.

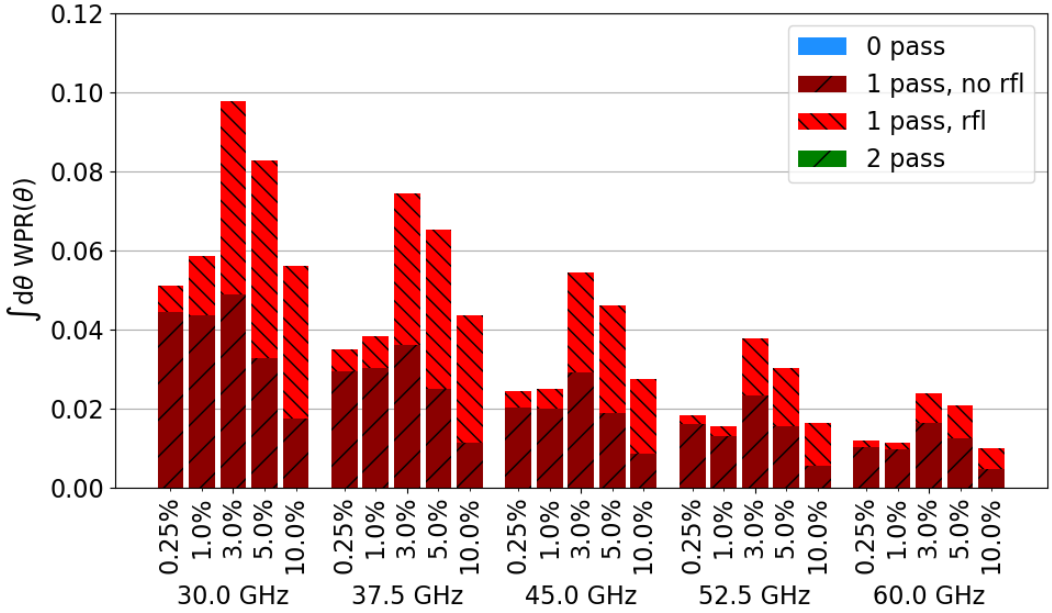

(a) TEM_{00}: $w_0 = 0.588\lambda$, $D = 14\,\mathrm{mm}$

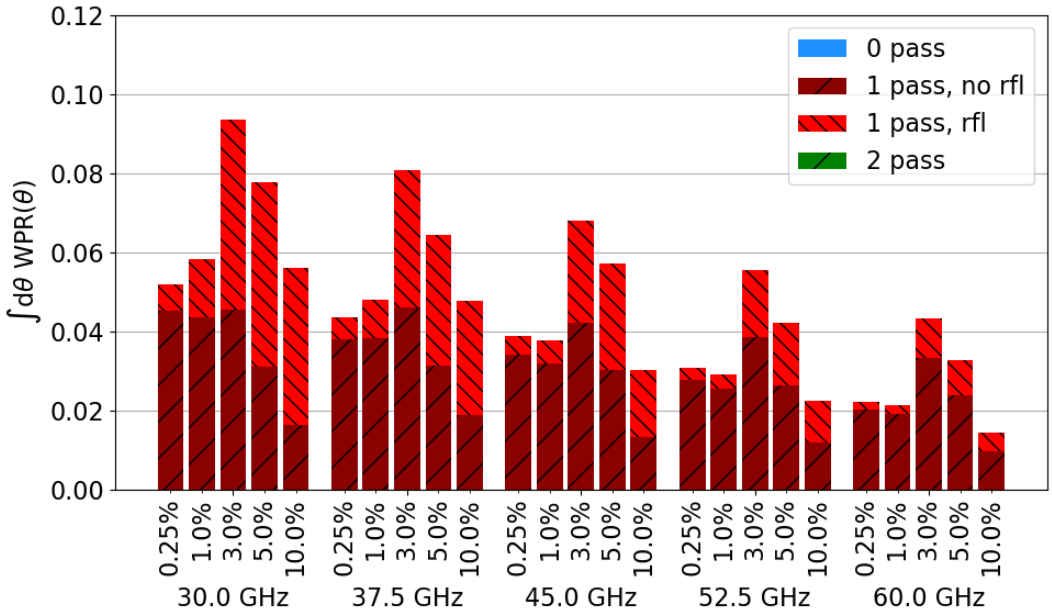

(b) TEM_{00}: $w_0 = 5.88\,\mathrm{mm}$, $D = 14\,\mathrm{mm}$ (fixed beam waist)

Figure 4.8: $\int \mathrm{d}\theta$ WPR(θ) for various simulated antennas at different frequencies and turbulence levels. Colors indicate the type of trajectory the returned ray has taken.

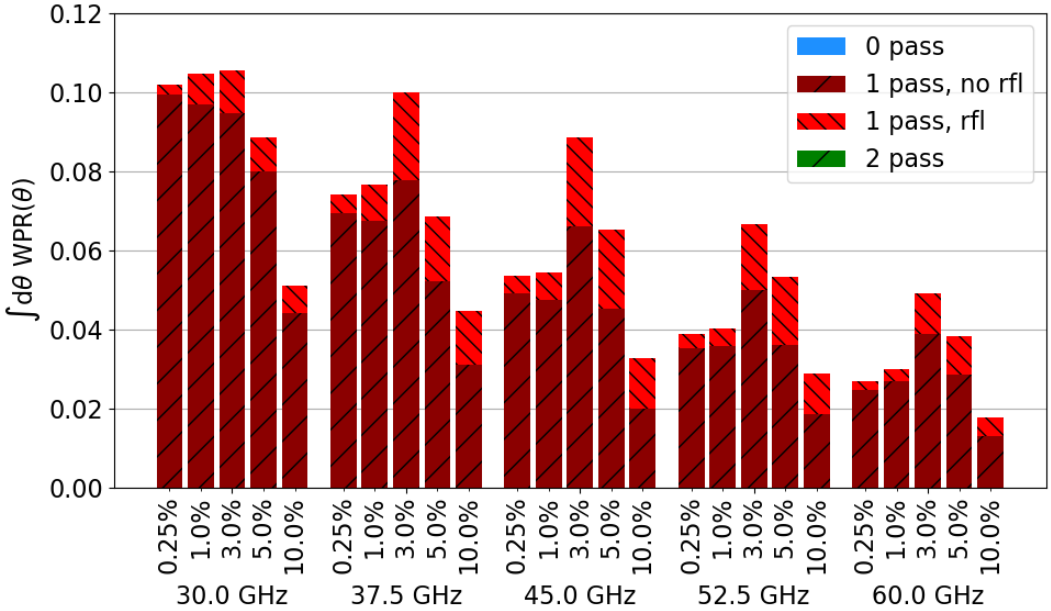

(a) TEM_{00}: $w_0 = 1.2\lambda$, $D = 28\,\text{mm}$

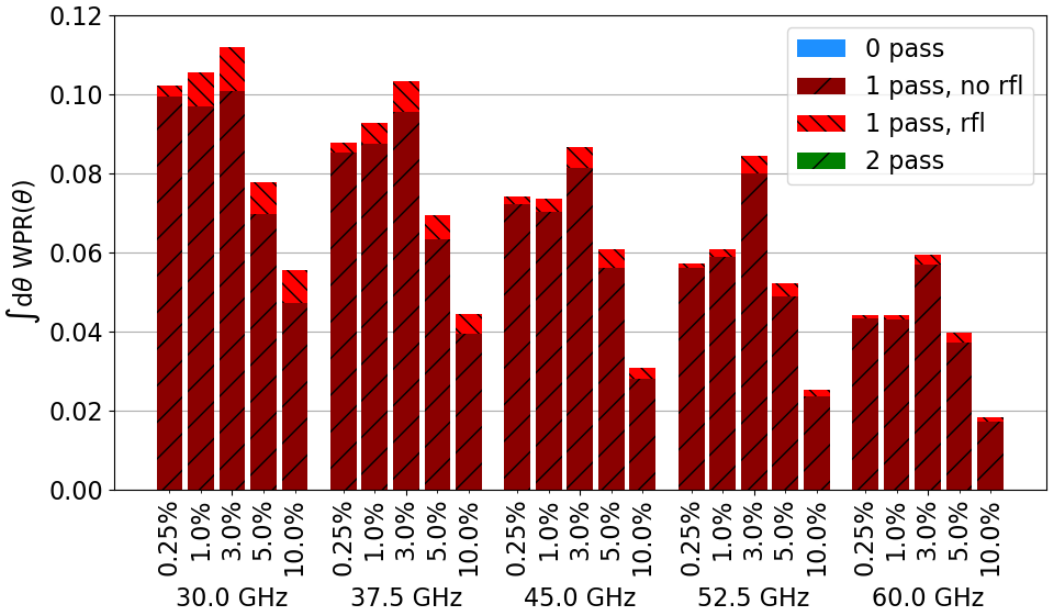

(b) TEM_{00}: $w_0 = 12\,\text{mm}$, $D = 28\,\text{mm}$ (fixed beam waist)

Figure 4.9: $\int d\theta$ WPR(θ) for various simulated antennas at different frequencies and turbulence levels. Colors indicate the type of trajectory the returned ray has taken.

Further comparison between the bar charts shows that the diagrams with larger aperture (Fig. 4.9) receive more returning power than diagrams with smaller aperture (e.g. Fig. 4.8). Most noticeable is that these antennas do also receive more power of unperturbed trajectories. This is a consequence of the Gaussian character of the antenna and the large fraction of power in the central region ($|\theta| < 0.1\,\text{rad}$) which is the only region in which such unperturbed trajectories are possible. The increased beam waist, which is possible thanks to the larger aperture size, is clearly beneficial, with the returned power reaching up to 10 % of the emitted power at low frequencies and low turbulence and still almost 2 % at the highest simulated frequency and turbulence level.

Also the SINC14-pattern (Fig. 4.7a) has high amounts of received power coming from unperturbed trajectories. This pattern also has strongly focused beams and despite its small aperture size, it has high $\int \text{WPR}$ values for higher frequencies. It can be seen that especially for high frequencies, these unperturbed trajectories contribute a lot to the received power.

It is possible for a certain value in the bar chart to be obtained in various ways. For example both SINC14 and the Gaussian patterns with $D = 28\,\text{mm}$ (Fig. 4.9) have $\int \text{WPR} \approx 0.02$ for 60 GHz at 10 % turbulence. However this average behaviour says nothing about the width of the distribution: the SINC14 pattern has almost 40 % probability on invalid runs for this case, meaning that the mean value is an average of high values in which the central part of the beam reaches the receiver and a lot of cases with no return at all. For the Gaussian patterns, the invalid run probability is a lot lower, so that the bar chart value is more often close to the actual behaviour of the antenna.

The Gaussian pattern with $w_0 = 0.588\lambda$ and $D = 14\,\text{mm}$ always has a large part of its power located outside of the $|\theta| = 0.1\,\text{rad}$ limit, contributing to indirect returning rays, which is clearly visible in the large bright red parts of Figure 4.8a. Although not ideal, this power makes the total fraction returning to the receiver still quite high and for low frequencies sometimes even in fractions comparable with the far more focused SINC14-pattern. The Gaussian pattern has an additional advantage over the SINC14 antenna that it has lower chances on invalid runs, again suggesting a good performance.

4.2.7 R2P2 Simulation Conclusions

For all antennas the returning power peaks at 3 % turbulence when keeping the frequency constant, which is explained by the initial broadening of the probability on return $\text{PR}(\theta)$ as turbulence rises, an effect that is overshadowed by a general lowering of $\text{PR}(\theta)$ as turbulence rises even higher. Both are a consequence of turbulent regions deflecting the rays, either towards the antenna (broadening $\text{PR}(\theta)$) or away from the antenna (lowering $\text{PR}(\theta)$). When increasing the frequency and keeping turbulence level constant, the returned power lowers gradually as a consequence of the larger turbulent region through which the rays travel up to the cut-off layer, which increases the chance on deflections.

The time-of-flight distributions of the antennas were compared, from which it was concluded that the largest differences in distribution were found at interme-

diate to high levels of turbulence (starting at 3 %) and that the distributions of antennas with the same beam waist-wavelength relation are more similar to each other than when this relation is changed. Often the found distributions were significantly different, but it is difficult to draw conclusions on which distributions are better, since this would depend on the plasma position reconstruction method used.

Several regions of the antenna diagram were identified, which contribute in different ways to the returning power:

1. Power radiated with $|\theta| < 0.1\,\text{rad}$ has a high chance on returning with an unperturbed ray trajectory.
2. Power radiated with $0.1\,\text{rad} < |\theta| < 0.3\,\text{rad}$ has a high chance on returning to the receiver after a single passage through the plasma with some blanket reflections.
3. Power radiated in $0.3\,\text{rad} < |\theta| < 0.7\,\text{rad}$ does not contribute much to the received power.
4. Power radiated in $|\theta| > 0.7\,\text{rad}$ has a chance on causing direct reflections and should be minimized.

A lot of different aspects of antenna PPR performance were evaluated using the R2P2 code. Because some antennas performed well on certain aspects but bad on other aspects, it is not possible to make a full ranking of the antennas based on their performance. However, fundamental Gaussian antennas with a large aperture and beam waist (frequency-independent or not) have clearly the best characteristics: a low number of invalid runs and high antenna coupling with a high amount of power coming from unperturbed trajectories. Also it is clear that superpositions of TEM_{00} with TEM_{10} are not suited for PPR purposes: their antenna coupling is low and their number of invalid runs is very high, which can be linked with the presence of sidelobes at $|\theta| > 0.7\,\text{rad}$.

All the above conclusions are made by using only a single, homogeneous turbulence model. For a different turbulence model (e.g. turbulence limited to a radial region in the plasma) some effects could change, in particular the frequency dependence of the antenna coupling could be less present for inhomogeneous turbulence.

Chapter 5

Antenna Design

5.1 Radiation Diagram Choice

Considering that the tolerances for the installation of the components in ITER are expected to be in the order of a few mm [11], the theoretical antenna with $w_0(\lambda) = 0.588\lambda$ and $D = 14\,\text{mm}$, shown in Fig. 4.1a seems the best option for a frequency-independent PPR antenna for ITER. If more space would be available, a more performant antenna with larger aperture and fundamental Gaussian radiation patterns could be used.

A direct comparison of the R2P2 simulation results of the selected antenna and those of the SINC14 antenna, which is used in the current ITER PPR design (but which is strongly frequency dependent and therefore less suited for plasma reconstruction methods based on neural network or databases), the Gaussian has better performance when it comes to number of invalid runs, especially for high amounts of turbulence (at 10 % turbulence on average 9 % invalid runs against 19 % for SINC14) and has a lower variance in the ToF probability distribution. Both antennas have similar amounts of power returning to the antenna at low frequencies, but the SINC14 antenna has better antenna coupling at higher frequencies. It is an inevitable consequence of a frequency-independent antenna that it has a broader main lobe than a frequency-dependent antenna at high frequencies, which explains this behaviour. Because of the broader main lobe of the Gaussian, the returning power for this antenna is more often from indirect trajectories (with parasitic wall reflections) rather than from unperturbed trajectories. A consequence from this is that the ToF mean is almost always a bit higher for the Gaussian pattern than that of the SINC14 pattern. Both antennas have advantages and disadvantages, making it difficult to state that one would have an overall better performance than the other, but given the constraints on the antenna size and the necessity to construct an antenna with a frequency-independent radiation diagram, the fundamental Gaussian with $w_0(\lambda) = 0.588\lambda$ is the best available option for ITER.

This choice of radiation pattern is so far purely theoretical. It still needs to be determined which antenna shape (if any) results in the desired radiation patterns.

5.2 Antenna Design

To find an antenna shape which has the wanted characteristics, an optimization is done using PROFUSION [20], a Linux commandline code package containing numerous tools to calculate microwave beam phenomena. A cylindrical antenna optimizer, based on a combination of simulation annealing and a downhill simplex method [21], is available and provides the possibility to optimize an antenna shape to resemble aperture fields as close as possible. The aperture fields of Gaussian beams are uniquely defined by the same characteristics as those that identify the radiation diagram (i.e. w_0, λ and for higher-order modes their relative phase and intensity), making it possible to launch the optimizer using the parameters which were used in the R2P2 simulations: frequencies 30, 37.5, 45, 52.5 and 60 GHz with $w_0 = 0.588\lambda$ are used as input fields to define the optimization goal. Additional geometrical parameters need to be given to the optimizer: D_1, the input diameter of the antenna at the waveguide end; $D_{\max}$, the maximum aperture diameter (also limiting the diameter that the antenna can have at any location apart from the aperture); l and Δl, the nominal length of the antenna and the tolerated deviation from it; $\theta_{\max}$ and $\theta_{\min}$, an upper and lower boundary for the slope of the geometry function $r(z)$ which describes the antenna shape.

A lower limit to D_1 is given by the cut-off frequency of the waveguide that feeds the antenna. Equation 2.18a gives that a waveguide with $D = 6\,\text{mm}$ has a TE_{11} cut-off frequency $f_c = 29.28\,\text{GHz}$, meaning that the frequencies in range $f \in [30\,\text{GHz}, 60\,\text{GHz}] > f_c$ can propagate through it. It is safe to take a margin on this minimum, leading to $D_1 = 8\,\text{mm}$. $\theta_{\max} = 90°$ and $\theta_{\min} = 0°$ were initially chosen to find an optimal diverging antenna. This type of antenna has the advantage of easy production over antennas with more exotic shapes. $D_{\max}$ was originally chosen to 14 mm, matching with the size of the SINC14 reference. Also the nominal length was chosen to match with the reference antenna used by Valera [11], $l = 115\,\text{mm}$, with $\Delta l = 10\,\text{mm}$.

The antennas generated with the initial parameters did unfortunately not give a satisfying result: optimizations were either not converging or finding an optimum with too much radiation in unwanted regions that showed frequency-dependent characteristics in at least a part of the $30 - 60\,\text{GHz}$ octave. This indicates that the design constraints were too tight. First the parameters Δl and $\theta_{\min}$ were loosened gradually. When this did not give better results, also $D_{\max}$ was increased. Only with $\Delta l = 70\,\text{mm}$, $\theta_{\min} = -60°$ and $D_{\max} = 20\,\text{mm}$ a good optimization was found, having on average only 1.67 % of its power in modes different from the wanted fundamental Gaussians. The resulting optimal antenna shape is seen in Figure 5.1 and 5.2.

The antenna shape is not, as was first intended, monotonically flared outwards, but has two diverging sections with in between a converging section. This makes the manufacturing process is more difficult than for a monotonically flared antenna. Also $D = 19.598\,\text{mm} > 14\,\text{mm}$ is not ideal, since it is not sure that the antenna will easily fit in between the blanket interspace: with a mounting precision of 2 mm for both blankets and antenna this antenna would still fit in the reserved space. When the precision is worse than 2 mm, it is not guaranteed that the antenna would fit. The optimized antenna has $\text{MAX}(w_0)/D = 0.3$. Under the

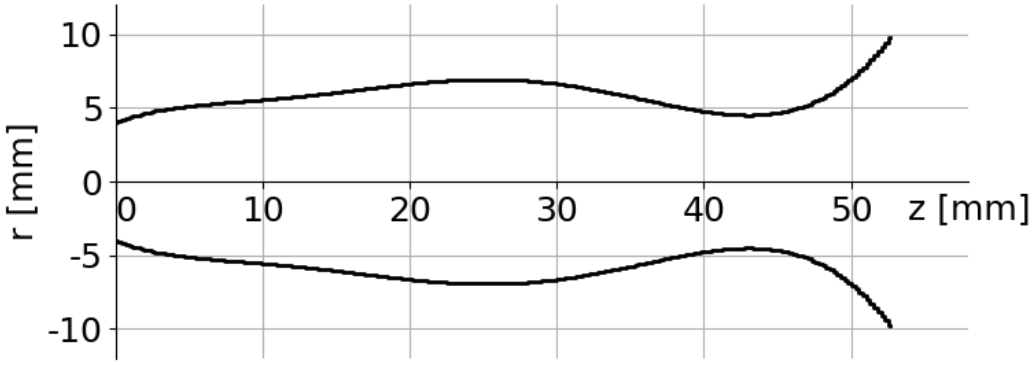

Figure 5.1: Optimized antenna shape with $D_{\text{in}} = 8\,\text{mm}$, $D = 19.598\,\text{mm}$, $l = 52.678\,\text{mm}$. The antenna has on average 98.33 % overlap with the optimization goal i.e. the fundamental Gaussian patterns with $w_0 = 0.588\lambda$.

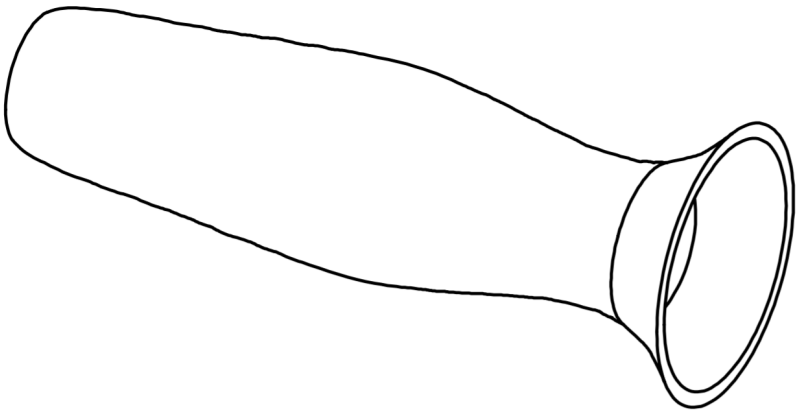

Figure 5.2: Trimetric view of a possible realization of the optimized antenna.

assumption that the required frequency-independent optimization can always be done with this ratio, it would be possible to make an antenna with $w_0(\lambda) = 0.42\lambda$ for $D = 14\,\text{mm}$. This type of antenna would however have a broader pattern with more power radiated in the unwanted $|\theta| > 0.7\,\text{rad}$ region. It is preferable to keep the slightly larger aperture antenna with $w_0 = 0.588\lambda$.

Because of the choice for $D_1 = 8\,\text{mm}$, some higher-order modes can exist in the antenna input. In Table 2.2 it is seen that for a cylindrical waveguide with diameter 8 mm not only the fundamental TE_{11}, but also the TM_{01} exists for the whole frequency band of 30 to 60 GHz and TE_{21} exists for almost the whole frequency band. When the antenna input field contains one of these modes, this might lead to changes in the resulting radiation pattern. One of the things which can change is the direction of the main lobe, which can have large influence on

the resulting blanket effects. PROFUSION simulations were done with 1 % of one of the higher-order modes at the antenna input. For none of the frequencies did 1 % TM_{01} result in any significant angular offset in the poloidal direction. However, 1 % TE_{21} resulted in sometimes large offsets of maximum 1.54° at 37.5 GHz (with 180° relative phase between TE_{01} and TE_{21}) and 1.24° at 45 GHz (with 270° relative phase). At other frequencies the offsets were limited to less than 1°. This means that extra care must be taken in the design of the transmission line to the PPR antennas to avoid these higher-order modes, which is not easy considering that the oversized waveguides leading to the PPR antennas in ITER will be very long and involve a lot of bends [26]. If higher-order modes at the antenna input are inevitable, another option would be to make a new antenna optimization which uses the actual antenna input. For this a mode analysis of the transmission line should be done first.

Chapter 6

Antenna Prototype Testing

The PROFUSION tools used to optimize the antenna shape are a mature software package and can be trusted to give correct results. However, because the optimization is done on the antenna aperture fields, the cylindrical antenna optimization tool does not allow external structures such as blankets to be modelled during the optimization. This limitation means that the optimized antenna might suffer from similar effects as described by Valera et al for square aperture antennas [11]: apart from introducing the multi-reflections (discussed in Chapter 4), the metallic blankets can also drastically change antenna radiation patterns. To assess the performance of the antenna when mounted between blankets, a prototype of the optimized antenna, and a conical reference antenna were built and radiation pattern measurements were made for both antennas with and without mock-up blankets.

6.1 Measurement Setup

Prototypes of the optimal antenna (see Chapter 5) and a conical reference antenna with the same length ($l = 52.678\,\text{mm}$) and the same input and output diameter ($D_{\text{in}} = 8\,\text{mm}$ and $D = 19.598\,\text{mm}$) as the optimized antenna were made. The antennas were milled out of a 28 mm diameter aluminium cylinder, the outer diameter of the block was not milled but left at 28 mm, reducing the production cost and simplifying mounting the antennas in a measurement setup.

A mock-up version of the ITER blanket structure was made from aluminium. The blanket geometry is prescribed by Figure 3.3 in the poloidal plane (in particular the value of $L = 120\,\text{mm}$ is important) and the blankets are 153 mm long in toroidal direction, which is the same as used by Belo et al in [35]. To guarantee that the distance between the blankets is $2h = 30\,\text{mm}$, two cylindrical spacers are placed between the blankets. The antenna mounted in the blanket structure is illustrated in Figure 6.1a. Also depicted at this figure is the transition from the antenna input diameter $D_{\text{in}} = 8\,\text{mm}$ to a standard WR-28 waveguide, so that this the antenna can easily be connected to standard components.

Measurements at 30, 37.50, 45, 52.50, and 60 GHz are done. The two lowest frequencies are located in the Ka-band ($26.5 - 40\,\text{GHz}$), the others fall in the V-band ($40 - 75\,\text{GHz}$). Since the V-band frequencies can propagate in Ka-band

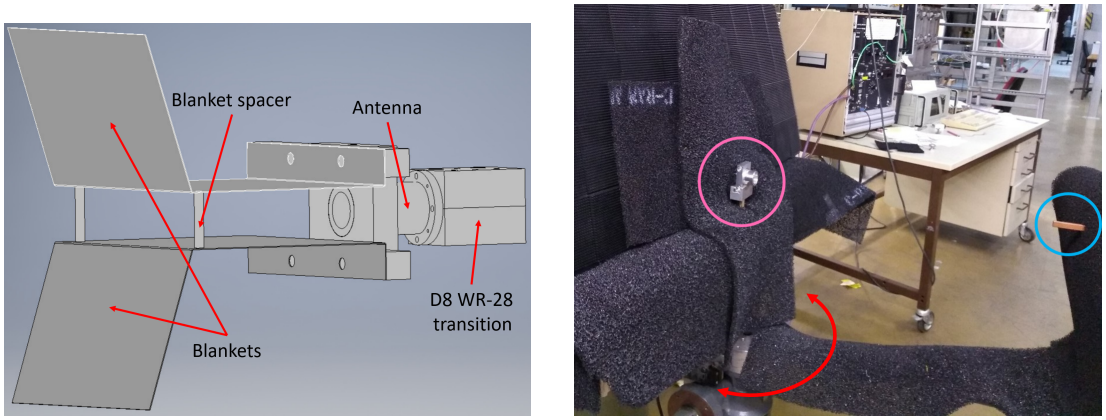

(a) (b)

Figure 6.1: (a) Assembly drawing of a prototype antenna surrounded by a blanket structure, (b) laboratory setup with the test-antenna (pink circle) mounted on pivot point and the receiver (blue circle) mounted on a rotating arm.

waveguides (Eq. 2.19), a single transition piece from a cylindrical waveguide with diameter 8 mm to a WR-28 Ka-band waveguide can be used for all measurements. For the V-band measurements an extra transition follows on this from WR-28 to WR-15, the V-band standard waveguide. The measurement accuracy is

$$\max\left(0.2\,\mathrm{dB}, 0.01 S_{\mathrm{dB}}\right)$$

with S_{dB} the measured signal amplitude. Although measurements at 45 GHz can be done with the V-band equipment, there is a chance that the accuracy of these measurements is worse than given above, because the used network analyzer specifies the V-band only for the range $50 - 75$ GHz.

To obtain the radiation patterns of the antennas, the poloidal, toroidal and cross-polarized electric fields radiated by the antennas will be measured. The test-antenna (with or without blankets) is used as emitter while a open-ended WR-28 waveguide, functioning as receiver, rotates around it and registers the both the amplitude and phase of the electric field. A picture of the setup is given in Figure 6.1b. All metallic objects in the direct environment of the measurements are covered with microwave absorbing material (black on Fig. 6.1b) to minimize their effects on the measurements. The distance between the transmitting and receiving antenna was 50 cm. With the far-field starting at 16 cm (Eqs. 2.26 evaluated for all frequencies, the most strict condition is obtained from Eq. 2.26a at 60 GHz), the measurements are taken in the Fraunhofer region, where the antenna diagram is independent of the distance on which it is taken.

6.2 Radiation Diagram Analysis

The results of the comparison between reference and optimized antenna are presented in Figures 6.2 and 6.3. The radiation patterns are normalized using Eq. 3.15. Only the measurements in the poloidal plane are given in the graphs, since these are the most relevant for plasma position reflectometry. In Figure

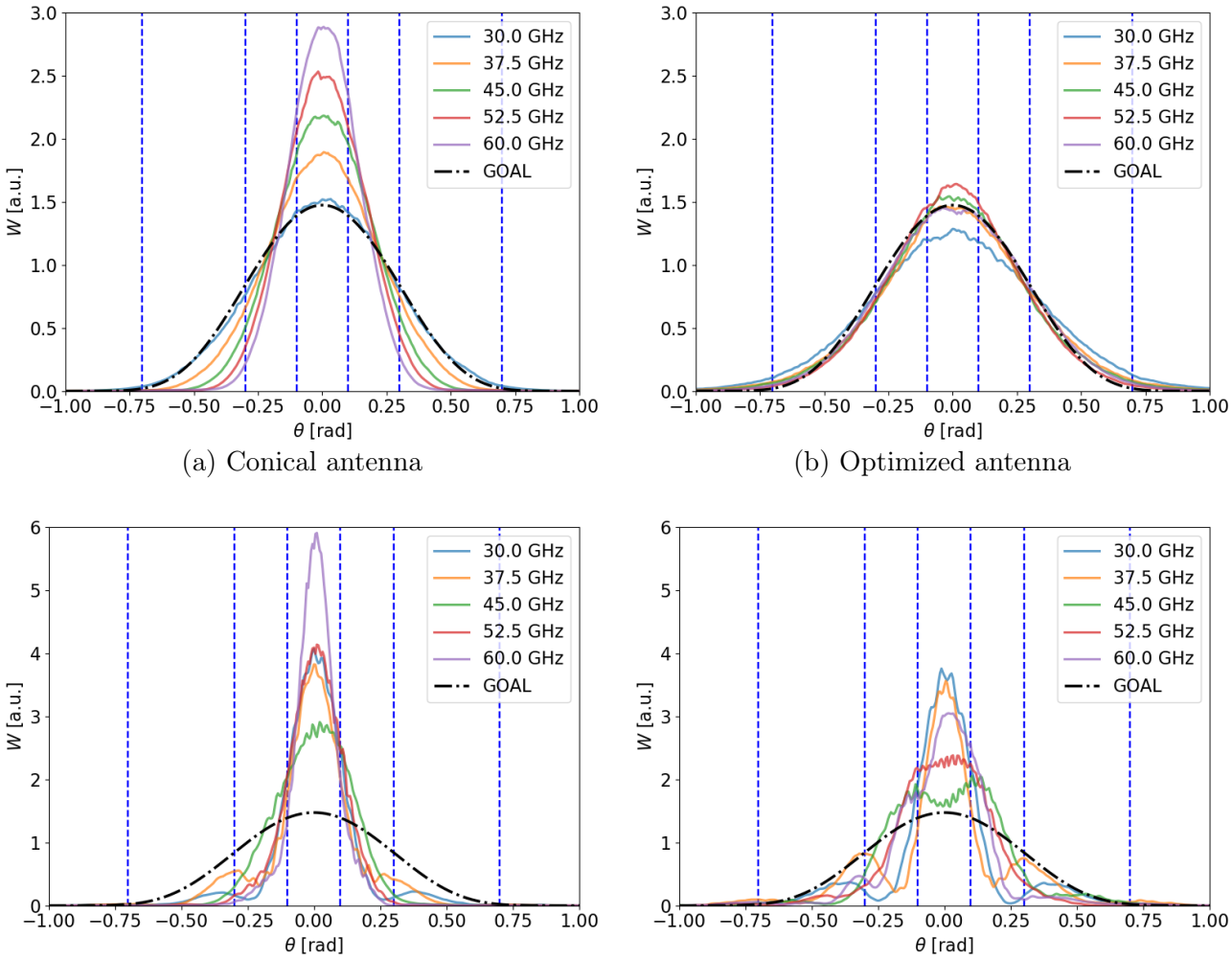

(a) Conical antenna

(b) Optimized antenna

(c) Conical antenna with blankets

(d) Optimized antenna with blankets

Figure 6.2: Linear-scaled poloidal (H-plane) radiation diagrams of the prototype antennas. The optimization goal, TEM_{00} with $w_0 = 0.588\lambda$ ($D = 14\,\mathrm{mm}$), is drawn for comparison. The optimized antenna clearly has a radiation diagram which is almost frequency independent in the frequency range $30 - 60\,\mathrm{GHz}$. Adding the blankets to the setup changes the radiation diagrams drastically. Vertical dotted lines are drawn at $\pm 0.1\,\mathrm{rad}$, $\pm 0.3\,\mathrm{rad}$ and $\pm 0.7\,\mathrm{rad}$.

6.2a-b, the results of the optimization can be clearly seen: the directivity and shape of the optimized antenna diagrams are a lot more homogeneous than for the conical antenna, whose diagram gets narrower and shows a strong increase in directivity when the frequency rises. When the blankets are added to the setup, the directivity of the optimized antenna remains less frequency dependent than that of the conical antenna. However, the shape of the optimized antenna diagrams is no longer frequency independent, but shows strong variations depending on the frequency, with sidelobes at different locations for all frequencies and a double-hump shape appearing at 45 GHz. As the measurements at 45 GHz have lower accuracy in the used measurement setup, it is possible that this effect would look slightly different when the measurements were to be repeated with more appropriate Q-band equipment.

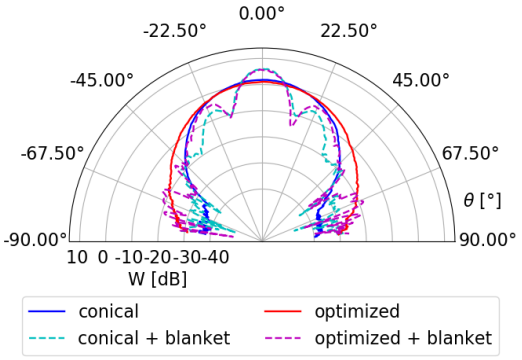

(a) 30 GHz

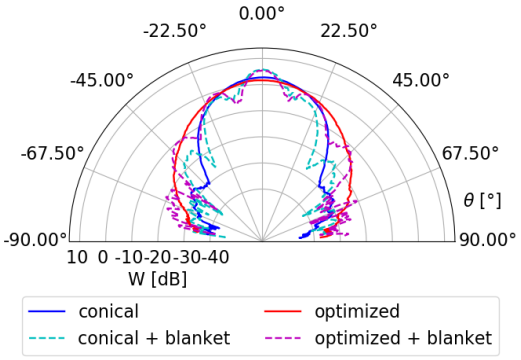

(b) 37.50 GHz

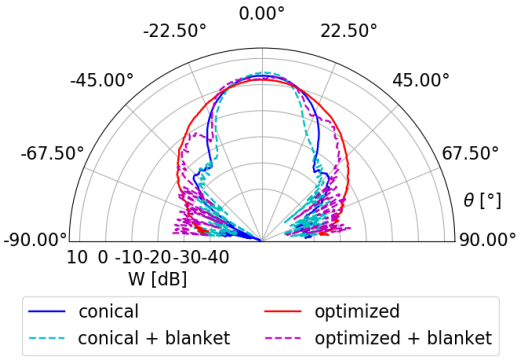

(c) 45 GHz

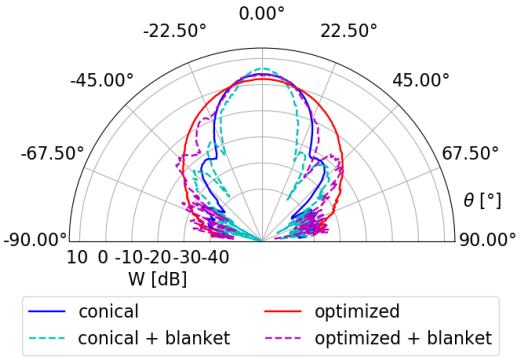

(d) 52.50 GHz

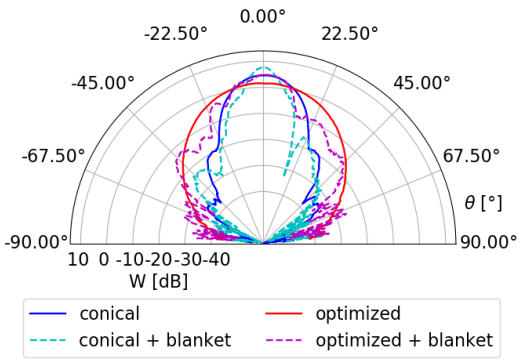

(e) 60 GHz

Figure 6.3: Poloidal (H-plane) radiation diagrams of the optimized and reference conical antenna prototypes with and without blankets at different frequencies. The reference antenna has a higher directivity for all frequencies. The blankets cause sidelobes and a change in directivity and radiation shape for both antennas.

In Figure 6.3, the same information is presented in polar coordinates and a logarithmic scale. The radiation diagram of the conical antenna shows a better directivity than the optimized antenna, both with and without blankets. The difference between the directivity of the antennas varies depending on the frequency. Also here it can be seen that adding the blankets to the setup undoes part of the optimization done by creating frequency dependence and high sidelobes. These effects were partly expected [11], but unfortunately it was not possible to take them into account in the PROFUSION optimization.

The influence of the blankets on the radiation diagram makes it no longer frequency independent, so that it does not, as intended, reduce the complexity of the problem. The change in radiation diagram also means that the performance of the antenna, which was assessed with R2P2, has changed. The sidelobes, which do not show when the antenna is used without blanket environment but are present when mounted in the environment, can cause unwanted direct reflections to the receiver, lowering the performance of the antennas (Section 4.2.5).

In addition to these measurements, different versions of the mock-up blankets with different lengths L (the length of the narrow part between the blankets, see Figure 3.3) were made to evaluate how the length of this section influences the radiation diagram. In addition to the blankets with $L = 120\,\text{mm}$ (which are used in other studies, R2P2 simulations, and Fig. 6.2 and 6.3) blankets with $L = 30,\ 60$ and $90\,\text{mm}$ were used. The results can be seen in Figure 6.4 for 30 and 52.5 GHz, the results for the other frequencies are found in Appendix C. It is seen that for 30 GHz the blankets with $L = 60\,\text{mm}$ result in an antenna diagram which is close to the optimization goal. However, at other frequencies such as 52.5 GHz, this is absolutely not the case. The reason for this is that the near field of the antenna, when placed in the environment, differs a lot depending on the used frequency. Therefore the effects of different blanket lengths also differ depending on the used frequency. Based on these results, there is no preferred value of L. However, already for the currently used $L = 120\,\text{mm}$ the heat loads on the antennas could be problematic [43], so $L < 120\,\text{mm}$ is not advisable from thermal point of view.

Another thing that is noticed in Figure 6.4 is the asymmetry which is present in some of the radiation patterns. This can be assigned to small misalignment of the antenna and blanket structure, which can occur as there are a lot of mechanical changes on the setup during these measurements. This explanation is supported by comparison of Figure 6.4b with Fig. 6.2d, which also shows results for the $L = 120\,\text{mm}$ measurement at 52.5 GHz, but measured in a measurement sequence with few mechanical changes. In Fig. 6.2d the asymmetry is not present. The observed asymmetry indicates that correct alignment of the setup is crucial for the resulting radiation diagram. Not only does this put strict tolerances on the antenna mounting, it also emphasizes the importance of the mode analysis of the antenna input (Section 5.2). High mode purity at the antenna input is required as small angular offsets (which can be caused by higher-order modes) could result in large asymmetry when taking the blankets into account. Addition-

ally, an extended study on the thermal behaviour of the complete system should be made to evaluate the effect of possible thermal expansion (resulting in e.g. a reduction of the blanket interspace or a change in the antenna position) on the radiation patterns.

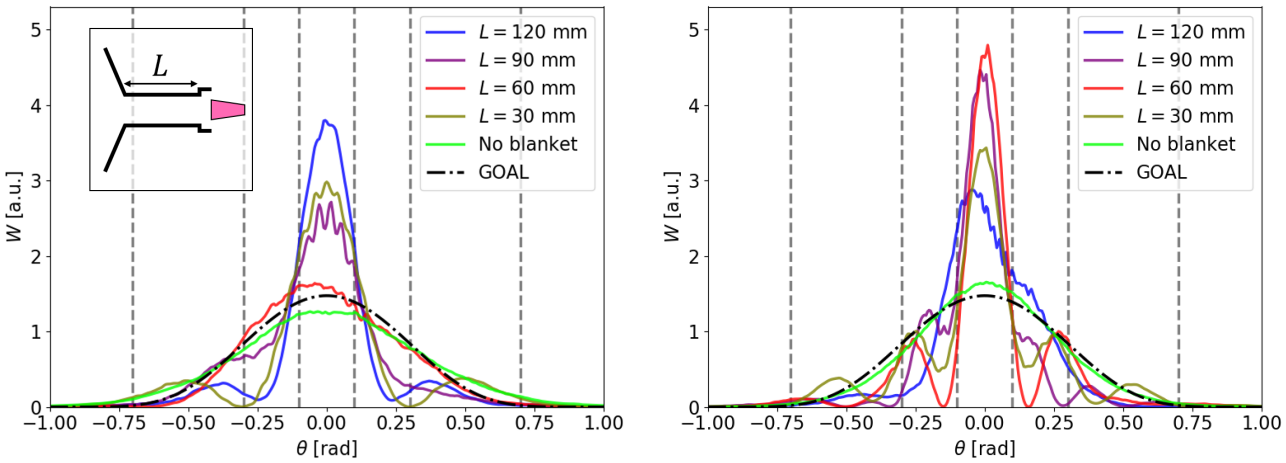

(a) 30 GHz (b) 52.5 GHz

Figure 6.4: Linear-scaled poloidal radiation diagrams of the optimized prototype antenna when using blanket structures with different lengths L. The optimization goal, TEM_{00} with $w_0 = 0.588\lambda$ ($D = 14\,\mathrm{mm}$), is drawn for comparison. Vertical dotted lines are drawn at ± 0.1 rad, ± 0.3 rad and ± 0.7 rad.

It is possible to use other optimization software such as the finite-element solver HFSS to model the antenna with environment and perform a similar optimization directly taking into account the blankets. Another possibility would be to obtain the optimal aperture fields for the antenna from software such as HFSS (taking into account the environment) and then use these results as input fields for the PROFUSION optimizer. Models for the traditional SINC14 PPR antennas have been made in HFSS in [29], where it was noted that: 'One of the major problems we had to deal with concerning HFSS was the large computational requirement for complex simulations at higher frequencies. Great part of the simulation work consisted in finding ways to reduce the computational effort in the models, without loosing accuracy in the results.' It can be expected that these problems will be even larger when making an optimization of the antenna shape with a model that includes blanket structures. Ideally, a study of higher-order modes in the antenna waveguide is done before the final antenna design is made, so that higher-order modes at the antenna input can be taken into account in the optimization. Also, when changing the antenna from a pyramidal to a more complicated optimized shape, the thermal behaviour of the antennas [43] needs to be re-evaluated.

Conclusions

In order to get accurate feedback on the plasma position, plasma positioning reflectometry (PPR) can be used as alternative or extension for magnetic diagnostics for plasma position control in large tokamaks. The blanket structures in these tokamaks are known to cause strong perturbations on the receiver antenna signals, making plasma position reconstruction methods using neural networks or full-wave simulation databases indispensable. Even when using these approaches, simplifications in the PPR system are necessary to make the methods computationally less intensive so that they can provide real-time results. In this work the antennas used for PPR were optimized so that they have similar characteristics independent of the used frequency. This reduces the weight of the calibration calculations necessary to extract plasma parameters from the perturbed signals since the convolution between the spatial correlation of the turbulence and the frequency dependency of the antenna diagram would disappear.

The parallelized, two dimensional ray tracing code R2P2 was built to simulate the behaviour of different antennas in an ITER-like environment, to evaluate the performance of the antennas at different frequencies and turbulence levels. Based on the simulation results, the radiation pattern was divided into regions with different behaviour. Rays launched in the first zone, $|\theta| < 0.1\,\mathrm{rad}$, are the only ones with a chance on an unperturbed trajectory (passing once through the plasma and returning to the receiver without reflections on the blankets). Rays launched up to $|\theta| = 0.3\,\mathrm{rad}$ have a relatively high probability of returning to the receiver, whereas rays in $0.3\,\mathrm{rad} < |\theta| < 0.7\,\mathrm{rad}$ have low chances of contributing to the received signals. Rays with $|\theta| > 0.7\,\mathrm{rad}$ have a high chance of being received after direct reflections on the blankets, and cause strong parasitic effects.

For all simulated radiation diagrams, a maximum antenna coupling was seen at 3 % turbulence while varying turbulence level at a constant frequency. This is caused by the interplay of two turbulence effects. When turbulence rises, the chance on density regions which deflect the rays away from the antenna increases, which results in a lower probability for a ray to be received. However, the turbulent regions might also deflect rays that would normally not be received in the direction of the receiver. This last effect has as a consequence that rays in directions which are never received at low levels of turbulence do get a chance of being received starting from intermediate turbulence levels. The combination of the broadening of the theta-interval which contributes to the receiver signal and the counteracting lowering of the probability leads to the observed maximum antenna coupling around 3 % turbulence.

Both the aperture size and beam waist of the antennas were varied in multiple simulations, showing that an increased aperture size with a linear scaling of the beam waist resulted into fewer invalid runs (simulations from which no valid time of flight could be calculated), higher power returns and a time-of-flight distribution with a mean close to the non-turbulent time of flight. However, strongly focused beams were not always found to have a better performance than broader beams. For example, radiation diagrams with a narrow central beam but sidelobes in $|\theta| > 0.7\,\text{rad}$ have a large chance on invalid runs, because direct reflections from the sidelobes to the antenna cause parasitic signals in the receiver. From the tested radiation patterns, fundamental Gaussian radiation patterns with large beam waists were found to have the best overall performance.

By comparing the time-of-flight distributions of the different antennas, it was found that when changing the radiation pattern, the behaviour of the system can change significantly, suggesting that it is possible to optimize the antennas not only to simplify the whole PPR system, as was done in the next part of this study, but also to minimize specific multi-reflection effects.

Given the ITER spatial constraints, an antenna radiating fundamental Gaussians with beam waist $w_0 = 0.588\lambda$ and $D = 14\,\text{mm}$ was proposed as optimal antenna. It has good PPR performance and a relatively broad, but frequency-independent radiation diagram in the frequency range $30-60\,\text{GHz}$, paving the way for real-time plasma position reconstruction. To find out which antenna shape (if any) had the required characteristics, an antenna shape optimization was made using PROFUSION. After increasing the antenna aperture size from 14 mm to 19.598 mm, a shape for a cylindrical horn antenna was found which agrees for 98.33 % on average with the desired radiation patterns. The increased diameter could pose problems with the antenna mounting, but a smaller antenna would have a broader main lobe with more power radiated in unwanted $|\theta| > 0.7\,\text{rad}$ region.

To validate these results coming from the numerical optimization, a prototype of the optimized antenna was made and tested against a reference conical antenna with the same outer dimensions. The optimized antenna simplified the radiation characteristics a lot, proving it to be a good optimization. Nevertheless, when repeating the experiments with mock-up aluminium blanket structures resembling the ITER antenna environment, the blankets interfered with the radiation pattern, making the advantages of the optimization disappear.

To evaluate the impact of boundary conditions on the effective radiation pattern of the system consisting of antenna and blankets, different geometries were tested. Different lengths of mock-up blankets (corresponding with placing the antenna closer to the plasma) did not show improvements in the radiation diagrams. These measurements involved many mechanical changes to the setup, which resulted in minor misalignment errors. The asymmetry in the radiation patterns as a consequence of these misalignments was found to be very large. This means that extra care should be taken for the mounting of in-vessel antennas in blanket-equipped tokamaks, as well as for the installation of the blanket environment. Since the antennas are known to face large heat loads, a study on

the impact of thermal expansion on the system should be done to evaluate if the resulting geometrical variations modify the system characteristics significantly or not.

An analysis of the effects of higher-order modes at the antenna input was done and showed that 1 % power in the TE_{21} mode can result in angular offsets of the radiation diagram of more than 1.5° when using the optimized antenna without blankets. It is not inconceivable that higher-order modes would be present at the ITER PPR antenna input, considering the many bends and the length of the transmission line leading to the antennas.

To conclude, a second optimization, done with different software that allows the surrounding blankets to be present in the optimization, is suggested. This second optimization should aim to optimize an antenna which yields frequency-independent behaviour when mounted between the blanket structures. Ideally, it would take into account the correct mode mixture at the antenna input. Research on the thermal properties of the antenna when placed in the ITER environment should be done afterwards. Additionally, a study should be made on the exact influence of antenna and blanket alignment on the radiation diagrams and the multi-reflections. Finally, possibilities to increase the space available for the antenna should be considered, since larger antennas could reduce multi-reflection effects and improve the overall PPR performance.

The introduced ray tracing code and the optimization of a PPR horn antenna for blanket-equipped tokamaks are only a first step towards using plasma positioning reflectometry to provide feedback in the plasma position control circuit of large tokamaks. Because of the inaccuracy of the magnetic diagnostics and the quintessential role of plasma position control in a future fusion power plant, it is necessary to further investigate antenna optimizations for this application, if fusion electricity is to become a reality.

Bibliography

[1] E.G. Adelberger et al. Solar fusion cross sections. II. The pp chain and CNO cycles. *Rev. Mod. Phys.*, **83** 195 (2011). doi:10.1103/RevModPhys.83.195.

[2] G. Ericsson. Advanced neutron spectroscopy in fusion research. *J. Fusion Energ.*, **38** 330-355(2019). doi:10.1007/s10894-019-00213-9.

[3] G. Janeschnitz. An economical viable tokamak fusion reactor based on the ITER experience. *Phil. Trans. R. Soc. A.*, **377** 20170433 (2018). doi:10.1098/rsta.2017.0433.

[4] J. Ongena, R. Koch, R. Wolf, and H. Zohm. Magnetic-confinement fusion. *Nat. Phys.*, **12** 398-410 (2016). doi:10.1038/nphys3745.

[5] U. Stroth. *Plasmaphysik*. Vieweg + Teubner Verlag Springer Fachmedien, 2011. ISBN 9783834816153.

[6] D. Reiter. Basic fusion boundary plasma physics: Plasma surface interactions. 10th ITER international school, 2019.

[7] M. Ariola and A. Pironti. *Magnetic Control of Tokamak Plasmas*. Springer Switzerland, 2016. ISBN 9783319298887.

[8] Ph. Moreau, P. Defrasne, E. Joffrin, F. Saint Laurent, and G. Martin. A magnetic diagnostic on Tore Supra. *Rev. Sci. Instrum.*, **74** 4324 (2003). doi:10.1063/1.1606097.

[9] A.E. Costley, T. Sugie, G. Vayakis, and C.I. Walker. Technological challenges of ITER diagnostics. *Fusion Eng. Des.*, **74** 109-119 (2005). doi:10.1016/j.fusengdes.2005.08.026.

[10] Y. Wang, F. Wang, S. Ji, and S. Li. A new analog integrator for magnetic diagnostics on EAST. *IEEE Trans. Nucl. Sci.*, **66**(7) 1335-1339 (2019). doi:10.1109/TNS.2019.2890851.

[11] P. Valera, A. Silva, and J.H. Belo. Testing of the ITER plasma position reflectometry high-field side in-vessel antenna assembly prototype. *Rev. Sci. Instrum.*, **89** 10H102 (2018). doi:10.1063/1.5036743.

[12] C. Laviron, A.J.H. Donné, M.E. Manso, and J. Sanchez. Reflectometry techniques for density profile measurements on fusion plasmas. *Plasma Phys. Control. Fusion*, **38** 905 (1996). doi:10.1088/0741-3335/38/7/002.

[13] A. Silva et al. Microwave reflectometry diagnostic for density profile and fluctuation measurements on ASDEX Upgrade. *Rev. Sci. Instrum.*, **70** 1072 (1998). doi:10.1063/1.1149439.

[14] J. Santos et al. Reflectometry-based plasma position feedback control demonstration at ASDEX Upgrade. *Nucl. Fusion*, **52** 032003 (2012). doi:10.1088/0029-5515/52/3/032003.

[15] F. da Silva, S. Heuraux, E. Ricardo, P. Quental, and J. Ferreira. Assessment of the measurement performance of the in-vessel system of gap 6 of the ITER plasma position reflectometer using a finite-difference time-domain Maxwell full-wave code. *Rev. Sci. Instrum.*, **87** 11E727 (2016). doi:10.1063/1.4962356.

[16] J. Santos, F. Nunes, M. Manso, and I. Nunes. Neural network evaluation of reflectometry density profiles for control purposes. *Rev. Sci. Instrum.*, **70** 521 (1999). doi:10.1063/1.1149379.

[17] R.B. Morales et al. The reconstruction of hollow areas in density profiles from frequency swept reflectometry. In *Proceedings of the 14th Intl. Reflectometry Workshop*, (2019).

[18] S. Heuraux. Personal communication, 2020.

[19] P. Valera, J.H. Belo, and P.B. Quental. Performance assessment of the antenna setup for the ITER plasma position reflectometry in-vessel systems. *Rev. Sci. Instrum.*, **87** 11E713 (2016). doi:10.1063/1.4961291.

[20] B. Plaum. Simulation of microwave beams with profusion (2019 edition). *OPUS - Online Publikationen der Universität Stuttgart*, 2019.

[21] B. Plaum. Optimization of broadband smooth-wall circular horn antennas. *J. Infrared Millim. Te.*, **39**(10) 984-995 (2018). doi:10.1007/s10762-018-0510-6.

[22] B. Plaum. Optimization of oversized waveguide components. Dissertation. https://elib.uni-stuttgart.de/bitstream/11682/1543/1/diss_plaum.pdf, 2001.

[23] P.F. Goldsmith. *Quasioptical Systems*. IEEE Press, 1997. ISBN 0780334396.

[24] C.A. Balanis. *Antenna Theory: Analysis and Design*. Wiley, 2016. ISBN 97811186420601.

[25] W.L. Stutzman and G.A. Thiele. *Antenna Theory and Design*. Wiley, (2012). ISBN 9780470576649.

[26] P. Valera, J.H. Belo, A. Silva, and F. da Silva. Design status of the in-vessel subsystem of the ITER Plasma Position Reflectometry system. *J. Instrum.*, **14** C09002 (2019). doi:10.1088/1748-0221/14/09/C09002.

[27] F. da Silva, S. Heuraux, and M. Manso. Developments on reflectometry simulations for fusion plasmas: application to ITER position reflectometers. *J. Plasma Phys.*, **72**(6) 1205-1208 (2018). doi:10.1017/S0022377806005940.

[28] S. Heuraux. On the difference between phase and amplitude behaviours: dependencies on the radiation pattern and on the turbulence level. In *Proceedings on the 12th Intl. Reflectometry Workshop*, (2015).

[29] H. Hugon. Study and optimisation of the antennas for the ITER plasma-position reflectometry diagnostics system. Unpublished. https://fenix.tecnico.ulisboa.pt/downloadFile/395146459392/Resumo%20Alargado.pdf, (2014).

[30] J. Peddie. *Applications of Ray Tracing*, pages 91–128. Springer International Publishing, (2019). ISBN 978-3-030-17490-3. doi:10.1007/978-3-030-17490-3_6.

[31] Z. Yun and M.F. Iskander. Ray tracing for radio propagation modeling: Principles and applications. *IEEE Access*, **3** 1089-1100 (2019). doi:10.1109/ACCESS.2015.2453991.

[32] B. Chaudhury and S. Chaturvedi. Comparison of wave propagation studies in plasmas using three-dimensional finite-difference time-domain and ray-tracing methods. *Phys. Plasmas*, **13** 123302 (2006). doi:10.1063/1.2397582.

[33] E.R. Tracy, A.J. Brizard, A.S. Richardson, and A.N. Kaufman. *Ray Tracing and Beyond*. Cabridge University Press, 2014. ISBN 9780521768061.

[34] E.Z. Gusakov, A.V. Surkov, and A.Y. Popov. Multiple scattering effect in Doppler reflectometry. *Plasma Phys. Control. Fusion*, **47**(7) 959 (2005). doi:10.1088/0741-3335/47/7/001.

[35] J.H. Belo, P. Valera, and A. Silva. Benchmarking of the EM modelling of the ITER plasma position reflectometry in-vessel antennas with a metallic target using prototype tests. *J. Instrum.*, **15** C01033 (2020). doi:10.1088/1748-0221/15/01/C01033.

[36] F. da Silva, S. Heuraux, E.Z. Gusakov, and A. Popov. A numerical study of forward- and backscattering signatures on doppler-reflectometry signals. *IEEE Plasma Sci.*, **38**(9) 2144-2149 (2010). doi:10.1109/TPS.2010.2056703.

[37] C. Fanack et al. Ordinary-mode reflectometry: modification of the scattering and cut-off responses due to the shape of localized density fluctuations. *Plasma Phys. Control. Fusion*, **38** 1915 (1996). doi:10.1088/0741-3335/38/11/004.

[38] R.V. Leslie. Microwave sensors. In *Comprehensive Remote Sensing*, chapter 1.16, pages 449–450. Elsevier, (2018).

[39] C. Honoré, P. Hennequin, Truc. A., and A. Quéméneur. Quasi-optical gaussian beam tracing to evaluate doppler back-scattering conditions. *Nucl. Fusion*, **46** S809 (2006). doi:10.1088/0029-5515/46/9/S16.

[40] C. Fanack. Etude analytique et numérique de la réflectométrie dans un plasma fluctuant: modèles à une et deux dimensions. Dissertation, 1997.

[41] B. Plaum. Personal communication, 2020.

[42] E.V. Sysoeva, F. da Silva, E.Z. Gusakov, S. Heuraux, and A.Y. Popov. Electron cyclotron resonance heating beam broadening in the edge turbulent plasma of fusion machines. *Nucl. Fusion*, **55**(3) 033016 (2015). doi:10.1088/0029-5515/55/3/033016.

[43] J. Nietiadia, C. Vidala, R. Luisa, and P. Varela. Thermal analyses of the in-vessel frontends of the ITER plasma position reflectometry system. *Fusion Eng. Des.*, **156** 111599 (2020). doi:j.fusengdes.2020.111599.

Appendices

A Received Power Reconstruction

Note: the notation introduced in Chapter 3 for the state of a ray Γ_p^i (Eq. 3.22) is also used in this appendix, with i the ray number and p the state number with $p = 0$ the initial, launching state and $p = q$ the state at final state of the ray.

After the main R2P2 program (Algorithm 1) has run, for each simulation information is available on whether a ray returns to the receiver or not, and if yes, at what time this happens. A ray tracing code does not lend itself to a plasma position reconstruction using Abels inversion (Eq. 2.32), so instead a reconstruction is made for the received power $P(t)$. In a first approximation, the rays can be considered to 'carry' the power. Ray i would then carry power $P^i = \frac{1}{2}P_{\theta_{i-1}\to\theta_i} + \frac{1}{2}P_{\theta_i\to\theta_{i+1}}$ (with $P_{\theta_{i-1}\to\theta_i}$ the power located between θ_{i-1} and θ_i in the radiation diagram[1]). When ray i would be received at time t_q^i, the whole power P^i would arrive at the receiver on that time, or: $P(t) = \sum_{\text{received}\,i} P^i\delta(t_q^i - t)$ (with $\delta(t) = 1$ for $t = 0$ and $\delta(t) = 0$ elsewhere).

The assumption that the power is carried on the rays is however wrong. With this approach the wave nature of the fields is forgotten. The power is not located on the rays but in between them, making it wrong to say that when two neighbouring rays return, it results in two peaks in $P(t)$ at t_q^i and t_q^{i+1} (note that in general $q^i \neq q^{i+1}$). In reality, $P(t) > 0\ \forall t \in [t_q^i,\, t_q^{i+1}]$, as the power between the rays will return during this interval and not only when the rays return. One possibility would be to launch an extremely high number of rays, so that in a limiting case the first approximation becomes correct. This would however increase the calculation time a lot. A second approach uses phase front reconstructions and takes into account rays $i-1$ and $i+1$ for each collected ray i, so that the power can be considered between the rays. By defining multiple phase fronts around the collection times of the rays (as illustrated in Figure A1), a good approximation of $P(t)$ can be made while simulating only few rays. The reconstruction is done step by step in the following paragraphs and is graphically represented in Figure A2. The reconstruction of the phase fronts involves a lot of interpolations, all of these calculations are however very fast, so that there is a considerable speed increase compared to the alternative of launching a lot more rays.

[1] Recall that $\forall i : \theta_{i-1} < \theta_i < \theta_{i+1}$.

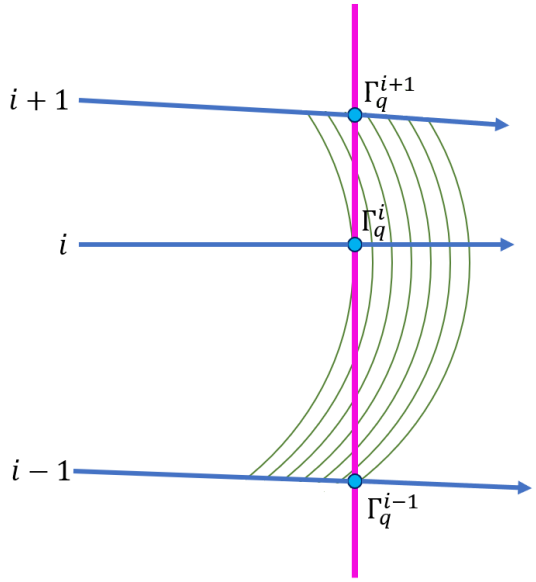

Figure A1: Aperture (violet) with three received rays (blue) and several phase fronts shown (green). The phase fronts are received at various times τ_a between the recollection of the first and the last ray. The aperture area between the intersection points of phase front ϕ_a with the aperture is already received at τ_a.

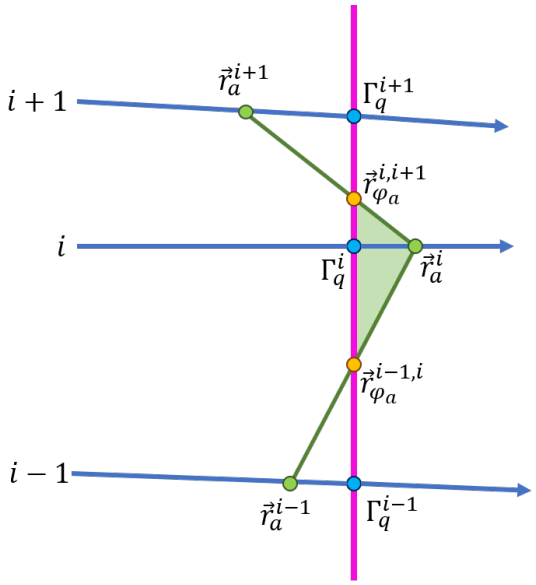

Figure A2: Aperture (violet) with three received rays (blue), showing the reconstruction of phase front ϕ_a (green) and its associated intersection points $\vec{r}_{\phi_a}^{\,i,i+1}$, $\vec{r}_{\phi_a}^{\,i-1,i}$ which are used to find the received power at time τ_a.

Suppose rays $i-1$, i and $i+1$ are all received and the end state of ray i (at step q^i) is

$$\Gamma_q^i = (\vec{r}_q, \vec{k}_q, \phi_q, t_q)^i \tag{6.1}$$

with $\vec{r}_q = (x_q, z_q)^i$. It is possible to reconstruct the phase fronts of the received rays at different times, similar to the phase fronts that are drawn in Figure A1.

Suppose $t_q^i < t_q^{i+1} < t_q^{i-1}$ (other cases are analogous). Between the first collection time (associated with phase ϕ_q^i) and the last collection time (associated with phase ϕ_q^{i+1}), an array of times can be defined:

$$\tau_a = (1-a) \cdot t_q^i + a \cdot t_q^{i-1} \tag{6.2}$$

with $a \in [0,1]$. At each of these times, a different phase front is being received by the antenna. Because the last part of the ray propagation is always in vacuum, the phase accumulation is linear in time (Eq. 3.24). This makes it possible to interpolate the received phases as

$$\phi_a = (1-a) \cdot \phi_q^i + a \cdot \phi_q^{i-1} \tag{6.3}$$

using the same interpolation as for τ_a.

For each of the received rays, the direction of propagation when received is stored in $\vec{k}_q$. Together with the coordinates at collection $\vec{r}_q$ and the phase ϕ_q, an interpolation is made to find the coordinates of the rays when their phase equals ϕ_a. For ray i, this is given by:

$$\vec{r}_a^{\,i} = \vec{r}_q^{\,i} + \frac{\vec{k}_q^i}{|\vec{k}_q^i|} \cdot c\frac{\phi_a - \phi_q^i}{\omega} \tag{6.4}$$

With three points for each phase front ϕ_a ($\vec{r}_a^{\,i-1}$, $\vec{r}_a^{\,i}$ and $\vec{r}_a^{\,i+1}$), the intersection points of the phase fronts with the aperture can be determined. This is done by defining three straight lines (each time through two of the above points) and finding their intersection with the aperture. Only the two intersections which are in the line segment of the aperture defined by the original collection points are kept. The resulting coordinates are named $\vec{r}_{\phi_a}^{\,i,i+1}$ for the intersection of the aperture with the line through ($\vec{r}_a^{\,i}$ and $\vec{r}_a^{\,i+1}$ and analogous for the other line.

Yet another interpolation is made to obtain the angles θ_{ϕ_a} associated with the interpolated aperture points. For point $\vec{r}_{\phi_a}^{\,i,i+1}$, this is a simple linear interpolation of this point between the coordinates $\vec{r}_q^{\,i}$ associated with θ^i and $\vec{r}_q^{\,i+1}$ associated with θ^{i+1}, for the other point it is analogous. In the radiation diagram, is the area between the two found angles θ_{ϕ_a} that is already received at time τ_a (the cumulative power, not $P(\tau_a)$). To find the power received at τ_a, the accumulated power of the previous phase front needs to be subtracted. For convenience θ_a is used to represent the θ interval which is received at time τ_a. With $W(\theta)$ as angular power density, the received power becomes:

$$P(\tau_a) = \int_{\theta_a} W(\theta)\mathrm{d}\theta - \int_{\theta_{a-1}} W(\theta)\mathrm{d}\theta \tag{6.5}$$

Examples of the above reconstruction are given in Figure 4.3(left). One issue rises when not all three rays are received, for example at the very edge of the aperture. What can be done in this case is to temporarily assume that the third ray (which will be located just next to the aperture, as the spatial resolution is very high here) is received and use it to build the phase fronts. Of course, when defining the received θ-interval (Eq. 6.5), it must made sure that only the zone

that actually falls inside the aperture is accounted for. It is important to note that the many interpolations used are not the only possibility for making a phase front reconstruction. For example, parabola or circles might be fitted through the three phase front points instead of piece-wise lines, or the order of interpolations could be slightly changed. Many of these possibilities have not been tried in the development of R2P2 but this could yield slightly different and possibly more accurate results. Benchmarking of the code (e.g. against other ray tracing or full-wave codes) whilst using different phase front reconstruction techniques would be a good way of selecting an optimal technique and quantifying its performance.

Another interesting quantity to compare would be the average time of flight τ_{TOF} of the rays, which gives a low-order indication of the location of the cut-off layer (Eq. 2.28, 2.30). The most basic definition for this is (with a running over all phase fronts of all received rays):

$$\begin{aligned}\tau_{\mathrm{TOF}} &= \frac{\int \mathrm{d}t\ t \cdot P(t)}{\int \mathrm{d}t P(t)} \\ &= \frac{\sum_a \tau_a \cdot P(\tau_a)}{\sum_a P(\tau_a)}\end{aligned} \tag{6.6}$$

The real collection process is an energy transport process, which is dependent on the electromagnetic power flux. To make a more correct estimate of τ_{TOF}, Equation 6.6 needs to be weighted with the power flux. Consider two rays i and $i+1$, between which the complete power is $P^{i,i+1} = \int_{\theta^i}^{\theta_{i+1}} \mathrm{d}\theta W(\theta)$. For these rays, multiple phase fronts ϕ_a have been defined which are received at times τ_a. The average time of recollection for the power between these two rays is:

$$\tau^{i,i+1} = \sum_a \frac{\tau_a \cdot P(\tau_a)}{\sum_a P(\tau_a)} \tag{6.7}$$

This is a normal average, the same as in Equation 6.6. For these rays, a weight is defined based on the power flux (which is defined over the aperture in only a single dimension so [W/m] as units):

$$w^{i,i+1} = \frac{P^{i,i+1}}{|\vec{r}_q^{\,i} - \vec{r}_q^{\,i+1}|} \tag{6.8}$$

The average time of flight is then (summing over only received rays i for which ray $i+1$ is also received):

$$\tau_{\mathrm{TOF}} = \frac{\sum_i \tau^{i,i+1} w^{i,i+1}}{\sum_i w^{i,i+1}} \tag{6.9}$$

B R2P2 Results

Results of the R2P2 simulations that were not given in Chapter 4 are given here. In the tables that follow abbreviations will be used to describe the simulated antennas. The list of given names and the description of the antenna can be found in Table B1, superpositions of TEM_{00} and TEM_{10} always have 180° relative phase shift.

Table B1: Names used in this appendix and the corresponding antenna description.

name	**description**
SINC14	square aperture antenna with $D = 14\,\mathrm{mm}$
G14F	fundamental Gaussian with $w_0 = 5.88\,\mathrm{mm}$ and $D = 14\,\mathrm{mm}$
G14L	fundamental Gaussian with $w_0 = 0.588\lambda$ and $D = 14\,\mathrm{mm}$
G28F	fundamental Gaussian with $w_0 = 12\,\mathrm{mm}$ and $D = 28\,\mathrm{mm}$
G28L	fundamental Gaussian with $w_0 = 1.2\lambda$ and $D = 28\,\mathrm{mm}$
G24L	fundamental Gaussian with $w_0 = \lambda$ and $D = 24\,\mathrm{mm}$
S9010	superposition of 90% TEM_{00} and 10% TEM_{10} with $w_0 = 0.588\lambda$ and $D = 14\,\mathrm{mm}$
S8020	superposition of 80% TEM_{00} and 20% TEM_{10} with $w_0 = 0.588\lambda$ and $D = 14\,\mathrm{mm}$
S7030	superposition of 70% TEM_{00} and 30% TEM_{10} with $w_0 = 0.588\lambda$ and $D = 14\,\mathrm{mm}$
S6040	superposition of 60% TEM_{00} and 40% TEM_{10} with $w_0 = 0.588\lambda$ and $D = 14\,\mathrm{mm}$
S5050	superposition of 50% TEM_{00} and 50% TEM_{10} with $w_0 = 0.588\lambda$ and $D = 14\,\mathrm{mm}$

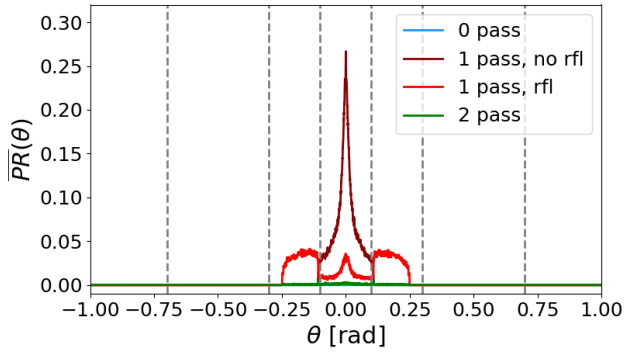

(a) G14F

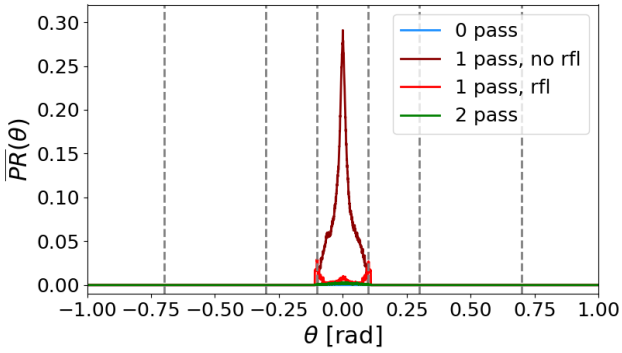

(b) G28F

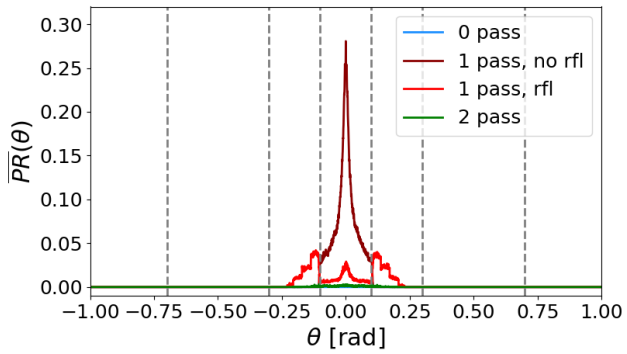

(c) G24L

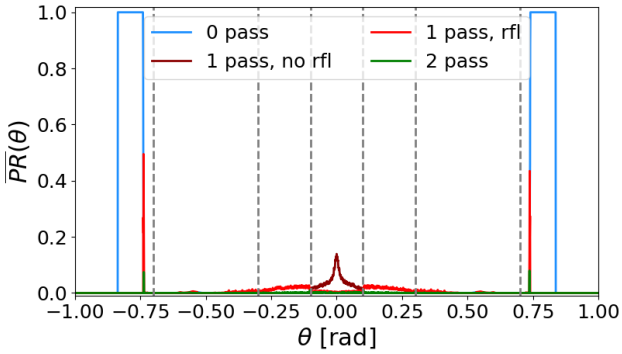

(d) S5050

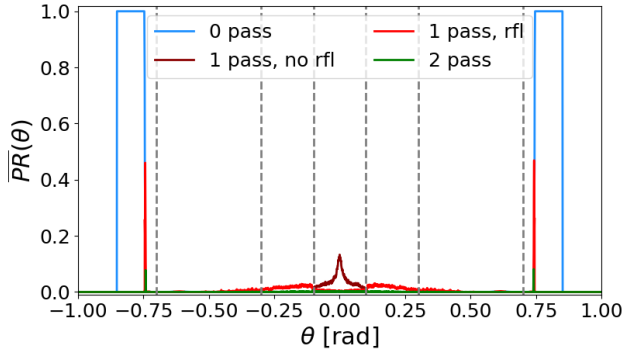

(e) S7030

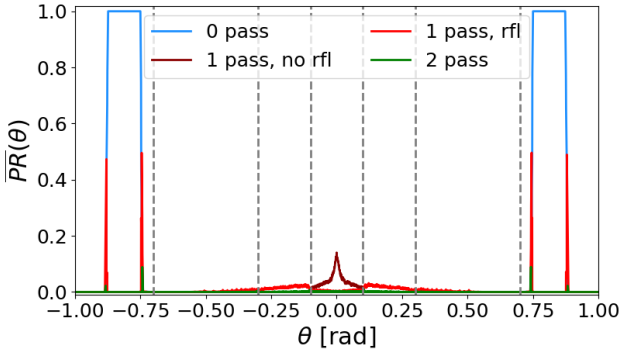

(f) S8020

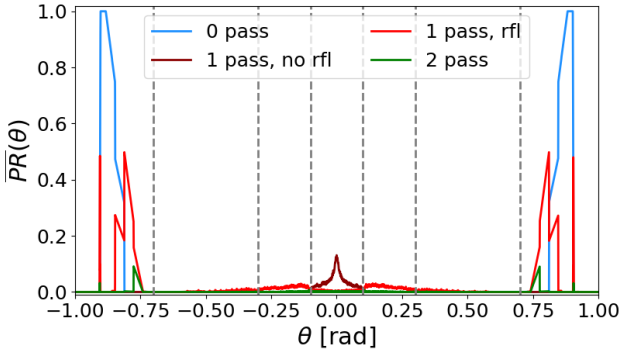

(g) S9010

Figure B1: Probability on return for different antennas averaged over different frequencies and turbulence levels.

Table B2: Mean value of normalized time-of-flight (τ) probability density functions.

f	30 GHz					37.50 GHz					45 GHz					52.50 GHz					60 GHz				
turb. (%)	0.25	1.00	3.00	5.00	10.00	0.25	1.00	3.00	5.00	10.00	0.25	1.00	3.00	5.00	10.00	0.25	1.00	3.00	5.00	10.00	0.25	1.00	3.00	5.00	10.00
SINC14	1.000	1.003	1.005	1.025	1.045	1.000	1.001	0.999	1.015	1.040	1.000	1.000	1.003	1.009	1.030	1.000	0.999	1.002	1.024	1.043	1.000	0.998	1.006	1.026	1.032
G14F	1.001	1.003	1.011	1.037	1.057	1.001	1.003	1.015	1.026	1.043	1.001	1.001	1.017	1.031	1.038	1.000	1.001	1.024	1.025	1.045	1.000	1.001	1.023	1.033	1.040
G14L	1.002	1.004	1.014	1.039	1.040	1.002	1.002	1.020	1.044	1.054	1.001	1.003	1.029	1.048	1.050	1.001	1.001	1.029	1.046	1.062	1.001	0.999	1.033	1.053	1.057
G28F	1.000	1.001	0.995	1.013	1.033	1.001	1.002	0.989	0.994	1.022	1.000	1.001	0.990	1.000	1.013	1.000	0.999	0.996	1.006	1.019	1.000	0.999	1.004	1.017	1.013
G28L	1.000	1.000	0.994	1.022	1.050	1.000	1.001	1.001	1.012	1.025	1.000	1.001	1.006	1.021	1.039	1.000	1.002	1.015	1.029	1.028	1.001	1.001	1.026	1.042	1.037
G24L	1.001	1.001	0.995	1.015	1.044	1.001	1.002	1.007	1.020	1.027	1.001	1.002	1.014	1.029	1.024	1.000	1.002	1.023	1.030	1.038	1.000	1.001	1.026	1.040	1.050
S9010	1.000	1.003	1.022	1.063	1.056	1.000	1.001	1.022	1.034	1.054	1.000	1.001	1.022	1.046	1.061	1.000	1.000	1.030	1.047	1.054	1.000	1.001	1.031	1.050	1.062
S8020	0.999	1.004	1.022	1.049	1.042	1.000	1.002	1.020	1.042	1.055	1.000	1.001	1.025	1.038	1.058	1.000	1.001	1.019	1.050	1.056	1.000	0.999	1.027	1.050	1.051
S7030	1.000	1.005	1.025	1.047	1.057	1.000	1.005	1.025	1.040	1.039	1.000	1.001	1.022	1.042	1.053	1.000	1.001	1.028	1.048	1.056	1.000	1.001	1.029	1.057	1.053
S6040	1.000	1.004	1.019	1.044	1.048	1.000	1.002	1.020	1.040	1.061	1.000	1.000	1.021	1.037	1.040	1.000	1.001	1.027	1.053	1.049	1.000	1.001	1.026	1.043	1.054
S5050	1.000	1.004	1.024	1.035	1.058	1.000	1.002	1.020	1.039	1.054	1.000	1.002	1.017	1.041	1.057	1.000	1.001	1.016	1.042	1.052	1.000	1.000	1.025	1.042	1.062

Table B3: Variances of normalized time-of-flight (τ) probability density functions. The color-coding of the cells represents the skewness s of the distribution: cells are coloured purple when $s < -0.5$, blue when $-0.5 < s < 0.5$, yellow when $0.5 < s < 1.0$, orange when $1.0 < s < 2.0$ and red when $s > 2.0$.

f	30 GHz					37.50 GHz					45 GHz					52.50 GHz					60 GHz				
turb. (%)	0.25	1.00	3.00	5.00	10.00	0.25	1.00	3.00	5.00	10.00	0.25	1.00	3.00	5.00	10.00	0.25	1.00	3.00	5.00	10.00	0.25	1.00	3.00	5.00	10.00
SINC14	2.0E-5	1.3E-3	5.1E-3	1.1E-2	2.0E-2	2.1E-5	2.3E-4	2.6E-3	8.5E-3	1.4E-2	1.8E-5	2.4E-4	3.1E-3	5.9E-3	1.4E-2	1.6E-5	1.9E-4	2.6E-3	7.7E-3	1.3E-2	1.9E-5	3.2E-4	3.0E-3	6.5E-3	1.1E-2
G14F	1.2E-5	1.7E-4	2.3E-3	8.4E-3	1.2E-2	1.4E-5	2.0E-4	2.9E-3	5.5E-3	1.1E-2	1.2E-5	2.3E-4	2.7E-3	5.2E-3	1.0E-2	1.5E-5	2.3E-4	2.6E-3	5.2E-3	1.1E-2	1.4E-5	2.6E-4	3.0E-3	5.6E-3	9.9E-3
G14L	1.4E-5	2.2E-4	3.7E-3	1.2E-2	1.2E-2	1.5E-5	2.1E-4	2.4E-3	7.2E-3	1.4E-2	1.3E-5	2.8E-4	3.1E-3	7.0E-3	1.1E-2	1.3E-5	2.3E-4	2.7E-3	5.3E-3	1.1E-2	1.3E-5	3.4E-4	3.4E-3	6.3E-3	1.1E-2
G28F	1.3E-6	1.7E-4	2.6E-3	1.3E-2	1.6E-2	1.3E-5	2.2E-4	1.6E-3	5.1E-3	1.6E-2	1.5E-5	2.0E-4	1.6E-3	5.1E-3	1.3E-2	1.6E-5	1.7E-4	2.2E-3	6.1E-3	1.3E-2	1.7E-5	1.9E-4	2.6E-3	6.6E-3	1.0E-2
G28L	1.2E-5	1.8E-4	2.6E-3	1.2E-2	2.2E-2	1.6E-5	2.2E-4	2.3E-3	7.8E-3	1.5E-2	1.6E-5	2.1E-4	2.3E-3	6.5E-3	1.6E-2	1.5E-5	2.5E-4	2.2E-3	5.3E-3	1.0E-2	1.5E-5	2.8E-4	3.4E-3	5.3E-3	1.1E-2
G24L	1.4E-5	1.6E-4	2.5E-3	1.1E-2	1.8E-2	1.4E-5	2.1E-4	2.6E-3	7.2E-3	1.3E-2	1.5E-5	2.2E-4	2.4E-3	5.7E-3	1.1E-2	1.5E-5	2.6E-4	2.5E-3	6.1E-3	1.2E-2	1.6E-5	2.6E-4	2.7E-3	5.0E-3	1.1E-2
S9010	1.9E-5	7.2E-4	6.5E-3	1.6E-2	1.4E-2	2.0E-5	2.8E-4	3.4E-3	7.8E-3	1.5E-2	1.7E-5	3.3E-4	3.1E-3	8.1E-3	1.3E-2	1.4E-5	3.2E-4	4.5E-3	7.3E-3	1.3E-2	1.9E-5	3.6E-4	4.2E-3	6.9E-3	1.1E-2
S8020	1.8E-5	5.2E-4	5.7E-3	1.4E-2	1.5E-2	1.9E-5	2.8E-4	3.5E-3	8.7E-3	1.5E-2	1.6E-5	2.6E-4	5.1E-3	6.0E-3	1.4E-2	1.7E-5	3.1E-4	3.5E-3	8.0E-3	1.1E-2	1.6E-5	2.6E-4	4.1E-3	7.3E-3	1.0E-2
S7030	2.0E-5	3.8E-4	6.6E-3	1.2E-2	1.6E-2	1.7E-5	9.3E-4	3.8E-3	8.3E-3	1.3E-2	2.0E-5	5.6E-4	3.4E-3	7.3E-3	1.2E-2	1.9E-5	3.0E-4	3.8E-3	6.5E-3	1.2E-2	1.7E-5	3.0E-4	4.2E-3	7.8E-3	1.2E-2
S6040	2.0E-5	1.3E-3	4.7E-3	1.3E-2	1.5E-2	1.7E-5	2.6E-4	4.3E-3	7.4E-3	1.6E-2	1.6E-5	2.6E-4	3.4E-3	8.5E-3	9.6E-3	1.7E-5	3.0E-4	4.2E-3	8.7E-3	1.2E-2	1.8E-5	3.6E-4	4.3E-3	6.2E-3	1.1E-2
S5050	1.9E-6	4.1E-4	7.6E-3	9.4E-3	1.6E-2	1.8E-5	2.9E-4	4.3E-3	8.7E-3	1.4E-2	1.8E-5	2.8E-4	3.7E-3	9.4E-3	1.4E-2	1.7E-5	3.4E-4	3.1E-3	6.3E-3	1.6E-2	1.7E-5	3.8E-4	3.4E-3	6.1E-3	9.0E-3

Table B4: Kullback-Leibler divergence for time-of-flight probability density distributions: the found distribution for SINC14 serves as $P(\tau)$ and the listed distribution as $Q(\tau)$ with $\mathrm{KL} = \int \mathrm{d}\tau P(\tau)\log(P(\tau)/Q(\tau))$. Color-coding represents the results of the Kolmogorov-Smirnov test done with 99% confidence interval and the SINC14 as reference distribution. Red cells indicate that the distribution is significantly different from the SINC14 distribution at same frequency and turbulence level.

f	30 GHz					37.50 GHz					45 GHz					52.50 GHz					60 GHz				
turb. (%)	0.25	1.00	3.00	5.00	10.00	0.25	1.00	3.00	5.00	10.00	0.25	1.00	3.00	5.00	10.00	0.25	1.00	3.00	5.00	10.00	0.25	1.00	3.00	5.00	10.00
G14F	0.326	0.487	0.794	0.824	0.908	0.245	0.456	0.690	0.764	0.825	0.262	0.414	0.740	0.835	0.871	0.186	0.398	0.850	0.816	0.873	0.222	0.428	0.785	0.833	1.063
G14L	0.216	0.540	0.741	0.808	0.798	0.317	0.484	0.841	0.897	0.822	0.271	0.398	0.895	0.969	0.790	0.175	0.471	0.911	0.792	0.958	0.355	0.455	0.941	0.809	0.910
G28F	0.375	0.695	0.647	0.900	0.766	0.304	0.519	0.718	0.816	0.928	0.251	0.473	0.816	0.769	0.739	0.267	0.423	0.700	0.837	0.821	0.269	0.410	0.722	0.713	1.041
G28L	0.286	0.480	0.719	0.749	0.884	0.215	0.468	0.645	0.760	0.900	0.246	0.490	0.770	0.841	0.777	0.190	0.376	0.705	0.889	0.834	0.243	0.420	0.766	0.711	0.977
G24L	0.288	0.576	0.664	0.800	0.780	0.322	0.443	0.725	0.761	0.818	0.243	0.498	0.702	0.841	0.770	0.198	0.452	0.728	0.755	0.925	0.203	0.479	0.831	0.850	0.953
S9010	0.218	0.537	0.753	0.940	0.821	0.157	0.442	0.827	0.764	0.828	0.240	0.425	0.691	0.911	0.766	0.191	0.497	0.813	0.819	0.836	0.200	0.503	0.851	0.819	0.999
S8020	0.268	0.451	0.675	0.888	0.822	0.137	0.494	0.663	0.834	0.776	0.195	0.446	0.724	0.932	0.840	0.202	0.440	0.767	0.860	0.917	0.244	0.376	0.789	0.795	0.968
S7030	0.163	0.503	0.683	0.751	0.834	0.177	0.502	0.754	0.811	0.835	0.190	0.426	0.817	0.900	0.810	0.193	0.496	0.781	0.828	0.979	0.244	0.460	0.752	0.770	0.978
S6040	0.217	0.529	0.661	0.830	0.876	0.201	0.417	0.763	0.787	0.833	0.203	0.497	0.787	0.806	0.884	0.159	0.488	0.723	0.848	0.952	0.241	0.539	0.719	0.710	1.038
S5050	0.143	0.480	0.699	0.849	0.863	0.235	0.498	0.750	0.757	0.858	0.158	0.525	0.853	0.835	0.825	0.182	0.469	0.722	0.753	0.887	0.216	0.461	0.836	0.698	0.864

Table B5: KL divergence and color-coded KS test results, similar to Tab. B4, now with G14L as reference distribution.

f	30 GHz					37.50 GHz					45 GHz					52.50 GHz					60 GHz				
turb. (%)	0.25	1.00	3.00	5.00	10.00	0.25	1.00	3.00	5.00	10.00	0.25	1.00	3.00	5.00	10.00	0.25	1.00	3.00	5.00	10.00	0.25	1.00	3.00	5.00	10.00
G14F	0.251	0.521	0.692	0.826	0.826	0.325	0.447	0.812	0.914	0.826	0.280	0.449	0.914	0.997	0.835	0.179	0.432	0.926	0.882	0.938	0.249	0.538	0.928	0.801	0.898
G14L	0.202	0.427	0.856	0.799	0.835	0.250	0.494	0.714	0.851	0.869	0.184	0.519	0.758	0.876	0.799	0.188	0.448	0.741	0.750	0.836	0.219	0.506	0.763	0.912	0.962
G28F	0.342	0.658	0.757	0.852	0.799	0.307	0.489	1.013	1.124	0.893	0.295	0.550	1.088	0.995	0.910	0.179	0.468	1.083	0.925	0.955	0.253	0.450	0.990	0.912	0.992
G28L	0.212	0.488	0.884	0.755	0.877	0.300	0.568	0.824	0.905	0.939	0.247	0.481	0.784	0.923	0.779	0.193	0.447	0.756	0.841	0.899	0.146	0.512	0.717	0.767	0.905
G24L	0.181	0.539	0.848	0.787	0.798	0.206	0.430	0.781	0.864	0.862	0.155	0.553	0.740	0.875	0.867	0.195	0.435	0.789	0.833	0.850	0.177	0.588	0.793	0.856	0.887
S9010	0.246	0.510	0.771	0.798	0.802	0.305	0.544	0.769	0.870	0.790	0.245	0.461	0.695	0.814	0.793	0.229	0.491	0.806	0.797	0.813	0.236	0.561	0.686	0.808	0.909
S8020	0.349	0.483	0.743	0.791	0.798	0.266	0.511	0.668	0.834	0.820	0.287	0.554	0.738	0.808	0.815	0.234	0.538	0.842	0.859	0.893	0.258	0.371	0.823	0.793	0.840
S7030	0.224	0.564	0.679	0.776	0.827	0.310	0.475	0.733	0.755	0.863	0.236	0.393	0.698	0.918	0.845	0.238	0.509	0.725	0.853	0.843	0.215	0.575	0.794	0.794	0.887
S6040	0.260	0.446	0.794	0.782	0.884	0.306	0.462	0.859	0.807	0.863	0.247	0.469	0.755	0.890	0.831	0.205	0.539	0.776	0.787	0.858	0.264	0.631	0.752	0.829	0.865
S5050	0.253	0.478	0.795	0.775	0.784	0.291	0.483	0.750	0.793	0.893	0.205	0.584	0.751	0.752	0.823	0.190	0.547	0.787	0.779	0.864	0.300	0.515	0.853	0.792	0.839

Table B6: Fraction of invalid runs for each of the parameter sets. The color code goes from green to red as the fraction becomes larger.

f	30 GHz					37.50 GHz					45 GHz					52.50 GHz					60 GHz				
turb. (%)	0.25	1.00	3.00	5.00	10.00	0.25	1.00	3.00	5.00	10.00	0.25	1.00	3.00	5.00	10.00	0.25	1.00	3.00	5.00	10.00	0.25	1.00	3.00	5.00	10.00
SINC14	0.00	0.01	0.01	0.00	0.04	0.00	0.03	0.01	0.04	0.08	0.00	0.02	0.03	0.06	0.17	0.01	0.03	0.04	0.12	0.28	0.04	0.05	0.10	0.23	0.39
G14F	0.00	0.00	0.00	0.00	0.02	0.00	0.01	0.01	0.02	0.05	0.00	0.01	0.00	0.02	0.06	0.01	0.02	0.02	0.04	0.13	0.04	0.05	0.03	0.09	0.22
G14L	0.00	0.00	0.00	0.00	0.01	0.00	0.01	0.00	0.02	0.02	0.01	0.06	0.01	0.01	0.05	0.08	0.10	0.04	0.07	0.15	0.27	0.21	0.08	0.14	0.28
G28F	0.00	0.00	0.00	0.02	0.02	0.00	0.00	0.01	0.02	0.07	0.00	0.00	0.00	0.04	0.12	0.00	0.00	0.01	0.06	0.21	0.00	0.01	0.03	0.12	0.30
G28L	0.00	0.00	0.00	0.01	0.05	0.00	0.00	0.01	0.02	0.05	0.00	0.01	0.01	0.02	0.08	0.00	0.02	0.02	0.06	0.11	0.05	0.04	0.04	0.08	0.22
G24L	0.00	0.00	0.00	0.01	0.03	0.00	0.00	0.00	0.01	0.05	0.00	0.01	0.01	0.02	0.07	0.00	0.02	0.02	0.03	0.13	0.05	0.06	0.04	0.09	0.19
S9010	0.00	0.04	0.01	0.02	0.05	0.00	0.06	0.01	0.03	0.06	0.04	0.09	0.02	0.05	0.09	0.08	0.12	0.05	0.11	0.23	0.16	0.22	0.10	0.21	0.36
S8020	0.00	0.01	0.01	0.01	0.07	0.01	0.03	0.01	0.02	0.05	0.04	0.06	0.02	0.06	0.10	0.08	0.12	0.03	0.12	0.21	0.17	0.18	0.09	0.22	0.40
S7030	0.01	0.02	0.01	0.01	0.06	0.02	0.05	0.02	0.03	0.06	0.04	0.08	0.03	0.05	0.10	0.10	0.10	0.06	0.11	0.20	0.13	0.21	0.09	0.18	0.38
S6040	0.01	0.04	0.01	0.01	0.07	0.03	0.03	0.01	0.02	0.06	0.05	0.09	0.02	0.05	0.12	0.06	0.13	0.05	0.14	0.23	0.12	0.25	0.12	0.22	0.38
S5050	0.01	0.03	0.03	0.01	0.04	0.01	0.05	0.01	0.05	0.04	0.04	0.11	0.01	0.07	0.13	0.07	0.13	0.06	0.12	0.27	0.13	0.24	0.12	0.15	0.34

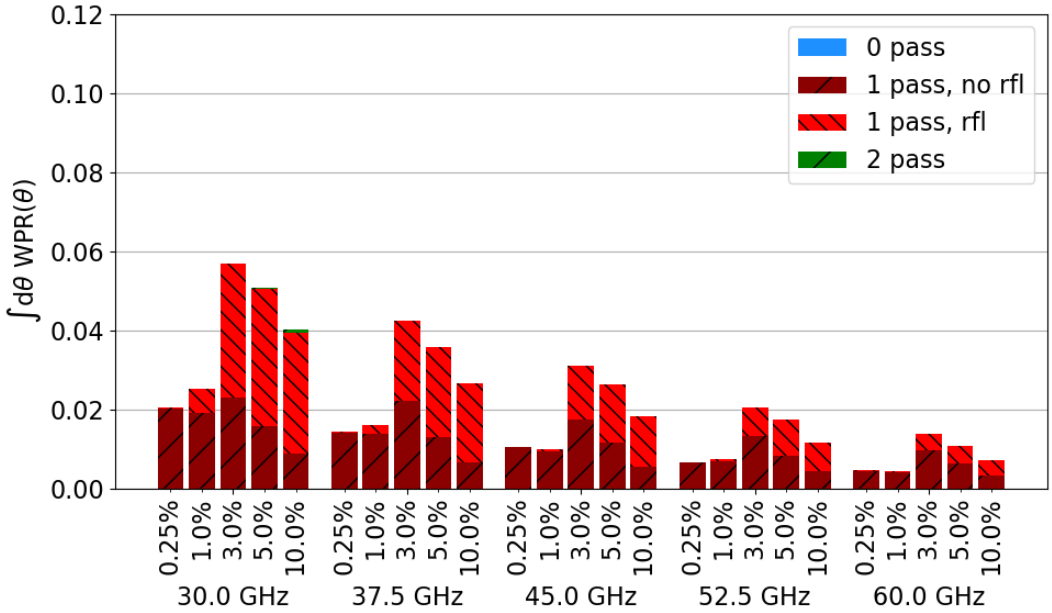

(a) S9010

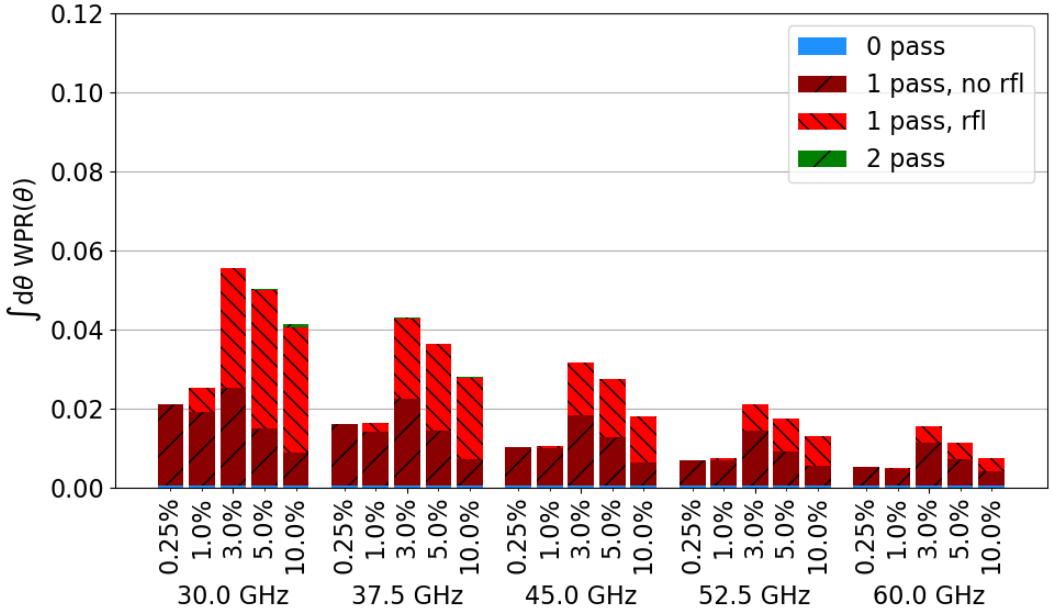

(b) S8020

Figure B2: $\int \mathrm{d}\theta$ WPR(θ) for various simulated antennas at different frequencies and turbulence levels. Colors indicate the type of trajectory the returned ray has taken.

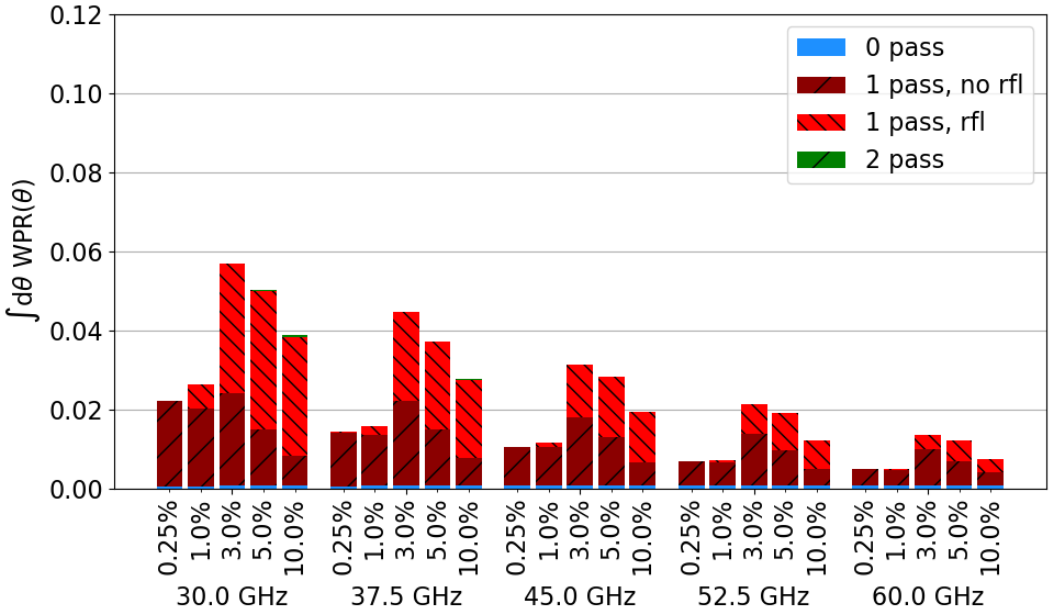

(a) S7030

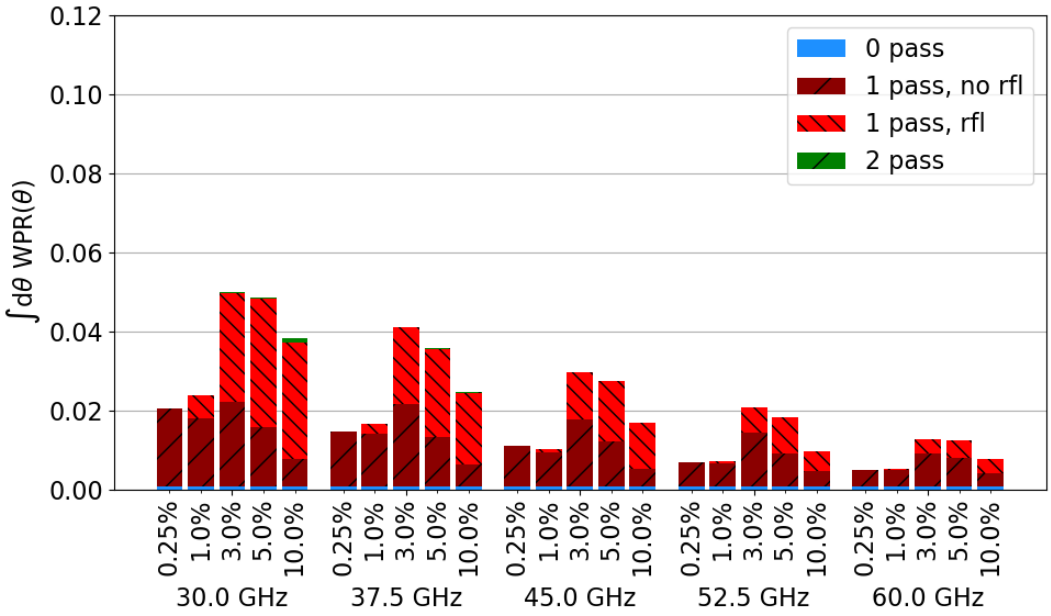

(b) S5050

Figure B3: $\int d\theta$ WPR(θ) for various simulated antennas at different frequencies and turbulence levels. Colors indicate the type of trajectory the returned ray has taken.

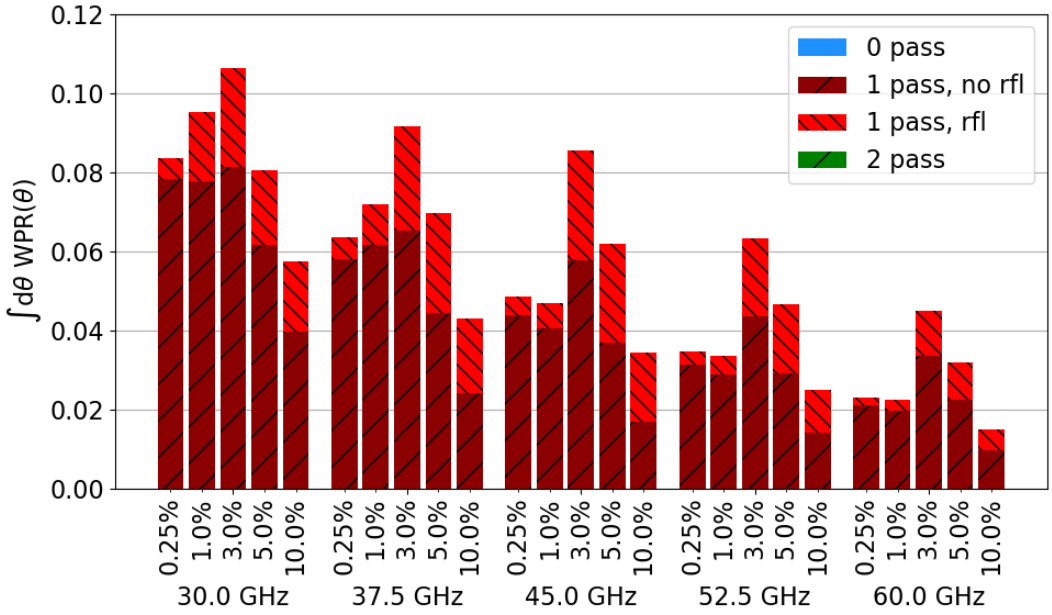

Figure B4: $\int \mathrm{d}\theta$ WPR(θ) for G24L antenna at different frequencies and turbulence levels. Colors indicate the type of trajectory the returned ray has taken.

C Prototype Measurement Results

Results of the measurements with different mock-up blankets that are not given in Figure 6.4 are given in Figure C1.

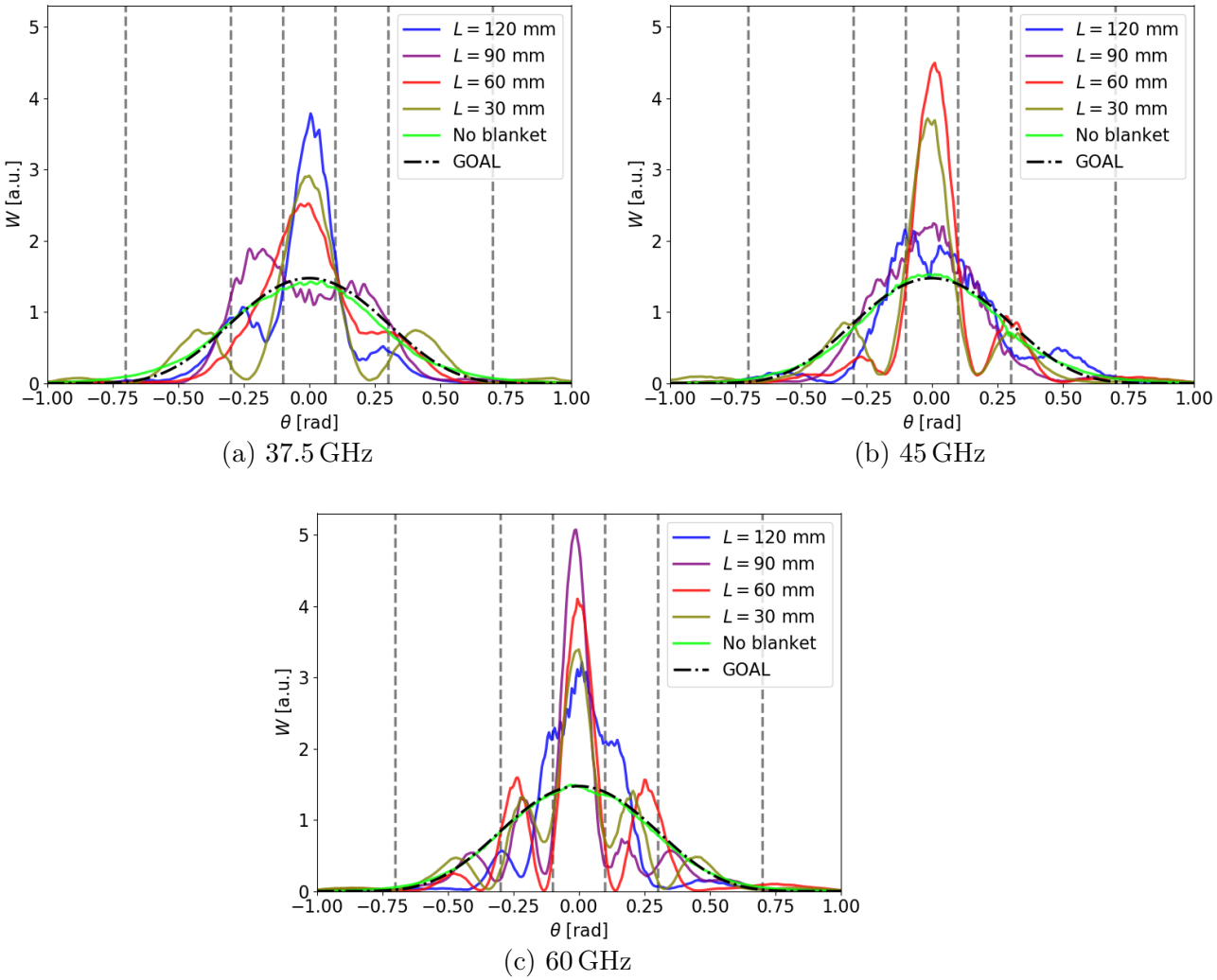

(a) 37.5 GHz

(b) 45 GHz

(c) 60 GHz

Figure C1: Linear-scaled poloidal radiation diagrams of the optimized prototype antenna when using blanket structures with different lengths L. The optimization goal, TEM_{00} with $w_0 = 0.588\lambda$ ($D = 14\,\mathrm{mm}$), is drawn for comparison. Vertical grey lines are drawn at $|\theta| = 0.1\,\mathrm{rad}$, $0.3\,\mathrm{rad}$ and $0.7\,\mathrm{rad}$.

Acknowledgements

I would like to express my profound appreciation for my three supervisors, Stéphane Heuraux, Carsten Lechte and Burkhard Plaum, who, with their complementary expertise, assisted me during this thesis. They have given me lots of help and advise, as well as new insights in physics and engineering, not by presenting solutions on a silver plate, but by sparking my own thought processes and guiding me where necessary. They have shown and taught me, not only during the last months, but over the last two years, the skills and values of a good scientist.

I would like to thank Walter Kasparek and Achim Zeitler, who were of great help during the experimental part of this study, as well as professor Ning Yan Zhu and Riccardo Ragona, with who I discussed various parts of this study.

Last words of thanks go out to my friends and family. There is no measure of how much I value their support, friendship and love. Or maybe there is: *to the sun and back*.

Declaration in lieu of oath

Herewith I declare in lieu of oath that I have prepared this thesis exclusively with the help of my scientific teachers and the means quoted by them.

City, the

Johannes Lips

Copyright Agreement

I hereby grant the FUSION-EP consortium the non-exclusive right to publish this work.

I declare that this work is free of copyright claims of third parties.

City, the

Johannes Lips